UNIVERSITÀ DEGLI STUDI DI PADOVA

DIPARTIMENTO DI BIOLOGIA

Corso di Laurea in Biologia Molecolare

ELABORATO DI LAUREA

I metaboliti microbici derivati dal triptofano attivano il recettore degli idrocarburi arilici (AhR) nei macrofagi associati al tumore per sopprimere l'immunità antitumorale

Tutor: Dott.ssa Gaia Codolo

Dipartimento di Biologia

Laureando: Tommaso Ballocci

ANNO ACCADEMICO 2021/2022

INDICE

ABSTRACT

Il recettore degli idrocarburi arilici (AhR) è un recettore citoplasmatico attivato da ligando che svolge attività a livello nucleare come fattore di trascrizione. AhR svolge un'importante funzione nella modulazione dell'immunità: nell'adenocarcinoma pancreatico la sua espressione nei macrofagi tumore-associati (TAM) è correlata ad immunosoppressione, maggiore crescita tumorale e peggiore prognosi. L'attività immunosoppressiva di AhR viene stimolata dal legame con gli indoli, cataboliti del metabolismo microbico del triptofano a livello intestinale. L'obiettivo dell'articolo oggetto del seguente elaborato è quello di elucidare la funzione di AhR espresso dai TAM nell'adenocarcinoma pancreatico e la sua dipendenza dal microbiota intestinale. Tramite l'utilizzo di modelli murini in cui l'attività di AhR è stata inibita, per delezione o farmacologicamente, è stata riscontrata una minore crescita tumorale ed uno switch pro-infiammatorio dell'infiltrato, con aumento di linfociti T citotossici e polarizzazione infiammatoria dei TAM. Gli stessi risultati sono stati ottenuti in seguito all'eliminazione del triptofano dalla dieta o rimozione di classi batteriche indolo-producenti dal microbiota intestinale. L'articolo evidenzia quindi la relazione tra microbiota intestinale, profilo immunologico del microambiente tumorale e crescita neoplastica, attraverso l'espressione di AhR nei TAM. I risultati dimostrano come agire a livello del microbiota e del suo metabolismo possa essere una valida opzione terapeutica nel caso di tumore al pancreas.

1. STATO DELL'ARTE

1.1. Adenocarcinoma pancreatico

Il pancreas è un organo ghiandolare che presenta una componente endocrina ed una esocrina, adibite a svolgere funzioni fondamentali per il metabolismo e l'omeostasi. Il pancreas endocrino è composto dalle isole di Langerhans, aggregati cellulari al cui interno sono presenti diversi tipi di cellule che si occupano della secrezione di ormoni quali insulina e glucagone, che mediano l'omeostasi del glucosio nel sangue. Il pancreas esocrino, che compone la maggior parte della ghiandola, si occupa della sintesi di enzimi pancreatici che permettono la digestione del cibo e favoriscono l'assorbimento nutritivo a livello intestinale.

Esistono numerose neoplasie correlate al pancreas, che principalmente si suddividono in base al tipo di cellule che colpiscono. Focalizzandosi sul tumore al pancreas esocrino, la forma più comune e più aggressiva di tumore è l'**adenocarcinoma duttale pancreatico** (PDAC), che si sviluppa in seguito a trasformazione in senso neoplastico di una cellula epiteliale del dotto pancreatico: questo tumore porta alla formazione di ghiandole secernenti mucina e attiva un'intensa *desmoplasia stromale*, con conseguente aumento del tessuto connettivo denso circondante il tumore. Le mutazioni genetiche più ricorrenti associate all'insorgenza di questo tumore riguardano diversi geni. Tra questi, l'oncogene *KRAS* (nel 90% dei casi), che sintetizza una GTPasi che media la trasduzione di segnale indotta dai fattori di crescita, *CDKN2A*, regolatore del ciclo cellulare, *TP53*, implicata nella risposta cellulare allo stress, e *SMAD4*, che media la trasduzione di segnale di TGFβ.

L'adenocarcinoma duttale pancreatico è la terza causa di morte da cancro negli Stati Uniti ed è caratterizzato da un tasso di morte estremamente elevato molto paragonabile al tasso di incidenza, e da un tasso di sopravvivenza a cinque anni dalla diagnosi intorno al 6%. Le cause principali che portano a questi risultati risiedono nella tarda diagnosi, nell'inefficienza dei metodi terapeutici e nell'elevato tasso di recidiva. La tarda diagnosi deriva da una comune asintomaticità o sintomatologia non specifica che caratterizza le prime fasi d'insorgenza del tumore, riducendo anche la possibilità di risultare idonei alla chirurgia di resezione. Questa ad oggi è l'unica terapia che può portare ad una sopravvivenza a lungo termine, se comparata all'efficienza della chemioterapia, radioterapia e immunoterapia: tuttavia, solamente il 20% dei pazienti affetti risulta idoneo, e molto spesso si sviluppano recidive[1].

L'immunoterapia applicata al PDAC offre numerosi piani d'attacco, dato il caratteristico **profilo immunosoppressivo** del microambiente tumorale: l'infiltrato immunitario conta principalmente linfociti T $CD8^+$ inattivati, $CD4^+$ principalmente Treg con funzione immunosoppressiva, e cellule mieloidi, principalmente macrofagi tumore-associati (TAMs). I macrofagi, polarizzati verso un profilo antinfiammatorio, hanno diverse proprietà pro-tumorali: sopprimono la risposta immunitaria adattativa, favoriscono la transizione epitelio-mesenchimale per la formazione di metastasi, aumentano l'angiogenesi e il rimodellamento del tessuto connettivo stromale.

Alcuni approcci di immunoterapia prevedono l'utilizzo di vaccini o l'inibizione degli immuno-checkpoint, nello specifico di PD1–PD-L1, per aumentare l'attività tumoricida dei linfociti T. Questo approccio risulta tuttavia inefficace, probabilmente a causa del basso tasso di mutazione in PDAC che risulta in una mancanza di neoantigeni tumorali, riconosciuti come non-self dal sistema immunitario adattativo e capaci di scatenare una risposta T-citotossica antigene-specifica[2].

1.2. Microbiota e tumore al pancreas

Il termine microbiota comprende l'insieme dei microrganismi che risiedono in un determinato distretto anatomico del nostro organismo: tra questi, il microbiota più studiato e ricco risulta essere quello intestinale.

In contesto fisiologico il microbiota intestinale svolge numerose funzioni benefiche per l'ospite, come la partecipazione al metabolismo, la regolazione del sistema immunitario e la formazione di una barriera di difesa iniziale contro l'infezione da parte di patogeni estranei[3].

L'alterazione degli equilibri all'interno del microbiota, fenomeno conosciuto come **disbiosi**, può contribuire all'insorgenza di numerose patologie. Il microbiota intestinale è spesso studiato in contesti tumorali, per la sua contribuzione alla definizione del profilo immunologico del TME e alla modulazione della risposta tumorale ai trattamenti con chemioterapici. Nel caso di tumore al pancreas PDAC, sono state riscontrate differenze nella composizione del microbiota intestinale tra pazienti LTS (long-term survivor) e pazienti STS (short-term survivor), con i primi caratterizzati da maggiore variabilità microbica, profilo pro-infiammatorio del TME ed aumento dell'infiltrato immunitario in cellule antitumorali[3,4].

Il microbiota risulta quindi essere un possibile target terapeutico per aumentare la responsività ad altri trattamenti o per stimolare l'attività antitumorale delle cellule immunitarie. Una tecnica di terapia recentemente sviluppata è il trapianto di microbiota fecale (FMT): questo consiste nella sostituzione del microbiota di un paziente con quello di un donatore, caratterizzato da una migliore responsività ad altri trattamenti e da una migliore prognosi. Il FMT ha permesso di evidenziare come differenze nella risposta a lungo termine a trattamenti antitumorali possano essere correlate alla variabilità di specie che compongono il microbiota intestinale. Inoltre, il trapianto di microbiota fecale da paziente LTS in topo PDAC comporta una riduzione della massa tumorale, mentre il trapianto da STS è associato ad una peggiore prognosi, con crescita del tumore ed aumento delle popolazioni di Treg immunosoppressori[4].

1.3. Recettore degli idrocarburi arilici – AhR

Il recettore degli idrocarburi arilici (**AhR**) è un recettore citoplasmatico ed un fattore di trascrizione attivato da ligando, codificato dal gene *Ahr*. Il recettore appartiene alla famiglia dei bHLH (basic helix-loop-helix), presenta un dominio N-terminale bHLH di legame con ligando, un dominio C terminale variabile ed un

dominio PAS (PER-ARNT-SIM) di legame al DNA. In assenza di ligando, AhR è sequestrato nel citoplasma da un complesso proteico composto da HSP90 e XAP2 (proteina interagente con AhR) che ne previene la degradazione. In seguito a legame con ligando, AhR trasloca nel nucleo dove eterodimerizza con la proteina **ARNT**, traslocatore nucleare degli idrocarburi arilici. L'eterodimero AhR/ARNT agisce da **fattore di trascrizione** regolando l'espressione genica di numerosi geni, a seconda del ligando di attivazione[5,6].

Una delle classi più interessanti di ligandi che attivano AhR sono gli **indoli**, tra cui acido indol-3-acetico (IAA), aldeide-3-indolo (IAld) e acido-3-indol-lattico (ILA), idrocarburi aromatici derivati dal metabolismo del triptofano dell'ospite e del microbiota intestinale. Questi agonisti attivano AhR per modulare l'espressione di geni coinvolti nella definizione del profilo immunologico tissutale, guidando il fenotipo di linfociti T e di cellule della linea mieloide verso un profilo immunosoppressorio[6,7].

In condizioni fisiologiche, a livello intestinale l'attivazione di AhR favorisce il differenziamento di linfociti T $CD4^+$ naive verso un profilo Treg e Th17, benefico all'attenuazione dello stato infiammatorio intestinale.

In contesto tumorale, specificatamente nel PDAC, l'attivazione di AhR mediante indoli prodotti dal microbiota intestinale modifica l'infiltrato immunitario, che acquisisce un profilo immunologico antinfiammatorio: è stato osservato come questo correli con un aumento della massa tumorale ed un peggioramento della prognosi in topo. L'azione di AhR guida i TAM verso uno shift funzionale di carattere pro-tumorale, antinfiammatorio, caratterizzato dall'espressione di geni marker come IL-10, TGFα, TGFβ e arginasi; inoltre, l'espressione di AhR nei linfociti T $CD8^+$ ne inibisce l'azione citotossica e l'espressione di IFNγ[6,7].

Dato il contributo di AhR nella modulazione dell'immunità tumorale, risulta interessante studiare come variazioni nell'espressione e nell'attività, mediata da indoli microbici, di questo recettore possano indurre modificazioni nel profilo immunologico del TME, nella crescita tumorale e nella sopravvivenza dei pazienti oncologici.

2. APPROCCIO SPERIMENTALE

2.1. Modelli sperimentali

Per lo svolgimento degli esperimenti sono state utilizzate diverse linee di topo, ottenute dai Jackson Laboratories e mantenuti in condizioni germ-free da una struttura di cura animale al Princess Margaret Cancer Centre. Le linee utilizzate sono C57BL6/J (B6), B6.Ido$^{-/-}$, B6.Ahr$^{fl/fl}$, B6.Lyz2CRE$^{+/-}$. Tutti i topi utilizzati erano femmine di età compresa tra le 10 e le 12 settimane.

2.2. Impianto del tumore ed induzione del tumore

L'impianto ortotopico del tumore nel pancreas è avvenuto tramite incisione laterale della parete addominale del topo, precedentemente anestetizzato con isoflurano al 2% in ossigeno. Sono state impiantate nel pancreas $10x10^3$ cellule derivanti da linee primarie di organoidi di adenocarcinoma pancreatico mT3, mT4 e mT5, risospese in 80 µl di matrigel diluito 1:4 in PBS.

Lo sviluppo del tumore è stato monitorato tramite palpazione ed i topi sono stati sacrificati a due settimane dall'impianto. Dal sacrificio sono stati estratti per ulteriori analisi campioni di tumore, di intestino tenue, di feci e di sangue.

2.3. Isolamento dei batteri dall'intestino murino

I ceppi batterici *L. murinus*, *L. intestinalis*, *L. reuteri* e *L. johnsonii* sono stati isolati dall'intestino di topi B6 tramite coltura in condizioni anaerobiche su terreno MRS. Le colonie isolate sono state caratterizzate tramite amplificazione con PCR del gene 16S, con seguente step di pulizia e sequenziamento Sanger. La caratterizzazione delle specie è stata svolta mediante allineamento della sequenza 16S usando BLASTn sul database di NCBI, con soglia di associazione al 99,5%.

2.4. Trattamento con antibiotico per rimuovere il microbiota

Per eliminare il microbiota intestinale i topi sono stati trattati con un cocktail di antibiotici, contenente ampicillina 1 g/l, metronidazolo 1 g/l, neomicina 1 g/l e vancomicina 0.5 g/l disciolti in acqua, cambiato quotidianamente durante la sperimentazione. A tre giorni dall'inizio del trattamento è stato impiantato il tumore ortotopico.

2.5. Trapianto di microbiota in topi SPF

Le femmine B6 sono state trattate con una soluzione ATBx contenente streptomicina 5 mg/ml e clindamicina 0.1 mg/ml disciolte in acqua sterile per due settimane, con cambio di bottiglie e soluzioni tre volte alla settimana. Dopo due settimane di trattamento con ATBx ai topi sono state somministrate colture di *L.murinus* + *L.reuterii* o *L.intestinalis* + *L.johnsonii*: la dose giornaliera conteneva circa 10^8 CFU per 200 µL. Le colture batteriche sono state somministrate oralmente, mediante un ago apposito, tre volte al giorno prima dell'impianto del tumore ortotopico, poi una volta a settimana fino alla fine dell'esperimento.

2.6. scRNA-sequencing e analisi

Il sequenziamento single-cell dell'RNA è una tecnica omica di nuova generazione che permette di analizzare i profili di espressione a livello di singola cellula, distinguendo tipi cellulari all'interno di un campione di analisi eterogeneo. Le

cellule vengono separate singolarmente prima di procedere con lo step di retrotrascrizione dell'RNA in cDNA, per sequenziare successivamente con tecniche di NGS. Le tecniche più moderne prevedono l'utilizzo di sequenze **barcode**, cellulo-specifiche, da associare al cDNA per assegnare una data reads ad una singola cellula.

Nell'articolo in esame i tumori di tre topi sono stati digeriti, raggruppati e colorati con il DAPI per selezionare le cellule vive. Successivamente sono stati svolti lavaggi con PBS + 0.04% BSA e sono state selezionate $10x10^3$ cellule per procedere con la sintesi single-cell del cDNA, utilizzando il kit *10X Genomics Chromium single-cell RNA master mix*. Successivamente è stato svolto un sequenziamento delle librerie con un sequenziatore *Novaseq* (Illumina). I risultati del sequenziamento sono stati suddivisi in singole reads, convertiti in formato FASTQ e processati con il software *Cell Ranger Single-Cell.* Il software ha permesso di allineare le reads ad un genoma murino di riferimento (GRCm38/mm10) e di associarle a geni e singole cellule in base alla sequenza barcode. Sono stati utilizzati noti marcatori superficiali espressi almeno nel 25% delle cellule di ogni cluster per associare il raggruppamento ad un determinato tipo cellulare, sia in topi WT che $Lyz2^{cre/+}Ahr^{fl/fl}$. È stata svolta un'analisi di espressione genica differenziale tra le cellule dei due modelli, visualizzata tramite *violin pots*.

2.7. Coltura di organoidi PDAC

Sono state allestite co-colture di organoidi PDAC con macrofagi umani trattati con IAA (acido indol-3-acetico) per visualizzare l'effetto di questi sulla crescita dell'organoide. I macrofagi derivati dai monociti sono stati messi in coltura con hM-CSF per 5 giorni, per essere poi divisi in due gruppi, uno di controllo ed uno trattato overnight con IAA. I macrofagi sono stati raccolti dalle piastre usando PBS + 2% FBS + 2mM EDTA, colorati con il DiD per 5 minuti a 37°C e lavati con terreno di coltura.

Per allestire la co-coltura gli organoidi marcati con GFP sono stati fatti crescere per 4 giorni in matrigel, e successivamente raccolti per piastrarli con i macrofagi. Per raccogliere gli organoidi si sono liberati dalla goccia di matrigel tramite pipettamento, per essere poi centrifugati in Advanced DMEM freddo; il matrigel nel pellet è stato depolimerizzato tramite una soluzione di lavaggio. La co-coltura è durata 5 giorni ed è stata allestita utilizzando il sistema *24-GLAnCE*, una piattaforma di co-coltura che permette di studiare le interazioni tra diversi tipi cellulari, avvicinandosi alle condizioni in vivo[8]. Per analizzare i profili di espressione genica dei macrofagi e degli organoidi, le cellule sono state selezionate in base alla positività al GFP (organoidi) o a CD45 (macrofagi). In seguito al *sorting* cellulare i pool di cellule sono stati sospesi in un buffer di lisi RNA per estrarre l'acido nucleico e procedere con le analisi di trascrittomica.

2.8. Citofluorimetria

La citofluorimetria è una tecnica biomedica utilizzata per l'analisi multiparametrica di singole cellule presenti in un campione, in base alle caratteristiche morfologiche

ed ai marcatori espressi, grazie all'utilizzo di un laser. Per fenotipizzare le cellule in base ai marcatori espressi si utilizzano anticorpi specifici per i marker, associati ad un fluoroforo che emette a determinate lunghezze d'onda. L'utilizzo di fluorofori di colori diversi e con spettri di assorbimento differenti permette di analizzare contemporaneamente molti marcatori superficiali e citoplasmatici, ottenendo una chiara categorizzazione delle cellule presenti nel campione[9].

La caratterizzazione cellulare si basa sulle modalità di dispersione della luce laser incidente e sulle fluorescenze legate agli anticorpi. La dispersione della luce frontale e laterale permette di analizzare la morfologia cellulare e la sua complessità citoplasmatica, in termini di granuli ed organelli presenti: l'analisi morfologica è utile per distinguere inizialmente cellule con strutture molto diverse e per osservare la formazione di aggregati cellulari. Le analisi di fluorescenza permettono di caratterizzare meglio le cellule, distinguendo tipi cellulari e profili funzionali in base alle molecole espresse. I risultati sono visualizzati tramite grafici bidimensionali dove le cellule si distribuiscono sulla base dei valori relativi per ognuna delle due caratteristiche analizzate. È possibile selezionare sottopopolazioni cellulari su cui svolgere analisi più approfondite, considerando altri marcatori di polarizzazione[9].

In immunologia questa tecnica è frequentemente utilizzata per definire il profilo immunitario di campioni di sangue o di tessuto solido, in contesti tumorali o di infezione[9].

Nell'articolo sono stati digeriti i tumori PDAC usando collagenasi IV 100U/ml e DNasi I 50u/ml in RPMI a 37°C per ottenere singole cellule. Queste sono state marcate con un cocktail di anticorpi anti-CD45, anti-CD11b, anti-F4/80 ad una concentrazione 1:300 in una soluzione FACS (PBS + 2% FBS) per 45 minuti a 4°C, con un marcatore di vitalità cellulare.

Sono seguiti lavaggi in soluzione FACS, poi fissazione delle cellule in paraformaldeide al 4% per 10 minuti ed ulteriore lavaggio. Per marcare le citochine intracellulari le cellule sono state trattate con PMA (5 ng/ml) per 4 ore e ionomicina (500 ng/ml) in presenza di Brefeldin A. Per le analisi al citofluorimetro *BD Fortessa* sono stati contati almeno 10^5 eventi per tubino, per avere omogeneità di analisi.

2.9. Citometria di massa in base al tempo di volo (CyTOF)

La citometria di massa in base al tempo di volo è una tecnologia recente che si evolve dalla citofluorimetria per la tipologia di anticorpi utilizzati nella marcatura delle cellule. In CyTOF gli anticorpi sono coniugati con metalli rari, tipicamente della famiglia dei Lantanidi, come il platino: non essendo presenti questi metalli nelle cellule di mammifero, questa tecnica permette di eliminare l'autofluorescenza delle cellule e presenta un risultato più pulito. Inoltre, anticorpi associati al platino permettono una possibilità di combinazione maggiore, per un'analisi multiparametrica potenziata. Le cellule sono incubate con anticorpi specifici per i diversi marcatori e questi vengono quantificati simultaneamente utilizzando i

principi della spettrometria di massa. In questo caso gli anticorpi sono associati a cis-platino per permettere la ionizzazione delle cellule etichettate; successivamente l'analisi viene fatta utilizzando un quadrupolo ed un sistema ToF (Time of Flight), secondo cui le particelle vengono separate in base alla velocità necessaria per raggiungere il rilevatore, dipendente dal rapporto m/z (massa su carica)[10].

Nell'esperimento svolto dagli autori dell'articolo sono state analizzate le cellule $CD45^+$ (leucociti) presenti nei tumori ortotopici PDAC, selezionate positivamente con un kit e con anticorpi anti-CD45 associati a biotina. Per essere analizzate al CyTOF, le cellule devono seguire diversi step di preparazione. Le cellule arricchite sono state bloccate con una soluzione di blocco Fc di *TruStain* per 10 minuti, per essere poi risospese in una soluzione di colorazione contenente il cocktail di anticorpi. Le cellule marcate sono state lavate ed incubate in 1 µM di cisplatino *Cell_Id* per 5 minuti. Il cisplatino è stato poi neutralizzato con PBS + 5% FBS. Le cellule sono state lavate, fissate, permeabilizzate e associate ad un barcode con il *Cell_ID multiplex Barcoding kit*. In seguito a permeabilizzazione le cellule sono state incubate con anticorpi citoplasmatici usando il kit di colorazione Foxp3. Infine, le cellule sono state lavate, risospese in PBS + 1,6% paraformaldeide + 0.3 % saponina + 125 nM Iridium. Le cellule sono state mantenute in questa soluzione a 4°C fino al giorno dell'analisi di CyTOF.

2.10. Dieta priva di triptofano e somministrazione degli indoli

Il giorno prima dell'iniezione del tumore ortotopico, i topi sono stati nutriti con una dieta amminoacidica di controllo o priva di triptofano, che è stata mantenuta per tutti i 14 giorni dell'esperimento, fino al sacrificio. In uno degli esperimenti i topi sono stati nutriti con 40 µg/kg di IAA, IAld o ILA disciolto in 200 µl di acqua, ogni giorno a partire da 4 giorni prima dell'iniezione del tumore ortotopico.

2.11. Sequenziamento dell'RNA 16S

Il sequenziamento del gene dell'RNA 16S è una tecnica di biologia molecolare utile al riconoscimento ed alla caratterizzazione delle specie microbiche presenti in un dato campione. Nel caso dell'articolo, questa tecnica è stata utilizzata per determinare le specie microbiche che andavano a comporre il microbiota intestinale in condizioni sperimentali diverse. La tecnica permette infatti di distinguere le diverse specie batteriche in base alle caratteristiche del gene 16S, conservato nei procarioti ma che presenta differenze, principalmente associate alla regione ipervariabile V4, che permettono la discriminazione specie-specifica.

Nell'esperimento in esame sono stati svolti sequenziamenti multipli grazie all'utilizzo di primer di sequenziamento con barcode.

Mix di PCR	
Reagente	*Volume*
ReadyMix KAPA2G Robust HotStart	12,5 µl
Primer forward (10 µM)	1,5 µl
Primer reverse (10 µM)	1,5 µl
Acqua sterile	7,5 µl
Campione	2 µl

Programma di PCR		
Step	*T (°C)*	*T*
Denaturazione iniziale	95	3 min
Cicli di amplificazione (18x-24x)		
Denaturazione	95	15 sec
Annealing	50	15 sec
Estensione	72	15 sec
Estensione finale	72	5 min

Le amplificazioni sono state svolte in triplicato ed il risultato è stato verificato con elettroforesi in gel di agarosio 1% in TBE. I campioni triplicati sono stati quantificati, poi sequenziati su un *Illumina MiSeq* in seguito a purificazione con beads *Ampure XP*. Nel sequenziamento sono stati inclusi anche una specie singola (*Pseudomonas aeruginosa*), una comunità simulata e un controllo negativo, privo di campione.

2.12. Analisi statistica e quantificazione

I risultati ottenuti dagli esperimenti riportati nell'articolo sono stati analizzati statisticamente con il programma *GraphPad Prism 8*, mentre per calcolare la significatività statistica sono stati utilizzati t-test, test di Wilcoxon, test ANOVA o analisi di Kaplan-Meier seguite da test del log-rank.

Le barre di errore rappresentano la deviazione standard e i p-value < 0.05 sono stati considerati statisticamente significativi (* $p < 0.05$, ** $p < 0.01$, *** $p < 0.001$, **** $p < 0.0001$, NS = non significativo).

3. RISULTATI E DISCUSSIONE

3.1. La delezione di AhR determina una polarizzazione infiammatoria dei TAM e dei CD8+ nel TME di PDAC

I macrofagi intratumorali esprimono maggiormente numerosi geni antinfiammatori rispetto ai macrofagi residenti nel tessuto sano: tra questi, anche il gene *Cyp1b1*, associato direttamente all'attività di AhR (dato non mostrato). Per verificare che AhR sia correlato all'immunosoppressione nel PDAC, i ricercatori hanno ottenuto modelli murini Ahr^{-} tramite delezione condizionale del gene nelle cellule del lineage mieloide (Lyz2$^{cre/+}$Ahr$^{fl/fl}$).

Dalle analisi di citofluorimetria sono state osservate differenze nella composizione dell'infiltrato immunitario tumorale tra topi WT e topi Ahr^{-}. La delezione di AhR nei TAM ha ridotto la loro rappresentazione relativa all'interno dei leucociti (CD45^{+}), seppur non influenzando il numero totale di TAM presenti nell'infiltrato. Inoltre, nei macrofagi dei topi deleti si è osservato un aumento dell'espressione di MHCII, CD40 e PD-L1, indice di una maggiore attività cellulare. Anche la proporzione di linfociti T CD8^{+} nel TME è aumentata, così come la loro attività, dimostrata dall'incremento di cellule effettrici o della memoria (CD62L^{neg}CD44^{hi}) (Fig. 1A).

Anche il profilo trascrizionale dei TAM Ahr^{-} risulta fortemente alterato rispetto a quello dei macrofagi WT: le analisi di trascrittomica hanno evidenziato l'espressione differenziale di numerosi geni che definiscono un profilo trascrizionale meno immuno-regolatorio (down-regolazione di *Arg1* e *Ido1*) e più pro-infiammatorio (up-regolazione di *Il1b*, *Gzb* e geni *MHCII*) (Fig. 1B).

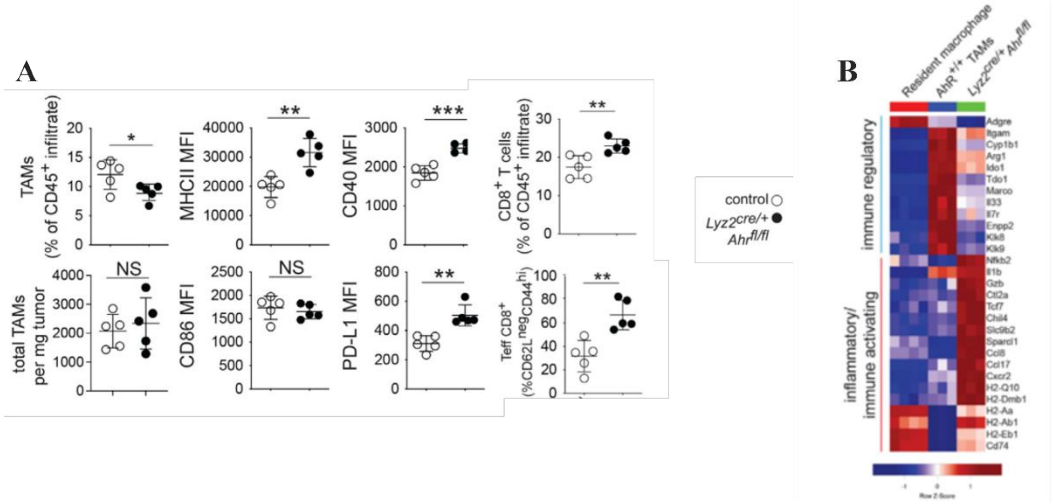

Fig. 1: La delezione di AhR determina una polarizzazione infiammatoria dei TAM e dei linfociti CD8^{+} nel TME di PDAC. (A) Espressione di marcatori superficiali e percentuali di TAM e CD8^{+} in campioni tumorali di topi di controllo e Lyz2$^{cre/+}$Ahr$^{fl/fl}$, ottenuti al citofluorimetro. *MFI = mean fluorescent intensity.* **(B)** *Heatmap* che mostra le differenze di espressione di marcatori immunoregolatori e pro-infiammatori in macrofagi tissutali, TAM di topi WT e TAM di topi Lyz2$^{cre/+}$Ahr$^{fl/fl}$. In rosso sono indicati i geni sovraespressi, in blu quelli sottoespressi. * *p-value* < *0.05*

A livello macroscopico, l'impianto di cellule di PDAC in topi deleti per Ahr ha portato, dopo 14 giorni, alla formazione di una massa tumorale di minor entità, associata ad un tasso di sopravvivenza superiore rispetto ai topi di controllo (Fig. 2A e B).

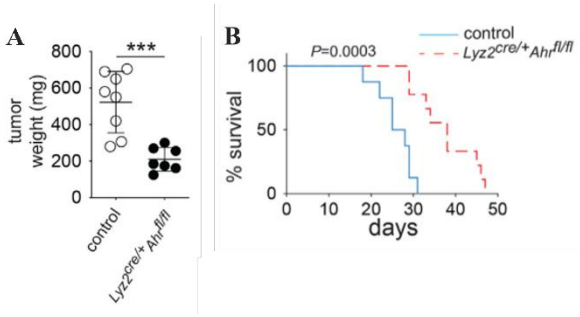

Fig. 2: La delezione di AhR determina una minor crescita tumorale e maggiore percentuale di sopravvivenza nei modelli murini. (A) Peso della massa tumorale a 14 giorni dall'iniezione, in topi di controllo (WT) e topi Lyz2$^{cre/+}$Ahr$^{fl/fl}$. **(B)** Curve di sopravvivenza di topi con tumore, WT o Lyz2$^{cre/+}$Ahr$^{fl/fl}$, su un campione di 8 topi per genotipo. *** *p-value < 0.001.*

3.2. Inibizione farmacologica di AhR promuove l'infiammazione nel TME e migliora la risposta alla terapia

Dai risultati ottenuti tramite delezione condizionale di Ahr nei TAM è stata estrapolata la funzione di questo recettore nella definizione del profilo immunologico del microambiente tumorale. Gli studiosi hanno quindi utilizzato un altro modello per verificare che si ottenessero risultati concordi ai precedenti: in questo caso i topi sono stati trattati con un inibitore farmacologico di Ahr, **CH223191**. Dopo 14 giorni di trattamento farmacologico, sono stati analizzati i campioni tumorali in citofluorimetria, focalizzandosi sugli stessi parametri considerati nell'esperimento precedente. In seguito a trattamento, i TAM presentavano una polarizzazione più pro-infiammatoria, con aumento di espressione di MHCII, CD40 e PD-L1. Inoltre, la popolazione linfocitaria CD8$^+$ all'interno delle cellule CD45$^+$ è risultata maggiormente rappresentata rispetto ai controlli (Fig. 3).

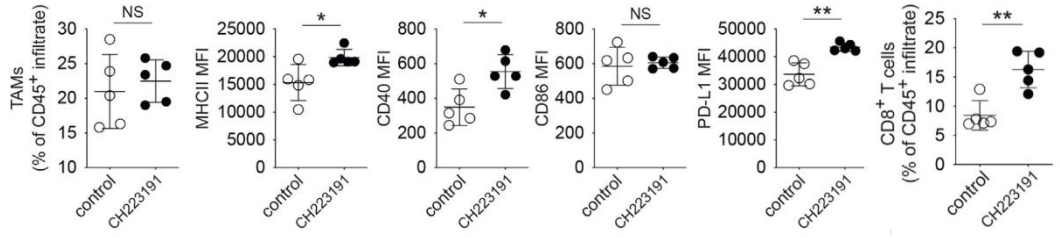

Fig. 3: L'inibizione farmacologica di AhR promuove l'infiammazione nel TME e migliora la risposta alla terapia. Espressione di marcatori superficiali e proporzioni di TAM e CD8$^+$ in campioni tumorali di topo WT e Lyz2$^{cre/+}$Ahr$^{fl/fl}$, ottenuti al citofluorimetro. * *p-value < 0.05,* ** *p-value < 0.01.*

Per verificare che il ruolo principale di modulazione dell'immunità del TME sia svolto dai TAM in base all'espressione di AhR, una coorte di topi Lyz2$^{cre/+}$Ahr$^{fl/fl}$ è stata trattata con CH223191 e dopo 14 giorni è stata misurata la massa tumorale. Comparando le masse tumorali di topi di controllo (WT e Lyz2$^{cre/+}$Ahr$^{fl/fl}$) e trattati farmacologicamente (WT e Lyz2$^{cre/+}$Ahr$^{fl/fl}$) si può osservare come la massa

tumorale sia ridotta in seguito a trattamento con CH223191 nei topi WT, mentre questa rimane invariata nei topi Ahr^{-} (Fig. 4A, 4B).

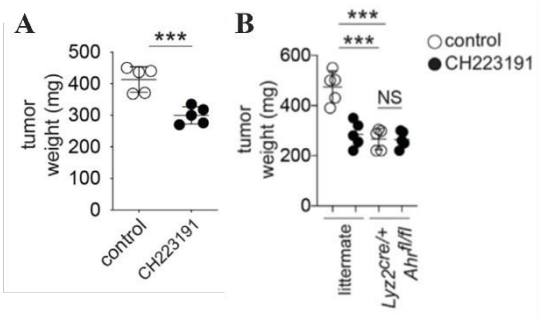

Fig. 4: L'inibizione farmacologica di AhR riduce la crescita tumorale nei modelli murini. (A) Peso delle masse tumorali dopo 14 giorni dall'iniezione in modelli murini WT, trattati o meno con CH223191. **(B)** Peso delle masse tumorali dopo 14 giorni dall'iniezione in modelli murini WT e Lyz2$^{cre/+}$Ahr$^{fl/fl}$, trattati o meno con CH223191. *** *p-value < 0.001.*

Si può dedurre che l'effetto principale sulla crescita tumorale è svolto da AhR nei TAM e che, in caso di delezione condizionale, l'inibizione farmacologica del recettore non contribuisce ulteriormente alle differenze fenotipiche osservate.

Dai risultati ottenuti si nota come, sebbene i TAM in cui l'espressione di Ahr è inibita presentino una polarizzazione più pro-infiammatoria, risulta sovraespresso il gene PD-L1, che ha una funzione inibitoria dell'immunità adattativa. PD-L1 (*Programmed Cell Death protein 1 ligand*) costituisce, legandosi a PD-1, uno degli immuno-checkpoint che implicano una riduzione della proliferazione dei linfociti T e della loro attività infiammatoria di rilascio di citochine[11].

I ricercatori hanno voluto indagare un potenziale effetto dell'inibizione combinata di AhR e PD-L1 sulla sopravvivenza dei topi, in questo caso utilizzando un anticorpo αPD-L1. L'inibizione singola di uno dei due recettori ha portato ad un aumento della sopravvivenza nei modelli murini, ma l'effetto maggiore si è ottenuto con la doppia inibizione di AhR e PD-L1: la sopravvivenza è doppia rispetto ai controlli ed aumentata del 50% rispetto all'inibizione di un singolo recettore (Fig. 5).

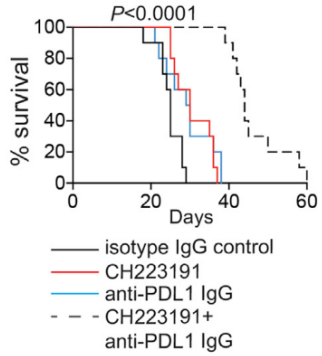

Fig. 5: L'utilizzo combinato di inibitori di AhR e PD-L1 aumenta la sopravvivenza dei modelli murini tumorali. Curve di sopravvivenza di topi trattati con CH223191, con anti-PDL1, o una combinazione dei due. Sono stati utilizzati 10 topi per gruppo.

3.3. L'attività di AhR dei macrofagi modella il profilo trascrizionale nel PDAC

Per capire che impatto avesse l'attività di AhR dei TAM sul microambiente tumorale, i ricercatori hanno caratterizzato l'infiltrato del TME utilizzando la tecnologia CyTOF (citometria di massa in base al tempo di volo). Questo approccio ha permesso di individuare e distinguere 32 cluster di cellule immunitarie a comporre l'infiltrato immunitario nel PDAC, in base all'espressione differenziale

di marcatori di superficie e citoplasmatici (Fig. 6A). Focalizzandosi sui macrofagi, l'analisi al CyTOF ha identificato tre cluster F4/80^{+} (marker macrofagico), chiamati cluster 12, 13 e 22. Il cluster 22 presentava una polarizzazione immuno-regolatoria, con l'espressione di CD206 e PD-L1, e possibile origine monocitica, per l'espressione di Ly6C. Gli altri due cluster macrofagici, 12 e 13, risultavano Ly6C^{neg} e si differenziavano tra loro per l'espressione di PD-L1, MHCII e Ly6G, maggiore nel cluster 12 (Fig. 6B).

Nel paragone tra TME di topi Ahr^{-} e WT non si è osservata una differenza nella distribuzione dei cluster cellulari, ma si è osservata una variazione nei profili funzionali dei macrofagi appartenenti ai cluster 12, 13 e 22. Specificatamente, l'inibizione dell'attività di AhR è correlata ad una minore espressione di iNOS, CCL4 e TNFα, geni solitamente espressi in cellule con attiva funzionalità infiammatoria, mentre nel cluster 22 si è osservato un aumento di espressione di MHCII (Fig. 6C).

Questi dati, seppur inizialmente contrastanti con i risultati precedentemente ottenuti, sono da interpretare come indice di una variazione funzionale complessa in seguito all'inibizione di AhR nella polarizzazione dei TAM. La complessità funzionale è espressa anche dalle diversità di espressione tra diversi cluster macrofagici, evidenziando quanto risulti complicato categorizzare una cellula entro definiti profili funzionali (proinfiammatori o protumorali). In generale, le analisi al CyTOF hanno evidenziato come le diverse popolazioni macrofagiche presentino polarizzazioni protumorali alternative.

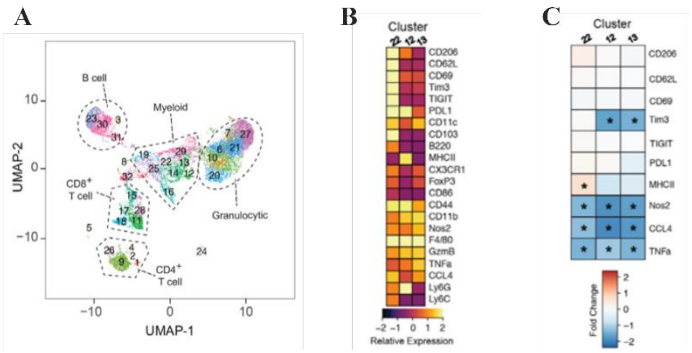

Fig. 6: L'attività di AhR dei macrofagi modella il profilo trascrizionale del PDAC. (A) Grafico UMAP ad indicare le diverse sottopopolazioni cellulari nell'infiltrato immunitario di PDAC, ottenuto tramite CyTOF. **(B)** *Heatmap* riguardo l'espressione relativa di marcatori in 3 cluster macrofagici, in modelli murini tumorali WT e Lyz2$^{cre/+}$Ahr$^{fl/fl}$. **(C)** Mappa di calore sull'espressione relativa di marcatori cellulari nei 3 cluster macrofagici tra topi WT e Lyz2$^{cre/+}$Ahr$^{fl/fl}$. In blu è indicata una sottoespressione, in rosso una sovraespressione.

Le analisi di scRNA-seq sulle popolazioni cellulari nel TME in PDAC hanno riportato risultati concordi con il CyTOF (dato non mostrato): sono stati identificati tre diversi cluster macrofagici caratterizzati da diversi stati di polarizzazione tendenzialmente pro-tumorali. Nel confronto tra cluster macrofagici in tumori Lyz2$^{cre/+}$Ahr$^{fl/fl}$ e tumori WT è emerso un significativo incremento dell'espressione di geni coinvolti nei *pathway* di risposta ad interferone-γ (IFN-γ) nella prima condizione, anche se con intensità variabile tra i diversi cluster.

IFN-γ è risultato sovraespresso, nei topi Ahr^{-}, anche nei cluster cellulari dei linfociti T CD8^{+}, sia a livello genico che proteico rispetto ai controlli (Fig. 7A, 7B).

Conoscendo il ruolo pro-infiammatorio di questa citochina, impiegata nella stimolazione dell'attività macrofagica, nel mantenimento del profilo funzionale Th1 dei linfociti T helper e nell'attivazione dei CTL[12], si sono indagati i possibili effetti dell'inibizione della sua attività sullo sviluppo del tumore. Gli sperimentatori hanno comparato le masse tumorali sviluppate a 14 giorni dall'iniezione, su modelli murini WT e Lyz2$^{cre/+}$Ahr$^{fl/fl}$, in seguito ad inibizione dell'attività dei linfociti CD8$^+$ (anti-CD8) o di IFN-γ (anti-IFNγ). Dai risultati è emerso come l'inibizione dei linfociti T citotossici o di IFN-γ non influenzasse la crescita tumorale in topi WT, dove la loro attività risulta soppressa dal microambiente tumorale. Al contrario, l'utilizzo di anticorpi anti-CD8 o anti-IFN-γ in topi deleti riporta la massa tumorale ai valori di controllo (Fig. 7C e D). Se ne deduce come l'attività dei CTL tramite il rilascio di IFN-γ contribuisca notevolmente allo switch pro-infiammatorio del microambiente tumorale in seguito all'inibizione di AhR nei TAM.

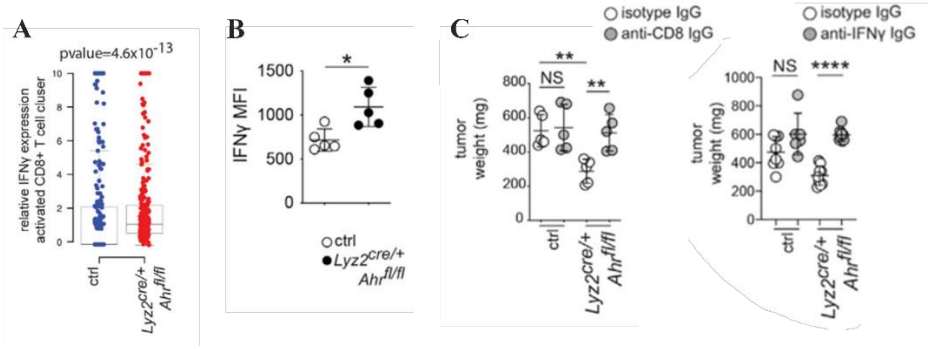

Fig. 7: L'attività AhR dei macrofagi modella il profilo trascrizionale del PDAC. (A) Espressione single-cell di IFN-γ nei cluster di linfociti T CD8$^+$**. (B)** Espressione intracellulare di IFN-γ in linfociti T CD8$^+$ di topi deleti e WT a 14 giorni dall'impianto di tumore valutata al citofluorimetro. I valori sono espressi come MFI (intensità media di fluorescenza). **(C)** Confronto delle masse tumorali in topi WT e deleti in seguito ad esaurimento dei linfociti T CD8$^+$ (pannello di sinistra) o ad inibizione di IFN-γ (pannello di destra). * *p-value* < *0.05; ** p-value* < *0.01; **** p-value* < *0.0001*.

3.4. La produzione di indoli da parte del microbiota guida la soppressione immunitaria nel TME e favorisce la crescita tumorale

Noto il ruolo del microbiota intestinale nella definizione del profilo immunitario del microambiente tumorale, i ricercatori hanno voluto indagare come l'influenza del microbiota su PDAC possa essere mediata dall'attività AhR nei TAM. Tra i ligandi attivatori di AhR si ritrovano infatti derivati del metabolismo microbico del triptofano, chiamati indoli. È stato quindi studiato il ruolo di specie batteriche indolo-producenti, come alcune appartenenti al genere *Lactobacillus*, nell'attivazione di AhR e modulazione dell'immunità tumorale. I topi sono stati trattati con **ampicillina**, microbicida su *Lactobacillus*, e **vancomicina**, cui questi batteri sono resistenti. Il microbiota trattato con Amp era caratterizzato da una maggiore diversità nella composizione in specie ed una minore rappresentazione di *Lactobacillus*, mentre l'opposto è stato osservato in seguito al trattamento con Vanc (dato non mostrato).

Il trattamento con Amp è risultato in una significativa riduzione della massa tumorale (Fig. 8A) ed un infiltrato tumorale più attivo e con profilo pro-infiammatorio. Nei TAM si è osservato un aumento della percentuale cellulare nell'infiltrato e dell'espressione di MHCII, PD-L1 e CD86 (Fig. 8B), mentre i linfociti T $CD8^+$ sono risultati maggiormente rappresentati. (Fig. 8C). Al contrario, il trattamento con Vanc non ha riportato differenze su questi parametri rispetto ai topi di controllo. I risultati sono concordi con quanto ottenuto dall'inibizione di AhR ed evidenziano una possibile correlazione tra microbiota, attivazione di AhR e modulazione dell'infiltrato.

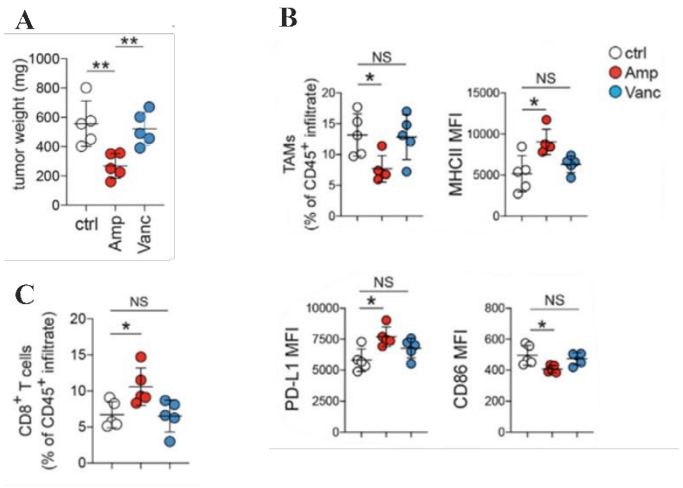

Fig. 8: La produzione di indoli da parte del microbiota guida la soppressione immunitaria nel TME e favorisce la crescita tumorale. (A) Confronto delle masse tumorali a 14 giorni dall'impianto in topi di controllo e trattati con Amp o Vanc. **(B)** Analisi in citofluorimetria dei TAM nelle condizioni riportate in legenda. **(C)** Analisi in citofluorimetria dei linfociti $CD8^+$ nelle condizioni riportate in legenda. * *p-value* < *0.05;* ** *p-value* < *0.01.*

Per caratterizzare meglio il ruolo del microbiota nel PDAC, sono state analizzate e testate nella produzione di indoli quattro specie di *Lactobacillus*, *L. murinus*, *L. reuterii*, *L. johnsonii* e *L. intestinalis*. Tra queste, *L. murinus* e *L. reuterii* sono risultate le più indolo-producenti, con produzione di ILA (acido 3-indol-lattico) e IAld (indolo-3-aldeide) (dati non mostrati).

I ricercatori hanno proceduto con un trapianto di microbiota su topi germ-free per verificare che la composizione batterica, e nello specifico in batteri indolo-producenti come *L. murinus* e *L. reuterii*, influenzasse lo sviluppo tumorale in PDAC. Ad una coorte di topi è stato trapiantato un microbiota indolo-producente con *L. murinus* e *L. reuterii* (*L. m/r*), mentre un altro gruppo è stato trapiantato con un microbiota contenente *L. intestinalis* e *L. johnsonii* (*L. i/j*). Successivamente al trapianto è partita la tumorigenesi e dopo 14 giorni sono stati analizzati i tumori e gli infiltrati immunitari. Nei topi *L. i/j* è stata riscontrata una crescita tumorale significativamente ridotta rispetto ai topi *L. m/r*, (Fig. 9A) accompagnata da un'alterazione pro-infiammatoria del TME. Nello specifico, tumori da topi *L.i/j* erano più ricchi in linfociti T $CD8^+$, con una composizione maggiore di $CD8^+$ effettori ed esprimenti TNF-α, mentre non si sono riscontrate differenze per i TAM (Fig. 9B e C). Per verificare che la differenza in termini di sviluppo tumorale tra le due coorti dipendesse dall'attività di AhR indotta dagli indoli l'esperimento è stato riproposto utilizzando topi $Lyz2^{cre/+}Ahr^{fl/fl}$. La delezione di AhR mostrava differenze nella crescita tumorale di topi *L. m/r*, mentre nell'altra coorte non si sono riscontrate differenze tra topi WT e deleti. Questo risultato dimostra come la

presenza di indoli contribuisca significativamente all'attivazione di AhR nei TAM (Fig. 9D).

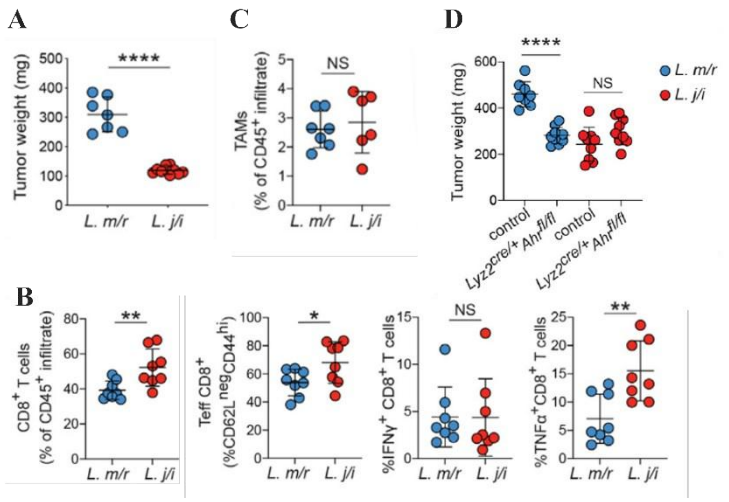

Fig. 9: La produzione microbica di indoli guida la soppressione immunitaria nel TME e favorisce la crescita tumorale. (A) Peso della massa tumorale a 14 giorni dall'impianto in topi WT trapiantati con *L. i/j* o *L. m/r*. **(B)** Proporzioni relative delle sottoclassi di linfociti T $CD8^+$ negli infiltrati di topi *L. m/r* e *L. i/j*. ** p-value < 0.05; ** p-value < 0.01; **** p-value < 0.0001.* **(C)** Proporzione relativa di TAM negli infiltrati di topi *L. m/r* e *L. i/j*. **(D)** Confronto delle masse tumorali a 14 giorni dall'impianto in topi WT e $Lyz2^{cre/+}Ahr^{fl/fl}$ con microbiota *L. m/r* o *L. i/j*. ***** p-value < 0.0001.*

3.5. Il triptofano e gli indoli IAA e ILA nella dieta promuovono l'immunosoppressione e la crescita del tumore al pancreas

Definita una possibile correlazione tra il microbiota intestinale e l'attivazione di AhR nei TAM, è stato verificato il ruolo del triptofano e degli indoli in questa relazione. L'eliminazione del triptofano dalla dieta di modelli murini tumorali ha determinato uno sviluppo tumorale rallentato, con tumori due volte più piccoli rispetto a quelli in topi di controllo. Per verificare che questo risultato derivasse da una produzione ridotta di indoli, i topi Trp^- sono stati alimentati con una dieta ricca di indoli, e questo ha riportato i valori ai controlli Trp^+ (Fig. 10A). Dall'analisi dell'infiltrato immunitario in topi Trp^- e Trp^+ si osserva un incremento nelle popolazioni linfocitarie $CD8^+$ e sottopopolazioni $TNF\alpha^+$ $IFN\gamma^+$ $CD8^+$ in assenza di Trp, mentre i TAM risultano meno presenti e con fenotipo meno attivato (Fig. 10B), con una riduzione dell'espressione di MHCII e di geni associati all'immunosoppressione come *Cyp1b1*, *Arg1* e *Il10* (Fig. 10C). In tutte queste analisi, la somministrazione di indoli in topi Trp^- ha abrogato l'effetto della dieta, riportando i valori agli standard di controllo.

Da questi risultati se ne deduce che il triptofano svolge un ruolo fondamentale nella definizione del profilo immunologico del TME in PDAC per mezzo della metabolizzazione ad indoli svolta dal microbiota.

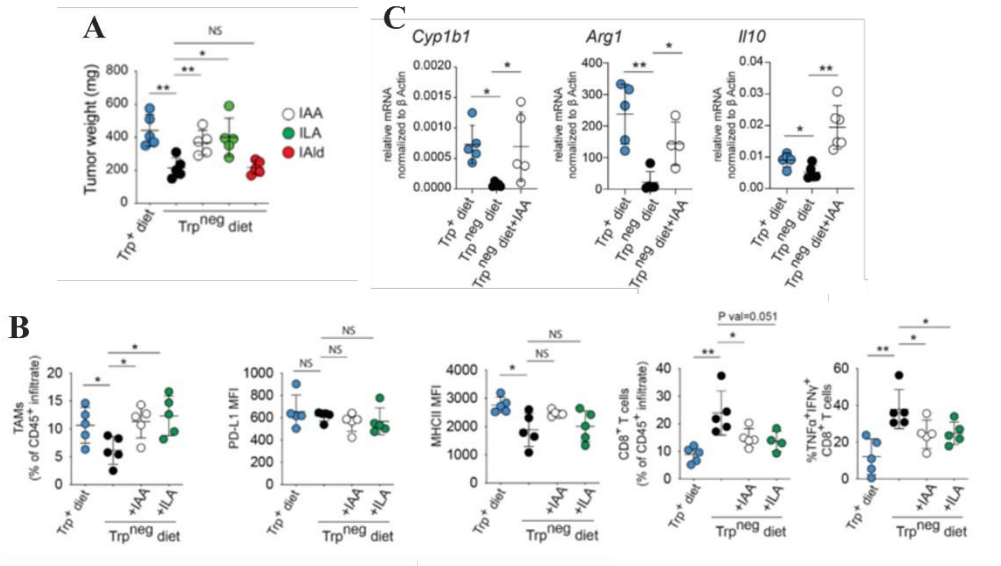

Fig. 10: Il triptofano e gli indoli IAA e ILA nella dieta promuovono l'immunosoppressione e la crescita di PDAC. (A) Peso delle masse tumorali in topi cui è stata somministrata una dieta Trp^+, Trp^- o Trp^- con aggiunta di IAA, ILA o IAld. **(B)** Espressione di marcatori superficiali e proporzioni relative nell'infiltrato di TAM e $CD8^+$ in topi WT in dieta Trp^+, Trp^-, Trp^- + IAA o Trp^- + ILA. **(C)** Confronto dell'espressione genica dei geni *Cyp1b1*, *Arg1* e *Il10* in TAM estratti da tumori di topi con dieta Trp^+, Trp^- o Trp^- + IAA, ottenuto tramite qRT-PCR e normalizzato su *β-actina*. * *p-value* < *0.05; ** p-value* < *0.01.*

3.6. L'espressione e l'attività di AhR è correlata con l'esito terapeutico di pazienti con PDAC umano

In ultima analisi i ricercatori hanno esaminato le correlazioni esistenti tra attività di AhR e caratteristiche prognostiche di pazienti con PDAC. È stato osservato come, anche in uomo, l'attività di AhR, sopra una certa soglia, risulti compromettente per la sopravvivenza del paziente: solamente i pazienti con attività AhR entro il primo quartile presentavano una sopravvivenza migliore (Fig. 11A). Analisi di correlazione tra l'attività di AhR ed il profilo trascrizionale dell'infiltrato tumorale hanno dimostrato infatti che l'espressione di AhR è correlata ad una ridotta attivazione dei linfociti T $CD8^+$ effettori. Inoltre, AhR è espresso maggiormente sui macrofagi, dove svolge una funzione regolatoria sul microambiente tumorale (dati non mostrati).

I ricercatori hanno anche indagato l'influenza dell'espressione di AhR sulla funzione di supporto stromale svolta dai TAM in contesto tumorale. Per fare ciò sono state allestite co-colture di macrofagi esposti a IAA con organoidi derivati da paziente PDAC. L'attivazione di AhR nei TAM tramite esposizione a IAA ha portato ad una crescita doppia del tumore rispetto alle co-colture con macrofagi di controllo, a cinque giorni dall'allestimento; inoltre, l'aggiunta di CH223191 nella coltura macrofagica prima della co-coltura ha abrogato l'effetto di IAA (Fig. 11B).

La co-coltura è stata analizzata con RNA-seq per definire le differenze di espressione genica dovute all'attivazione o meno di AhR nei macrofagi. Nelle co-colture con macrofagi esposti a IAA si è osservato un aumento dell'espressione di pathways associati alla crescita tumorale e alla metastasi, insieme ad una riduzione

di *pathways* di regolazione della proliferazione del PDAC. Dai risultati si evince come l'acquisizione di un profilo macrofagico pro-tumorale sia indotta dall'attivazione indolo-dipendente di AhR (Fig. 11C).

Anche in uomo è stato analizzato il ruolo del microbiota nella crescita del tumore PDAC, confrontando l'effetto di un trapianto di microbiota intratumorale di pazienti LTS (*long-term survivors*) e STS (*short-term survivors*) in modelli murini PDAC. Il trapianto di microbiota LTS ha mostrato una riduzione nello sviluppo tumorale, al contrario del microbiota STS. La composizione microbiotica di STS risulta infatti arricchita in specie batteriche indolo-producenti, tra cui *L. reuteri*, rispetto al microbiota di LTS, dove questa specie risultava assente. L'aumento dell'abbondanza di specie indolo-producenti, come *Bacteroides coprophilus*, *Faecalibacterium prausnitzi* ed i generi *Lactobacillus* e *Bifidobacterum*, nel TME di campioni STS correla con una prognosi peggiore ed una minore aspettativa di sopravvivenza. (Fig. 11D).

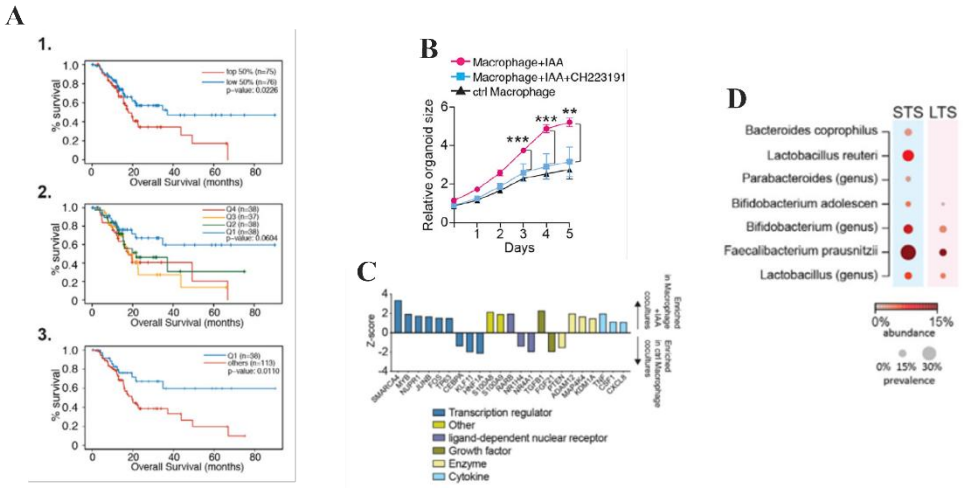

Fig. 11: L'espressione e l'attività di AhR è correlata con l'esito terapeutico di pazienti con PDAC umano. (A) Sopravvivenza complessiva di pazienti con PDAC dal dataset TCGA in base all'espressione relativa di AhR: (1) mediana d'espressione di AhR; (2) quartili d'espressione di AhR; (3) sopravvivenza del primo quartile rispetto agli altri combinati. **(B)** Curva di crescita su 5 giorni di organoidi PDAC in co-coltura con macrofagi di controllo, macrofagi + IAA e macrofagi + IAA + CH223191. **(C)** Z-score dell'arricchimento di set genici nella co-coltura di organoidi PDAC e macrofagi in presenza e meno di IAA, a 5 giorni dall'allestimento. **(D)** Prevalenza ed abbondanza relativa di specie batteriche indolo-producenti nel microbiota tumorale di pazienti PDAC STS e LTS. ** *p-value* < *0.01;* *** *p-value* < *0.001*.

3.7. Discussione e limiti allo studio

I risultati riportati in questo articolo evidenziano una forte connessione tra l'attivazione del fattore di trascrizione AhR a livello di macrofagi tumore-associati ed il profilo immunitario del microambiente tumorale in PDAC. L'attività di AhR nei TAM favorisce infatti uno *switch* antinfiammatorio nel profilo funzionale dei TAM stessi, mediante l'aumento dell'espressione di *Arg1* ed *Il10*. Inoltre, l'attività di AhR riduce la proporzione relativa di linfociti T $CD8^+$, e tra questi di $CD8^+$ effettori, nell'infiltrato, e determina un profilo immunitario meno attivato, con ridotta espressione di IFN-γ. AhR è risultato correlato anche alla crescita tumorale, in quanto gli esperimenti di inibizione della sua espressione *in vivo* hanno dimostrato lo sviluppo di una massa tumorale di minore entità nei modelli murini PDAC.

Dagli esperimenti descritti nell'articolo si evince la dipendenza dell'attività di AhR dalla produzione di indoli a livello del microbiota intestinale, dimostrando l'importanza assunta da quest'ultimo nella determinazione delle caratteristiche immunitarie del PDAC. La rimozione di specie batteriche producenti indoli o l'eliminazione del triptofano dalla dieta hanno determinato una forte riduzione nella crescita tumorale ed hanno contribuito alla definizione di un profilo immunitario pro-infiammatorio nel TME. A supporto della dipendenza di AhR dagli indoli, l'inserimento nella dieta Trp^{neg} di questi composti ha riportato i valori analizzati (massa tumorale e profilo immunitario del TME) ai livelli di controllo.

L'insieme di questi risultati contribuisce ad evidenziare l'importanza della comunicazione chimica svolta tra il microbiota ed il sistema immunitario, specificamente in alcuni contesti tumorali come PDAC. Questo forte *crosstalk* potrebbe essere indagato in profondità come target terapeutico immunostimolante in alternativa alle tecniche di trapianto di microbiota, permettendo una manipolazione a livello metabolico. Un targeting più specifico e mirato, infatti, potrebbe ridurre eventuali effetti collaterali derivati dalla massiccia modificazione del microbiota intestinale in seguito a trapianto. Tuttavia, rimane ancora incompreso come sia effettivamente il metabolismo del triptofano da parte del microbiota intestinale, e non delle cellule di mammifero, a contribuire significativamente all'attivazione di AhR.

Un altro approccio terapeutico che potrebbe essere sviluppato riguarda la modulazione dell'attività di AhR per favorire un'immunità attiva nel tumore. Bisogna tuttavia considerare che le affinità di legame dei ligandi ad AhR differiscono tra topo e uomo, rendendo più complessa la selezione di molecole specifiche con ruolo inibitorio per AhR in uomo.

4. BIBLIOGRAFIA

Hezaveh K, Shinde RS, Klötgen A et al. Tryptophan-derived microbial metabolites activate the aryl hydrocarbon receptor in tumor-associated macrophages to suppress anti-tumor immunity. *Immunity*. 2022 Feb 8;55(2):324-340.e8.

1. Riquelme E, Zhang Y, Zhang L, et al. Tumor Microbiome Diversity and Composition Influence Pancreatic Cancer Outcomes. *Cell*. 2019;178(4):795-806.e12;
2. Kamisawa T, Wood LD, Itoi T, Takaori K. Pancreatic cancer. Lancet. 2016 Jul 2;388(10039):73-85;
3. Carpenter E, Nelson S, Bednar F, Cho C, Nathan H, Sahai V, di Magliano MP, Frankel TL. Immunotherapy for pancreatic ductal adenocarcinoma. *J Surg Oncol*. 2021 Mar;123(3):751-759;
4. Li JJ, Zhu M, Kashyap PC, et al. The role of microbiome in pancreatic cancer. *Cancer Metastasis Rev*. 2021;40(3):777-789;
5. Shinde R, McGaha TL. The Aryl Hydrocarbon Receptor: Connecting Immunity to the Microenvironment. *Trends Immunol*. 2018;39(12):1005-1020;
6. Murray IA, Patterson AD, Perdew GH. Aryl hydrocarbon receptor ligands in cancer: friend and foe. *Nat Rev Cancer*. 2014;14(12):801-814;
7. Roager HM, Licht TR. Microbial tryptophan catabolites in health and disease. *Nat Commun*. 2018 Aug 17;9(1):3294;
8. D'Arcangelo E, Wu NC, Chen T, Shahaj A, Cadavid JL, Huang L, Ailles L, McGuigan AP. Gels for Live Analysis of Compartmentalized Environments (GLAnCE): A tissue model to probe tumour phenotypes at tumour-stroma interfaces. Biomaterials. 2020 Jan;228:119572
9. McKinnon KM. Flow Cytometry: An Overview. *Curr Protoc Immunol*. 2018;120:5.1.1-5.1.11. Published 2018 Feb 21
10. Tanner, S.D., Baranov, V.I., Ornatsky, O.I. *et al.* An introduction to mass cytometry: fundamentals and applications. *Cancer Immunol Immunother* 62**,** 955–965 (2013);
11. Han Y, Liu D, Li L. PD-1/PD-L1 pathway: current researches in cancer. *Am J Cancer Res*. 2020;10(3):727-742. Published 2020 Mar 1;
12. Bhat, P., Leggatt, G., Waterhouse, N. *et al.* Interferon-γ derived from cytotoxic lymphocytes directly enhances their motility and cytotoxicity. *Cell Death Dis* **8,** e2836 (2017).

Article

Immunity

Tryptophan-derived microbial metabolites activate the aryl hydrocarbon receptor in tumor-associated macrophages to suppress anti-tumor immunity

Graphical abstract

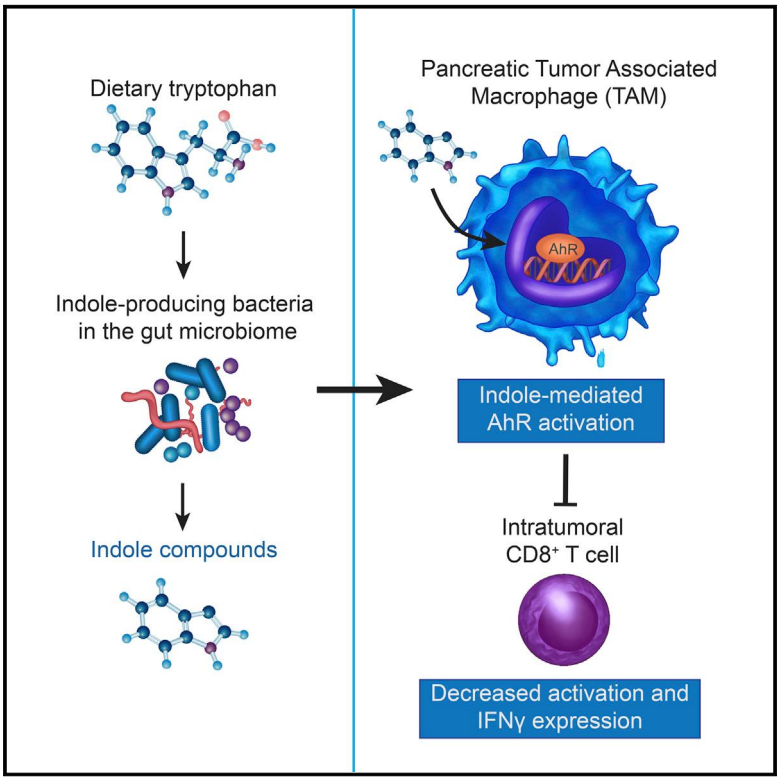

Authors

Kebria Hezaveh, Rahul S. Shinde, Andreas Klötgen, ..., Dana J. Philpott, David G. Brooks, Tracy L. McGaha

Correspondence

tmcgaha@uhnresearch.ca

In brief

AhR directs macrophage polarization. Hezaveh et al. identified a key role for AhR in tumor macrophage function in pancreatic cancer, with AhR suppressing inflammatory T cell infiltration and promoting growth. AhR was activated by gut microbiome-produced tryptophan metabolites and human disease showed association of macrophage *AHR* expression and worse outcomes.

Highlights

- AhR controls tumor-associated macrophage function in pancreatic cancer
- AhR is activated in tumor macrophages by microbiome-produced tryptophan metabolites
- Inhibition of AhR function improves T cell function, inhibiting tumor growth
- AhR expression is enriched in human tumor macrophages and correlates with survival

Hezaveh et al., 2022, Immunity *55*, 324–340
February 8, 2022
https://doi.org/10.1016/j.immuni.2022.01.006

CellPress

CellPress

Immunity

Article

Tryptophan-derived microbial metabolites activate the aryl hydrocarbon receptor in tumor-associated macrophages to suppress anti-tumor immunity

Kebria Hezaveh,[1,15,16] Rahul S. Shinde,[1,15,17] Andreas Klötgen,[2] Marie Jo Halaby,[1] Sara Lamorte,[1] M. Teresa Ciudad,[1] Rene Quevedo,[1] Luke Neufeld,[1,3] Zhe Qi Liu,[1,3] Robbie Jin,[1,3] Barbara T. Grünwald,[4] Elisabeth G. Foerster,[3] Danica Chaharlangi,[5] Mengdi Guo,[1,3] Priya Makhijani,[1,3] Xin Zhang,[1] Trevor J. Pugh,[1,6,7] Devanand M. Pinto,[8] Ileana L. Co,[9] Alison P. McGuigan,[9,10] Gun Ho Jang,[7] Rama Khokha,[4,6] Pamela S. Ohashi,[1,3] Grainne M. O'Kane,[7,11] Steven Gallinger,[7,12,13] William W. Navarre,[5] Heather Maughan,[14] Dana J. Philpott,[3] David G. Brooks,[1,3] and Tracy L. McGaha[1,3,18,*]

[1]Tumor Immunotherapy Program, Princess Margaret Cancer Centre, University Health Network, Toronto, ON M5G 2M9, Canada
[2]Department of Computational Biology of Infection Research, Helmholtz Centre for Infection Research, Braunschweig 38124, Germany
[3]Department of Immunology, The University of Toronto, Toronto, ON M5S 1A8, Canada
[4]Princess Margaret Cancer Centre, University Health Network, Toronto, ON M5G 1L7, Canada
[5]Department of Molecular Genetics, The University of Toronto, Toronto, ON M5S 1A8, Canada
[6]Department of Medical Biophysics, The University of Toronto, Toronto, ON M5G 1L7, Canada
[7]The Ontario Institute for Cancer Research, Toronto, ON M5G 0A3, Canada
[8]National Research Council, Human Health Therapeutics, Halifax, NS B3H 3Z1, Canada
[9]Institute of Biomedical Engineering, The University of Toronto, Toronto, ON M5S 3G9, Canada
[10]Department of Chemical Engineering and Applied Chemistry, The University of Toronto, Toronto, ON M5S 3E5, Canada
[11]Division of Medical Oncology, Department of Medicine, The University of Toronto, Toronto, ON M5S 3H2, Canada
[12]Department of Laboratory Medicine and Pathobiology, The University of Toronto, Toronto, ON M5S 1A8, Canada
[13]Lunenfeld-Tanenbaum Research Institute, Mount Sinai Hospital, Toronto, ON M5G 1X5, Canada
[14]Ronin Institute, Montclair, NJ 07043, USA
[15]These authors contributed equally
[16]Present address: Translational Science and Experimental Medicine, Research and Early Development, Respiratory and Immunology (R&I), BioPharmaceutical R&D, Astra Zeneca, Gothenburg, 431 50, Sweden
[17]Present address: Immunology, Microenvironment, and Metastasis Program, The Wistar Institute, Philadelphia, PA 19104, USA
[18]Lead contact
*Correspondence: tmcgaha@uhnresearch.ca
https://doi.org/10.1016/j.immuni.2022.01.006

SUMMARY

The aryl hydrocarbon receptor (AhR) is a sensor of products of tryptophan metabolism and a potent modulator of immunity. Here, we examined the impact of AhR in tumor-associated macrophage (TAM) function in pancreatic ductal adenocarcinoma (PDAC). TAMs exhibited high AhR activity and *Ahr*-deficient macrophages developed an inflammatory phenotype. Deletion of *Ahr* in myeloid cells or pharmacologic inhibition of AhR reduced PDAC growth, improved efficacy of immune checkpoint blockade, and increased intra-tumoral frequencies of IFNγ^+CD8$^+$ T cells. Macrophage tryptophan metabolism was not required for this effect. Rather, macrophage AhR activity was dependent on *Lactobacillus* metabolization of dietary tryptophan to indoles. Removal of dietary tryptophan reduced TAM AhR activity and promoted intra-tumoral accumulation of TNFα^+IFNγ^+CD8$^+$ T cells; provision of dietary indoles blocked this effect. In patients with PDAC, high *AHR* expression associated with rapid disease progression and mortality, as well as with an immune-suppressive TAM phenotype, suggesting conservation of this regulatory axis in human disease.

INTRODUCTION

Despite significant improvements in cancer therapies, outcomes for patients afflicted with pancreatic ductal adenocarcinoma (PDAC) remain grim as PDAC exhibits resistance to therapeutic approaches, including checkpoint blockade. Interestingly, microbiota appear to impact outcomes of PDAC. In long-term PDAC survivors, increased microbiome diversity correlates with survivorship and immunologic features of the tumor microenvironment (TME). Furthermore, fecal microbiota transplant (FMT) from long-term survivors reduced tumor size in mouse models, whereas FMT from short-term survivors (STS) resulted in larger tumor sizes and increases in CD4$^+$ FOXP3$^+$ T cells (Riquelme et al., 2019). Thus, the microbiota can promote or inhibit

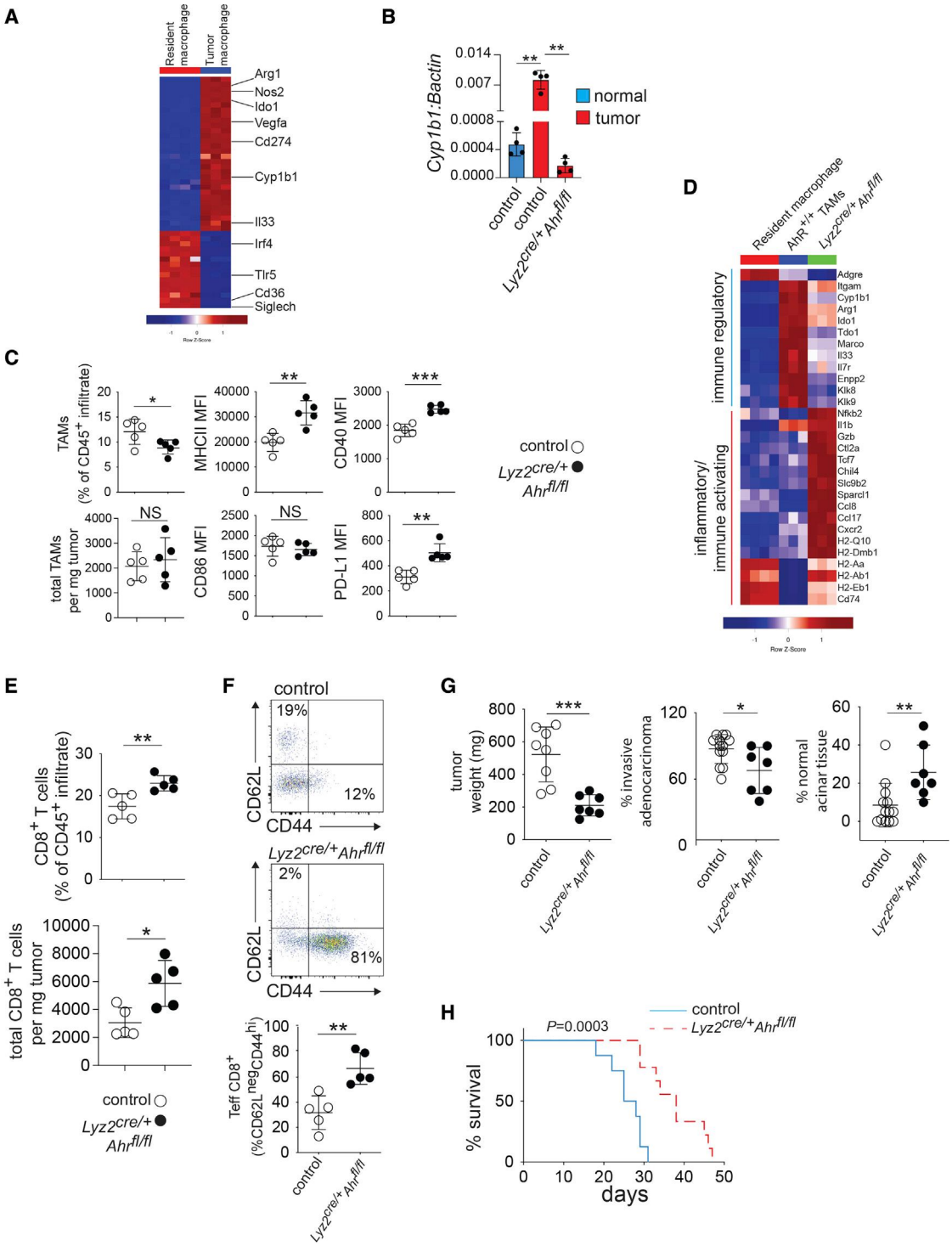

Figure 1. Deletion of AhR in macrophages drives inflammatory polarization of TAMs and CD8⁺ T cells in the PDAC TME

(A) CD45⁺CD11b⁺F4/80⁺ macrophages were enriched by flow cytometry sorting from normal pancreas (i.e., resident macrophages) or PDAC tumors 14 days after tumor implantation. Heatmap shows hierarchical clustering depicting differentially expressed RNA transcripts (>2.0 logFC, FDR p < 0.01). Each column represents an individual mouse.

(B) Macrophages were sorted from normal pancreas or tumors from mice of the indicated genotype, and mRNA expression of *Cyp1b1* relative to *βactin* was determined by qRT-PCR.

(C) Expression of surface markers in TAMs from tumor-bearing mice of the indicated genotype were determined by flow cytometry. MFI, mean fluorescence intensity.

(legend continued on next page)

tumor progression in PDAC, impacting the TME cellular composition.

An immunologically important class of bacterial metabolites is generated by metabolization of the amino acid tryptophan (Trp) to indole and related compounds (herein, collectively referred to as indoles) (Roager and Licht, 2018). Indoles are essential for mucosal barrier integrity and suppression of inflammation by activation of the transcriptional regulator AhR (Monteleone et al., 2011). Upon binding of indoles in the cytoplasm, AhR translocates to the nucleus. Ahr activation exerts potent effects on T cells, dendritic cells, and macrophages. Macrophages are a major component of the immune infiltrate in PDAC, providing stromal support for tumor growth (DeNardo and Ruffell, 2019) and resistance to chemotherapy (Halbrook et al., 2019). AhR activation can drive macrophages to acquire an immune-suppressive phenotype. AhR induces the immune-suppressive cytokine interleukin (IL)-10 (Shinde et al., 2018) and drives the expression of transforming growth factor (TGF)-α, TGF-β, and arginase (Arg1) (Franchini et al., 2019; Rothhammer et al., 2018). Importantly, AhR expression is elevated in myeloid-lineage cells relative to other cell types (Goudot et al., 2017; Shinde et al., 2018), which is suggestive of increased sensitivity to AhR ligands.

Based on these findings, we asked whether the microbiota could drive immune suppression in the PDAC TME by inducing AhR activity in tumor-associated macrophages (TAMs). To test this, we deleted *Ahr* in PDAC TAMs or inhibited AhR activity pharmacologically. Loss of AhR function caused a reduction in tumor size, and *Ahr*-deficient TAMs acquired a proinflammatory phenotype with increased intra-tumoral IFNγ$^+$ CD8$^+$ T cells. Microbial production of indole compounds was the key driver of AhR activity. In human PDAC samples, *AHR* expression was associated with rapid disease progression and mortality, as well as with an immune-suppressive TAM phenotype. Thus, microbial metabolites activate AhR in macrophages, driving macrophage polarization and PDAC outcomes.

RESULTS

Deletion of AhR drives inflammatory polarization of TAMs and CD8$^+$ T cell infiltration in the PDAC TME

To understand the role of macrophages in PDAC, we used an orthotopic model of pancreatic cancer utilizing the mT4 organoid line cloned from a primary tumor isolated from *Trp53*$^{+/LSL\text{-}R172H}$ *Kras*$^{+/LSL\text{-}G12D}$ *Pdx1*-Cre (KPC) mice (Boj et al., 2015). First, we performed RNA-seq comparing transcriptomes of intra-tumoral versus tissue-resident macrophages. Compared with tissue-resident macrophages, PDAC TAMs exhibited increased expression of 880 genes, including the pro-tumor genes *Arg1, Nos2,* and *Cd274* (the gene encoding PD-L1) (Figures 1A and S1A). Ingenuity pathway gene set enrichment analysis (iGSEA) predicted increased AhR activity in TAMs relative to the healthy tissue-resident macrophages (Figure S1B) and there was an increased expression of the AhR-responsive gene *Cyp1b1* in TAMs compared with the resident macrophages (Figures 1A and 1B). To test the prediction that macrophage AhR was required for suppression of immunity in PDAC, we deleted AhR from Mφ by crossing *Lyz2*$^{cre/+}$ x *AhR*$^{fl/fl}$ mice (*Lyz2*$^{cre/+}$*Ahr*$^{fl/fl}$) (Shinde et al., 2018). Since the *Lyz2-CRE* promoter can show activity in several myeloid cell types, we first tested the relative activity of CRE in TAMs by crossing *Lyz2*$^{cre/+}$ x Cg-Gt*(ROSA)26Sor*$^{tm9(CAG\text{-}tdTomato)Hze}$ mice (Madisen et al., 2010), examining tdTomato expression in TAMs and DCs. In the tumors, 98% of the CD11b$^+$F4/80$^+$ TAMs expressed tdTomato (Figure S1C), contrasting with intra-tumoral CD11c$^+$ DCs where 20% were tdTomato$^+$ (Figure S1C), showing *Lyz2*$^{cre/+}$ is an appropriate model to study macrophage AhR function in PDAC.

Importantly, whereas WT TAMs exhibited a 10-fold increase in expression of *Cyp1b1* compared with control macrohages, *Lyz2*$^{cre/+}$*Ahr*$^{fl/fl}$ TAMs had an abrogation of relative *Cyp1b1,* demonstrating the dependence on AhR for *Cyp1b1* expression (Figure 1B). AhR deletion reduced the percentage of TAMs in the CD45$^+$ infiltrate but did not reduce the absolute numbers of TAMs (Figure 1C). However, AhR deletion increased the expression of MHCII, CD40, and PD-L1, indicating increased TAM activation (Figure 1C). *Ahr* deletion altered the expression of 416 genes (Figures S1D and S1E). TAMs from *Lyz2*$^{cre/+}$*Ahr*$^{fl/fl}$ tumors showed a decreased immune-regulatory transcriptional signature as compared with TAMs from control tumors, characterized by reductions in the expression of *Arg1* and *Ido1* (Figure 1D). In agreement with protein expression data (Figure 1C), TAMs from *Lyz2*$^{cre/+}$*Ahr*$^{fl/fl}$ tumors were more proinflammatory with increased *Il1b*, *Gzb*, and MHCII genes expression (Figure 1D). TAMs from PDAC tumors can proliferate *in situ* and contribute to fibrosis-expressing genes for extracellular matrix (ECM) proteins (Zhu et al., 2017). When the TAMs lacked AhR, function genes involved in cell-cycle progression were decreased and the TAMs showed increased expression of pro-apoptotic genes, as well as caspases, suggesting reduced proliferation and self-renewal capability (Figure S1F). Likewise, the TAM ECM transcriptional signature was decreased in the absence of AhR (Figure S1G). Thus, the data suggest that AhR is a key driver of the TAM pro-tumor phenotype, and when AhR function is abrogated, TAM phenotypic polarization is shifted to a proinflammatory state.

Next, we sought to understand how AhR-mediated alterations in TAM polarization impact T cells in the TME. We found that the frequency and number of CD8$^+$ T cells were increased within the TME of *Lyz2*$^{cre/+}$*Ahr*$^{fl/fl}$ mice (Figure 1E). Moreover, intra-tumoral CD8$^+$ T cells from *Lyz2*$^{cre/+}$*Ahr*$^{fl/fl}$ mice exhibited a change from a naive (CD62L$^+$CD44^{lo}) to an effector/memory (CD62L^{neg}CD44^{hi}) phenotype (Figure 1F), suggesting increased T cell activation. Moreover, tumor weight and the extent of invasive

(D) Heatmaps showing differential expression (FDR, <0.01; logFC, >1) of selected inflammatory or immune-regulatory markers in FACS-sorted TAMs and healthy tissue macrophages as described in (A and B).
(E) Intra-tumoral CD3$^+$CD8$^+$ T cell numbers as a percent of the CD45$^+$ immune infiltrate were determined by flow cytometry in d14 tumors in *Lyz2*$^{cre/+}$*Ahr*$^{fl/fl}$ versus control tumor-bearing mice.
(F) Percent of CD44- and CD62L-positive intra-tumoral CD8$^+$ T cells from samples described in (E) was determined by flow cytometry.
(G) Day-14 tumor weight and pathology in mice of the indicated genotype.
(H) Survival curves for tumor-bearing mice of the indicated genotype. n = 8 mice per group. (see also Figure S1). * p <.05, ** p <.01, *** p <.001.

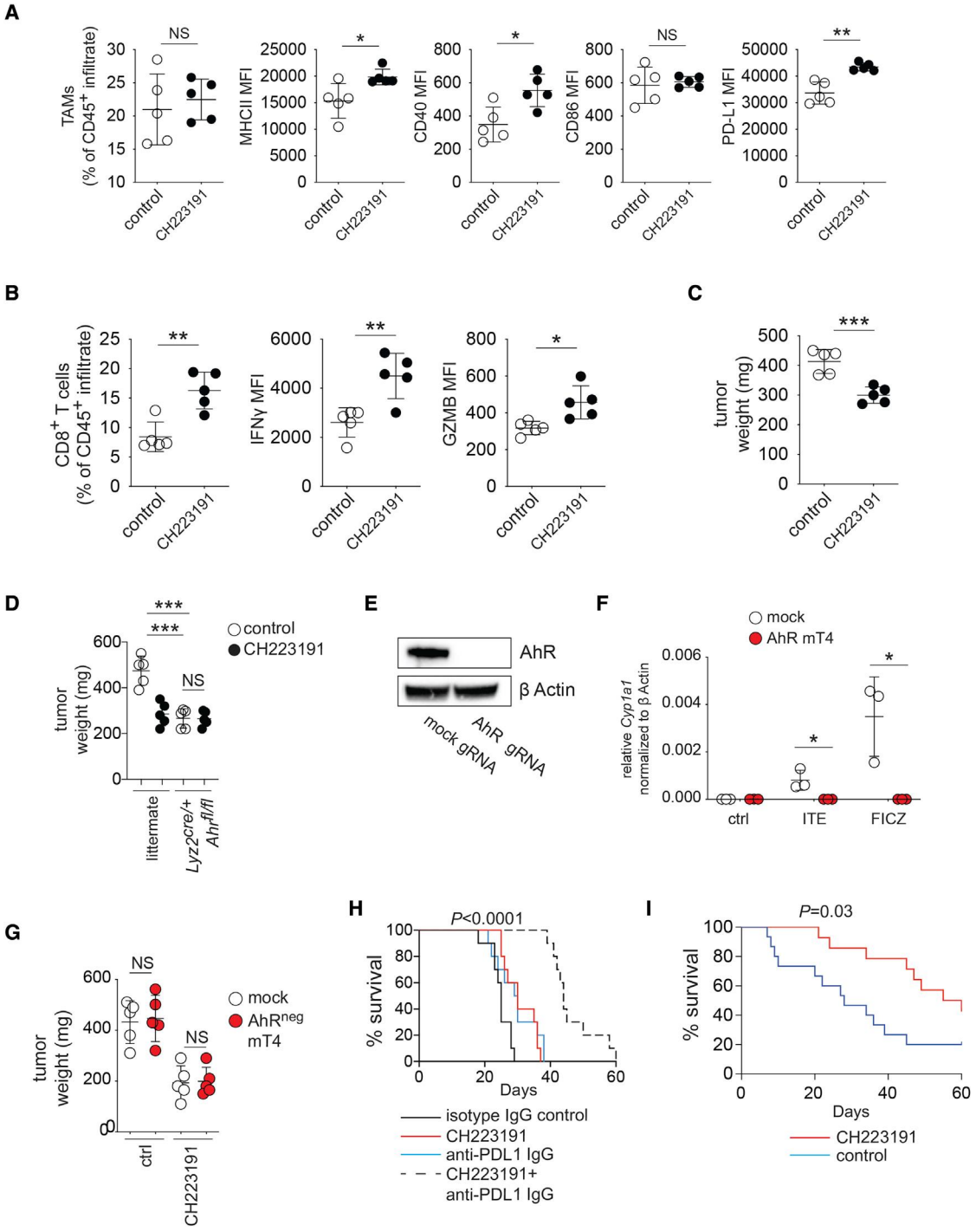

Figure 2. Pharmacologic inhibition of AhR promotes inflammation in the TME and improves responses to immune therapy

(A) CD45$^+$CD11b$^+$F4/80$^+$ TAMs were analyzed by flow cytometry in d14 tumors from B6 mice +/− treatment with the AhR inhibitor CH223191 as described in STAR Methods. MFI, mean fluorescence intensity.

(B) Tumor infiltrating CD3$^+$CD8$^+$ T cells were analyzed from mice described in (A) by flow cytometry. GZMB-granzyme B.

(C) Tumor weight of d14 tumors from mice described in (A).

(D) D14 tumor weight from mice of the indicated genotype +/− CH223191 treatment as described in (A).

(E) Representative Western blot showing loss of AhR expression in mT4 cell clone transfected with control versus AhR guide RNA.

(F) *Cyp1a1* quantification by qRT-PCR of control and mT4 cultures treated with the AhR agonists ITE and FICZ.

(legend continued on next page)

adenocarcinoma were decreased in *Lyz2*$^{cre/+}$*Ahr*$^{fl/fl}$ mice (Figure 1G), leading to improved survival compared with littermate controls (Figure 1H). Further, we observed decreased tumor burden in *Lyz2*$^{cre/+}$*Ahr*$^{fl/fl}$ mice which bear tumors from several other KPC-derived tumor cell lines (Figure S1H), indicating that lack of AhR in TAMs reduces tumor burden across multiple PDAC tumor models.

Pharmacologic inhibition of AhR promotes inflammation in the TME and improves responses to therapy

To test whether pharmacologic inhibition of AhR could impact the immune infiltrate phenotype and tumor growth, we treated mice with the AhR inhibitor CH223191 (Shinde et al., 2018). TAMs from tumor-bearing mice receiving CH223191 had increased expression of MHCII, CD40, and PD-L1, increases in IFNγ and granzyme B-expressing CD8$^+$ T cells, and enhanced tumor control (Figures 2A–2C). Since CH223191 inhibits AhR activity in all cell types, we tested the contribution of macrophage AhR function to these results by repeating AhR inhibition experiments using *Lyz2*$^{cre/+}$*Ahr*$^{fl/fl}$ mice. On day 14, tumors had a 50% reduction in weight when the mice received CH223191 in the littermate control groups. In contrast, the addition of CH223191 did not have any additional effect on tumor control in *Lyz2*$^{cre/+}$*Ahr*$^{fl/fl}$ mice (Figure 2D), indicating that the effect of the drug is through targeting of AhR in macrophages. AhR has been reported to directly affect tumor cell growth (Murray et al., 2014); therefore, we tested the impact of AhR deletion in PDAC cells on tumor growth. Deletion of AhR in tumor cells by CRISPR (Figure 2E) nullified PDAC cell responses to AhR agonists *in vitro* (Figure 2F); however, there was no effect on tumor growth *in vivo* compared with mock PDAC tumors (Figure 2G). These data suggest that macrophage-specific AhR function is the main contributor to AhR-dependent tumor growth.

Since PD-L1 was increased in TAMs from both *Lyz2*$^{cre/+}$*Ahr*$^{fl/fl}$ (Figure 1C) and CH223191-treated mice (Figure 2B), we tested for a potential effect of dual AhR and PD-L1 blockade. Control mice (isotype IgG-treated) had a median survival of 25 days (Figure 2H). Administration of either αPD-L1 IgG or AhR inhibitor alone increased survival; however, combining αPD-L1 IgG and AhR inhibition had the strongest effect by extending the survival 2-fold compared with the control treatment and by increasing the survival up to 50% higher than either therapy alone (Figure 2H). We then tested the effect of AhR inhibition on autochthonous PDAC tumors using a tamoxifen inducible KPC (iKPC) model of PDAC (Maddipati and Stanger, 2015). Median survival for the control group was 28 days post-initiation of treatment (Figure 2I). In contrast, mice treated with AhR inhibitor had improved survival (Figure 2I), suggesting AhR inhibition can improve outcomes for both *in situ* pancreatic adenocarcinoma, as well as orthotopic tumors. Hence, the data show that AhR is a central driver of TAM function, and suppression of inflammatory T cell maturation, and its inhibition improves responses to immune checkpoint blockade.

Macrophage AhR activity shapes the transcriptional landscape in PDAC

To understand the impact of macrophage AhR function on the TME, we conducted CyTOF and single-cell RNA sequence (scRNA-seq) analysis of day-14 tumors (Halaby et al., 2019; Levine et al., 2015). We identified 32 clusters of intra-tumoral immune cells by CyTOF, with the majority being myeloid or granulocytic (Figures 3A and S2A). There were 3 macrophage clusters identified by the expression of F4/80 (clusters 12, 13, and 22). Macrophage cluster 22 expressed the immune-regulatory polarization markers CD206 and PD-L1, as well as the inflammatory monocyte marker Ly6C, suggesting monocytic origin (Figures 3B and S2A). In contrast, macrophage clusters 12 and 13 were Ly6C^{neg,} with macrophage cluster 12 expressing PD-L1, MHCII, and Ly6G compared with cluster 13, which had the lowest staining of all three markers (Figures 3B and S2A). Furthermore, we identified 2 populations of CD11c$^+$ dendritic cells (DCs, clusters 14 and 16) differentiated by the expression of PD-L1 (in cluster 14) and the integrin CD103 (in cluster 16) (Figure S2A). In addition, DC cluster 14 had expression of several markers found in the macrophage clusters, including CD11b, CD44, and Nos2 (iNOS). CD8$^+$ T cells appeared as 5 related clusters (clusters 11, 15, 17, 18, and 28) differentiated by the expression of T bet, a key transcription factor driving inflammatory Th1 T cell lineage commitment (Szabo et al., 2000) and CX3CR1, a marker of inflammatory intra-tumoral T cells (Yamauchi et al., 2020) (Figure S2A). Deletion of TAM *Ahr* did not impact cell clustering or the relative composition of the immune infiltrate (Figures 2B and S2C); however, loss of *Ahr* reduced iNOS, CCL4, and TNFα detectable by CyTOF in all macrophage clusters (clusters 12, 13, and 22), suggesting alteration in functional activity (Figure 3C).

To understand the transcriptomic changes in the TME caused by loss of macrophage *Ahr*, we performed scRNA-seq analysis of 10,000 cells from *Lyz2*$^{cre/+}$*Ahr*$^{fl/fl}$ and control tumors. We identified 18 clusters of cells in the tumor, including multiple clusters of macrophages, T cells, and granulocytes (Figures 3D and S2D). Similar to the CyTOF results, we identified 3 clusters of macrophages (Figure 3D). Macrophage cluster 1 expressed *Arg1* and *Tgm2* (a gene involved in macrophage remodeling of ECM in tumors) (Afik et al., 2016), whereas macrophage clusters 2 and 3 expressed *Klf4* encoding the transcription factor Krüppel-like factor 4, a driver of regulatory macrophage function in the TME (Liao et al., 2011) (Figure S2E). Further distinguishing between macrophage cluster 2 and 3, cluster 2 expressed the immune-suppressive macrophage marker *Chil3/Ym1* (Zhu et al., 2020), whereas there was an enrichment in cluster 3 of mRNA for *Il1b* and *Ptgs2* (the gene encoding prostaglandin-endoperoxide synthase 2) (Figure S2E). Thus, cumulatively, the data show that the macrophage populations in the PDAC TME exhibit a transcriptional profile with characteristics of pro-tumor, alternative polarization states.

Macrophage clusters 1 and 2 showed a significant transcriptional change in *Lyz2*$^{cre/+}$*Ahr*$^{fl/fl}$ tumors. iGSEA analysis showed

(G) B6 mice were orthotopically implanted with the indicated mT4 clones +/− CH223191 beginning 4 days after implantation. Weights are shown for d14 tumors.
(H) Survival curves of mice treated with AhR antagonist, anti-PD-L1 blockade, or a combination of the two versus controls. n = 10 mice per group.
(I) Survival curves of iKPC mice treated with AhR antagonist versus controls 12 weeks post-tamoxifen treatment. n = 14 mice per group. * p <.05, ** p <.01, ***, NS-not significant.

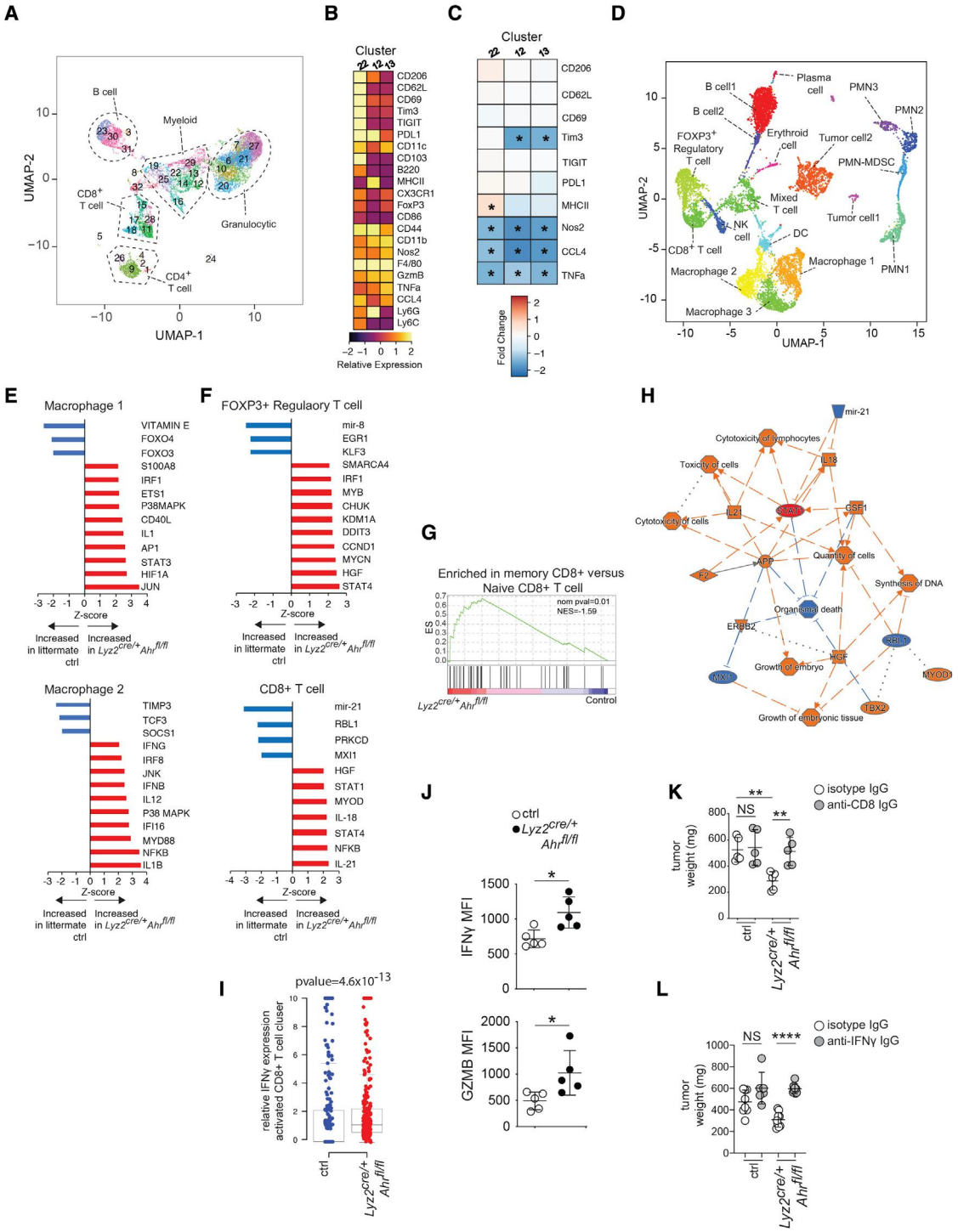

Figure 3. Macrophage AhR activity shapes the immune transcriptional landscape in PDAC

(A) UMAP and phenograph analysis of the CD45$^+$ infiltrate in d14 PDAC tumors showing the major immune subpopulations identified by CyTOF analysis. Data from 4 (control) or 5 ($Lyz2^{cre/+}Ahr^{fl/fl}$) biological replicates were concatenated in the plots.

(B) Heatmap depicting relative expression of the indicated markers in d14 tumors of $Lyz2^{cre/+}Ahr^{fl/fl}$-tumor-bearing mice versus controls for the 3 F4/80$^+$ macrophage clusters (Cluster 12, 13, and 22).

(C) Heatmap showing relative expression of indicated markers in each TAM cluster in $Lyz2^{cre/+}Ahr^{fl/f}$ versus control determined by CyTOF. Red squares indicate increased expression compared with control baseline, whereas blue squares indicate decreased expression relative to control baseline.

(D) UMAP showing scRNA-seq data of pooled whole day-14 tumor samples for both $Lyz2^{cre/+}Ahr^{fl/fl}$ and control tumors. n = 3 mice per group. PMN- polymorphonuclear leukocyte.

(legend continued on next page)

that in *Lyz2*$^{cre/+}$*Ahr*$^{fl/fl}$ tumors, macrophage cluster 1 was enriched for expression of target genes for several interferon-induced transcription factors (Jun/Ap1, STAT3, and IRF1), signal transduction networks, and inflammatory mediators, with reduction of genes driven by the immune-regulatory transcription factors Foxo3 (Dejean et al., 2009) and Foxo4 (Zhu et al., 2015) (Figure 3E). iGESA analysis of macrophage cluster 2 showed an even stronger enrichment of interferon response pathways in *Lyz2*-$^{cre/+}$*Ahr*$^{fl/fl}$ tumors, including IFNγ, IRF8, IFI16, IFNβ, and the MYD88 pathway (Figure 3E). Surprisingly, iGSEA analysis of cluster 3 showed that loss of AhR had relatively little impact with no enrichment of genes associated with inflammation or interferon responses (Figure S2F), suggesting a differential effect of AhR deletion on TAM populations in the PDAC TME.

There were 3 T cell clusters identified in the TME, including a FOXP3$^+$ T reg cell cluster, a mixed population of CD4$^+$ and CD8$^+$ T cells, and a population of Tc1-like CD8$^+$ T cells (St Paul and Ohashi, 2020) with expression of *Ifng* (Figure S2D). The CD8$^+$ T cell cluster also showed expression of the exhaustion marker *Lag3* (Figure S2D); however, expression of other T cell exhaustion markers (e.g., PD1, TIM3, and CTLA4) were low, suggesting that the population was not functionally exhausted per se. Transcriptomic analysis of the FOXP3$^+$ T reg cell cluster showed that loss of *Ahr* in macrophages caused enrichment for a number of pathways associated with plasticity and loss of T reg cell suppressive function, including STAT4 (Cuadrado et al., 2018) and IRF1 (Fragale et al., 2008) (Figure 3F). In addition, there was enrichment of several pathways involved in T reg cell homeostasis in the FOXP3$^+$ T reg cell cluster in *Lyz2*$^{cre/+}$*Ahr*$^{fl/fl}$ tumors, including CHUK/IKKA and MYB (Chen et al., 2015; Dias et al., 2017), as well as the stress response/apoptosis pathway driven by DDIT3/CHOP (Figure 3F). Together, these results suggest that the loss of Mφ AhR may promote a switch to an inflammatory phenotype in FOXP3+ T reg cells with increased cellular stress and population turnover.

We also observed inflammatory transcriptional changes in the CD8$^+$ T cell cluster in *Lyz2*$^{cre/+}$*Ahr*$^{fl/fl}$ tumors compared with controls. There was enrichment of IFN responsive pathways (e.g., STAT1, STAT4, NFKB, and IL-12) in the CD8$^+$ T cell cluster (Figure 3F). This showed that the intra-tumoral CD8$^+$ T cells were responding to the increased inflammatory milieu in the TME of *Lyz2*$^{cre/+}$*Ahr*$^{fl/fl}$ tumors with heightened functional maturation. Supporting this prediction, GSEA analysis of the differentially expressed genes from the CD8$^+$ T cell clusters identified enrichment of upregulated genes characteristic of memory CD8$^+$ T cells (Figure 3G), suggesting a potentially key role for this population for the reduced tumor burden seen in macrophage *Ahr*-deficient tumors.

Network analysis of the transcriptional signatures impacted in the CD8$^+$ T cell cluster from *Lyz2*$^{cre/+}$*Ahr*$^{fl/fl}$ tumors identified a key role for STAT1 in the observed global transcriptional pathway alterations (Figure 3H). Since STAT1 is a driver of IFNγ signaling, we predicted that increased IFNγ may be a significant contributor to inflammation and CD8$^+$ T cell activation in the intra-tumoral milieu of *Lyz2*$^{cre/+}$*Ahr*$^{fl/fl}$ tumors. In agreement with this, the CD8$^+$ T cell cluster showed increased *Ifng* expression when macrophage AhR was deleted compared with controls (Figure 3I). This was confirmed at the protein level by flow cytometry where we observed increased IFN-γ in CD8$^+$ T cells from *Lyz2*$^{cre/+}$*Ahr*$^{fl/fl}$ tumors compared with control tumors (Figure 3J). Because IFNγ is a driver of anti-tumor immunity (Braumüller et al., 2013) (Shankaran et al., 2001), we tested the impact of IFNγ on tumor growth in PDAC. Depletion of CD8$^+$ T cells abrogated the effect of macrophage *Ahr* deletion on tumor size, showing that CD8$^+$ T cells are needed for control of tumor growth (Figure 3K). We found that antibody blockade of IFNγ did not impact tumor size in controls (Figure 3L); however, IFNγ blockade in *Lyz2*$^{cre/+}$*Ahr*$^{fl/fl}$ tumor-bearing mice rescued tumor growth to control levels, showing that increased IFNγ production by CD8$^+$ T cells is an important driver of the reduced tumor burden observed in *Lyz2*$^{cre/+}$*Ahr*$^{fl/fl}$ tumors (Figure 3L).

Indole-producing microbiota drive suppression in the TME promoting tumor growth

Next, we investigated sources of ligands that may drive AhR activity in the TME. Because AhR is a receptor for ligands generated by mammalian and bacterial metabolization of the amino acid Trp (Shinde and McGaha, 2018), we focused on these pathways. Trp is metabolized to the AhR ligand kynurenine by the enzyme indoleamine 2,3 dioxygenase 1 (IDO1) (Shinde and McGaha, 2018); however, neither the inhibition of IDO1 by treatment of tumor-bearing mice with 1-methyl tryptophan (1MT) (Ravishankar et al., 2015) nor the deletion of *Ido1* impacted tumor growth (Figures 4A and S3A) or AhR activity in TAMs (Figure S3B). In contrast, administration of broad-spectrum antibiotics reduced tumor size (Figure 4A). Bacteria belonging to the genus *Lactobacillus* are gut commensals with an ability to produce indoles from Trp metabolization (Roager and Licht, 2018). *Lactobacilli,* with a sensitivity to the antibiotic ampicillin (Amp) and resistance to vancomycin (Vanc), are important drivers of AhR activity in myeloid cells in inflammatory disease (Rothhammer et al., 2016). We hypothesized that removal of *Lactobacilli* by administration of Amp would phenocopy observations in

(E) iGSEA analysis of the macrophage clusters 1 and 2 for enrichment of genes associated with the indicated pathways.
(F) iGSEA analysis of the clusters FOXP3+ regulatory T cell and CD8$^+$ T cell for enrichment of genes associated with the indicated pathways.
(G) GSEA plot of CD8$^+$ T cell cluster for enrichment of genes associated with memory CD8$^+$ T cell differentiation was done with MSigDB (C7) ES = enrichment score.
(H) Summary network analysis of scRNA-seq data for the activated CD8$^+$ T cell cluster showing the interactions between upstream regulators, downstream genes, and physiological functions of activated CD8$^+$ T cells. Red symbols/lines indicate activation, whereas blue ones indicate inhibition.
(I) Relative IFNγ single-cell gene expression in the activated CD8$^+$ T cells cluster.
(J) Mean fluorescence intensity of IFNγ (left) and granzyme B (right) in *Lyz2*$^{cre/+}$*Ahr*$^{fl/fl}$ and control CD8$^+$ T cells from day-14 tumors as determined by flow cytometry.
(K and L) Effect of CD8$^+$ T cell depletion (K) or IFNγ blockade (L) on PDAC tumor weight in *Lyz2*$^{cre/+}$*Ahr*$^{fl/fl}$ and control tumor-bearing mice. Tumors were collected at day 14. (see also Figure S2). * p <.05, ** p <.01, **** p <.0001, NS- not significant.

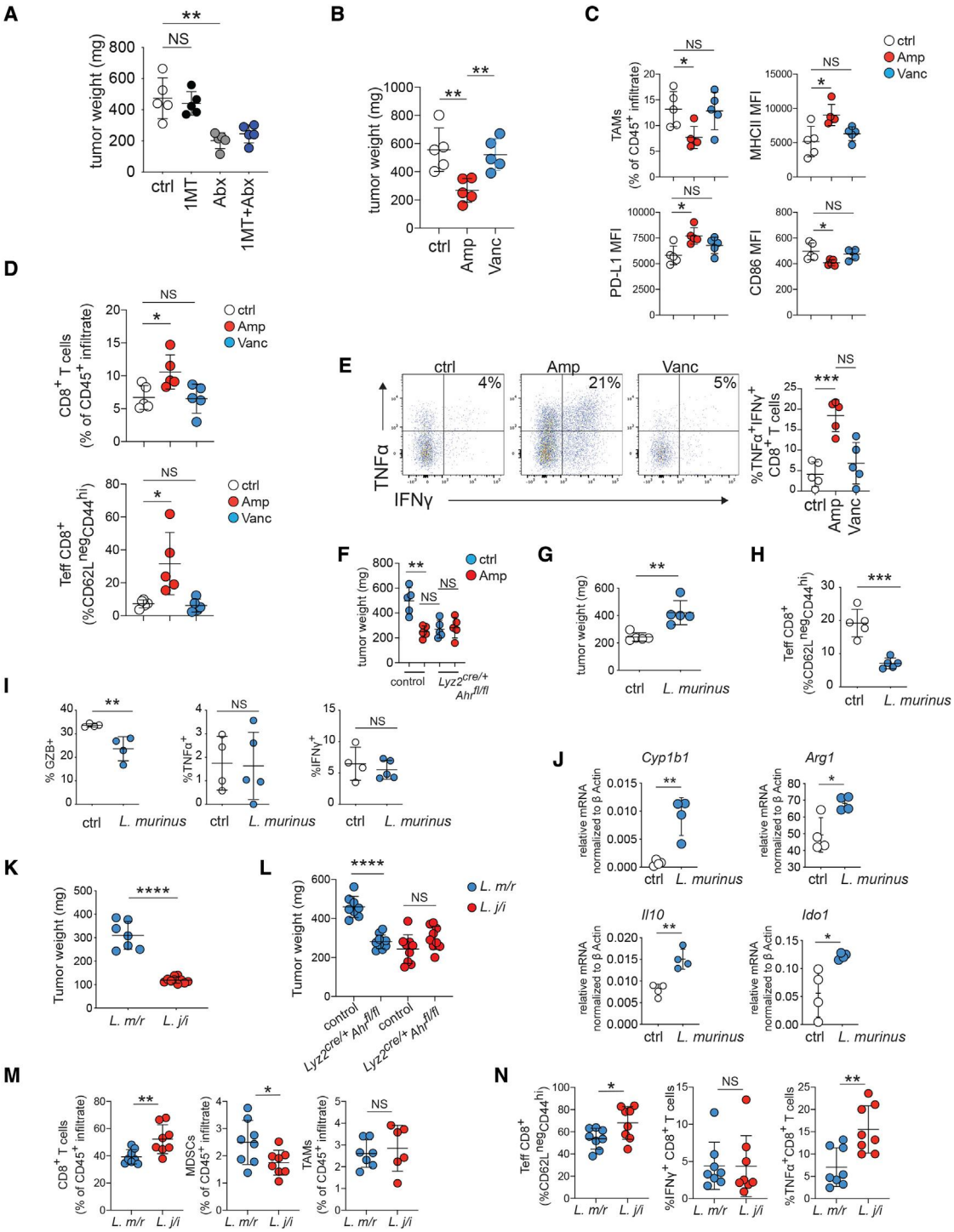

Figure 4. Indole-producing microbiota drive immune suppression in the TME

(A) B6 pancreatic tumor-bearing mice were treated with D1MT or broad-spectrum antibiotics. Tumor weight was determined 14 days after implantation.

(B) Tumor-bearing B6 mice were placed on drinking water containing the indicated antibiotic as described in STAR Methods. Tumor weight was determined 14 days after implantation.

(C) $CD45^+CD11b^+F4/80^+$ TAMs from the tumors in (B) were analyzed for the indicated markers by flow cytometry.

(D) $CD3^+CD8^+$ T cells from the tumors in (B) were analyzed for the indicated markers by flow cytometry.

(E) Percentage of tumor infiltrating $CD3^+CD8^+$ T cells, expressing IFNγ and TNFα from the tumors in (B) was determined by flow cytometry. Plots to the left are representative pseudocolor dot plots from each group gated on $CD3^+CD8^+$ T cells.

(legend continued on next page)

Lyz2$^{cre/+}$*Ahr*$^{fl/fl}$ mice. In agreement with this prediction, Amp treatment, but not Vanc, reduced tumor weight. Moreover, the TAMs in Amp-treated mice showed increased expression of MHCII and PD-L1 (Figure 4C) and reduced expression of AhR-responsive genes (*Cyp1a1, Cyp1b1*, and *Cyp1a2*) (Figure S3C), indicating that Amp exposure reduces TAM AhR transcriptional activity. Furthermore, Amp treatment increased infiltration of activated CD8$^+$ T cells (Figure 4D). Importantly, intra-tumoral IFNγ^+TNFα^+CD8$^+$ T cells increased 5-fold in Amp-treated mice compared with Vanc-treated groups (Figure 4E). AhR function was required for this effect as Amp treatment had no effect on tumor size in *Lyz2*$^{cre/+}$*Ahr*$^{fl/fl}$ mice (Figure 4F). These data suggest that Amp-sensitive microbes may promote tumor growth and immune suppression in PDAC.

When we analyzed the gut microbiome of antibiotic-treated, tumor-bearing mice by 16S ribosomal sequencing, we found that that Amp treatment increased fecal microbial alpha-diversity and operational taxonomic units compared with controls (Figure S3D), while reducing the relative abundance of *Lactobacillus* (Figure S3E). *Lactobacillus* made up 10% of the total bacteria taxa detected in control microbiome, dropping to 3.7% in Amp-treated mice (Figure S4A). This contrasted with Vanc treatment, which reduced overall microbial diversity but increased the relative *Lactobacillus* abundance (Figures S3E and S4A). Analysis of the *Lactobacillus* species present in the fecal microbiome indicated that the most abundant species was *Lactobacillus murinus*, which constituted approximately 50% of the total *Lactobacillus* detected overall in controls and the large majority of *Lactobacillus* detected in Vanc-treated mice (Figure S4A). *L. murinus* can reduce inflammation in the central nervous system via indole production (Wilck et al., 2017), suggesting a potential link between antibiotic treatment, the modulation of *L. murinus* in the fecal microbiome, and intra-tumoral immune modulation

Next, we compared 4 *Lactobacillus* species cultured from the gastrointestinal tract (GIT) of C57BL/6J mice for the ability to produce indoles by mass spectrometry analysis. Reports indicate that *L. johnsonii* possesses limited ability to produce the AhR ligand indole-3-aldehyde (IAld), whereas *L. reuteri* and *L. murinus* can both produce anti-inflammatory indoles (Wilck et al., 2017; Zelante et al., 2013). In agreement with this, we found that neither *L. johnsonni* nor *L. intestinalis* produced IAld or another AhR ligand indole lactic acid (ILA) (Figures S4B and S4C). In contrast, ILA and IAld were produced by both *L. reuteri* and *L. murinus* cultures, with *L. murinus* showing higher relative production of both the metabolites compared with *L. reuteri* (Figures S4B and S4C). An examination of indoles and amino acids or their derivatives present in the *Lactobacillus* cultures showed that *L. murinus* and *L. reuteri* cultures had similar profiles that were compositionally distinct from *L. intestinalis* and *L. johnsonii* (Figures S4C and S4D). Since *L. murinus* can suppress inflammation via production of indoles (Wilck et al., 2017), we then tested whether this microbe could impact tumor growth and inflammation in PDAC. For this, we gavaged germ-free mice with *L. murinus* prior to implantation of PDAC tumors, examining growth and immune characteristics. Transplanted *L. murinus* was stable, and we could detect it in the feces 30 days after gavage (Figure S4E). Importantly, mice gavaged with *L. murinus* had increased fecal ILA (Figure S4F). Tumors in mice with *L. murinus* were larger than tumors in control germ-free mice (Figure 4G), suggesting *L. murinus* promoted PDAC tumor growth. Compared with the control group, mice with *L. murinus* microbiota had decreased numbers of activated and granzyme B-expressing CD8$^+$ T cells, although there was no change in TNFα and IFNγ expression (Figures 4H and 4I). TAMs sorted from 14 day tumors showed that the presence of a *L. murinus* microbiome increased the expression of *Cyp1b1* compared with controls, demonstrating that *L. murinus* microbiota correlate with increased AhR activity (Figure 4J). Moreover, the TAMs exhibited increases in A expression of the pro-tumor genes *Arg1*, *Ido1*, and *Il10* (Figure 4J), suggesting that *L. murinus* could drive TAMs to acquire an immunosuppressive program.

However, these results did not rule out a general role for microbiota in the suppression of immunity in the TME rather than a specific effect of *L. murinus*. Thus, we utilized a microbiota transplant approach, directly comparing tumor growth in mice with a microbiome containing indole-producing bacteria (i.e., *L. murinus* and *L. reuteri*, hereafter referred to as *L. m/r*) to mice with a microbiome containing *Lactobacillus* that do not robustly produce indoles (i.e., *L. johnsonii* and *L. intestinalis*, hereafter referred to as *L. j/l*). Similar to germ-free mice, the *L. m/r* group had increased fecal ILA compared with the *L. j/i* group (Figure S4G). Strikingly, there was a large difference in tumor weight between the groups at day 14 (Figure 4K), suggesting that the presence of indole-producing bacteria in the GIT contributes to tumor growth. To test the prediction that the increased tumor burden in the *L. m/r* group was due to indole-induced TAM AhR activity, we repeated the experiment using *Lyz2*$^{cre/+}$*Ahr*$^{fl/fl}$ mice. We found that *Lyz2*$^{cre/+}$*Ahr*$^{fl/fl}$ mice with

(F) Tumor-bearing B6 mice of the indicated genotype were placed on drinking water containing ampicillin (Amp) as described in (B) and tumor weight was determined 14 days after implantation.

(G) Day-14 tumor weight in germ-free mice with a *L. murinus* microbiome compared with controls.

(H and I) Total effector CD8$^+$ T cells (CD62L^{lo}CD44^{hi}) as a percentage of the CD45$^+$ infiltrate (H) and the percentage of CD3$^+$CD8$^+$ T cells expressing granzyme B (GZB), TNFα, and IFNγ (I) was determined by flow cytometry in day-14 tumors in inoculated versus control germ-free tumor-bearing mice.

(J) CD45$^+$CD11b$^+$F4/80$^+$ TAMs were sorted from day-14 tumors from germ-free B6 mice +/−, an *L. murinus* microbiome. The mRNA indicated were measured by q-rtPCR and normalized against *Bactin* as described in STAR Methods.

(K and L) Day-14 tumor weight from B6 mice (J) or *Lyz2*$^{cre/+}$*Ahr*$^{fl/fl}$ mice or littermate controls (L) with a microbiome containing *L. murinus*+*L. reuteri* (*L. m/r*) or *L. johnsonii*+*L. intestinalis* (*L. j/i*).

(M) Percent of intra-tumoral CD8$^+$ T cells, CD11b$^+$GR1$^+$MHCII^{lo} MDSCs, and CD11b$^+$F4/80$^+$ TAMs in the CD45$^+$ infiltrate of tumors from (J) was determined by flow cytometry.

(N) Percentage of Teff, IFNγ^+, and TFNα^+ CD8$^+$ T cells from tumors described in (J) was determined by flow cytometry. (see also Figure S3). * p <.05, ** p <.01, *** p <.001, **** p <.0001, NS- not significant.

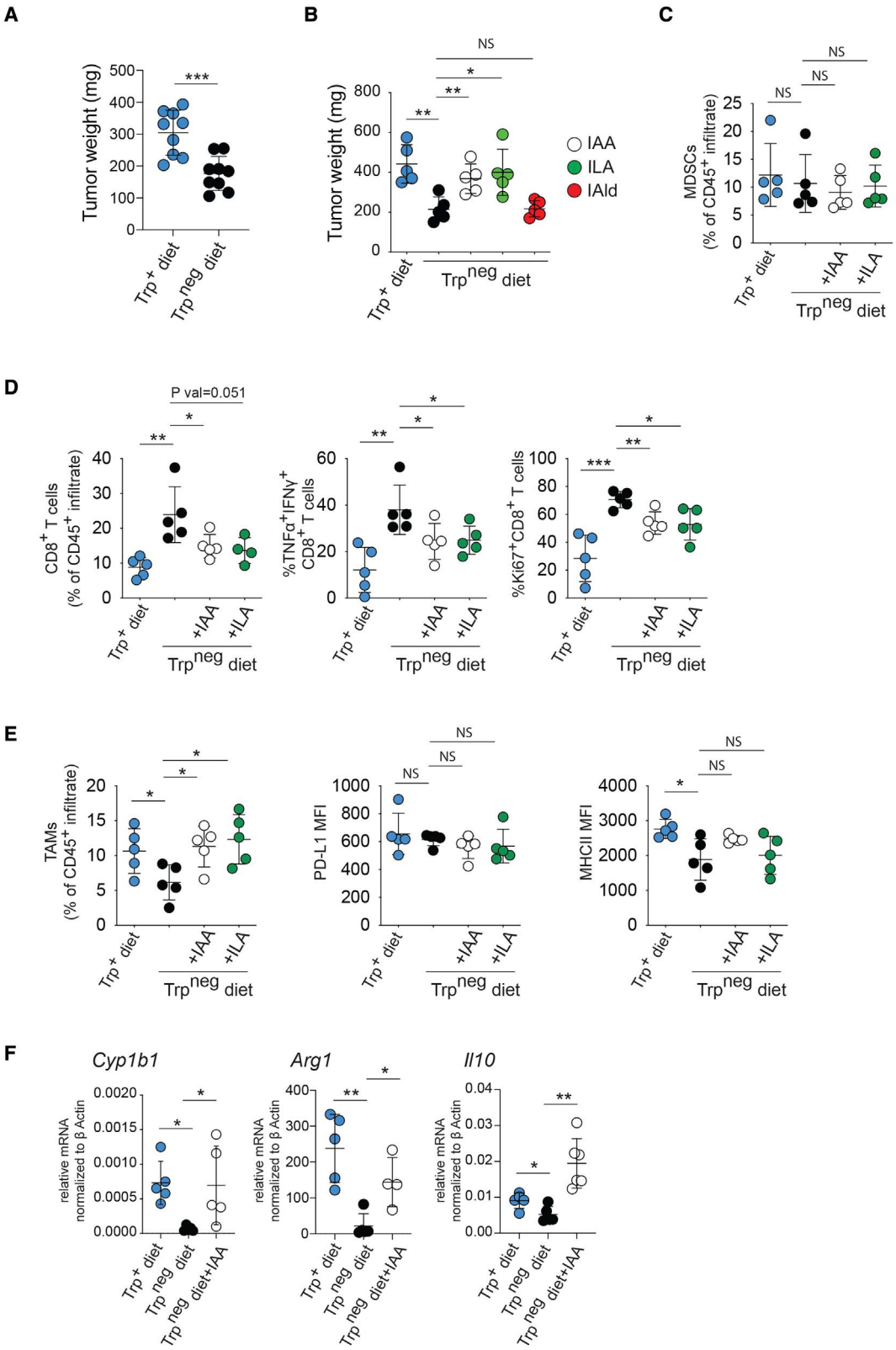

Figure 5. Dietary Trp and indoles promote immune suppression and PDAC growth

(A) Day-14 PDAC tumor weight in mice on control or Trp-free diet.

(B) Day-14 tumor size in B6 mice on chow +/− Trp with some groups receiving daily gavage with the indicated indole.

(legend continued on next page)

an *L. m/r* microbiome had reduced tumor weight compared with *L. m/r* littermate controls (Figure 4L). In contrast, the loss of TAM AhR function had no impact on tumor size in *L. j/l* mice (Figure 4L), suggesting that the increased tumor weight in *L. m/r* mice is due to TAM AhR activity. The difference in tumor weight was accompanied with alteration of the TME. There was an increase in intra-tumoral $CD8^+$ T cells and a reduction in myeloid derived suppressor cells (MDSCs) in the tumors from the *L. j/l* group compared with tumors from the *L. m/r* group (Figure 4M). The percentages of effector $CD8^+$ T cells were significantly increased in the tumors of *L. j/i* mice compared with tumors from the *L. m/r* group, which paralleled an increase in $TNF\alpha^{+-}$ $CD8^+$ T cells (Figure 4N). Combined with the germ-free experiments, the data show that indole-producing bacteria increase AhR transcriptional responses and promote an immunosuppressive TME in PDAC.

Trp and the indoles IAA and ILA in the diet promote immune suppression and pancreatic tumor growth

Since Trp metabolization is a key mechanism of AhR ligand generation (Shinde and McGaha, 2018), we tested whether the removal of dietary Trp would phenocopy effects of *Ahr* deletion in macrophages. Removal of Trp from the diet was well tolerated over the course of the experiment; however, at day 10, tumors were 2-fold smaller in the dietary Trp^{neg} group compared with controls (Figure 5A). We then reasoned that if the reduction of PDAC burden in mice in a Trp^{neg} diet was due to reduced indole production by the microbiome, we should be able to rescue tumor growth by provision of dietary indoles. To test this, we gavaged dietary Trp^{neg} mice with indoles (indole-3-acetic acid [IAA], ILA, or IAld) after tumor implantation. In agreement with our hypothesis, both IAA and ILA supplementation abrogated the effect of a Trp^{neg} diet, resulting in tumor weight that was comparable with that of the dietary Trp+ controls (Figure 5B). Further examination of the TME by flow cytometry showed that removal of Trp from the diet did not impact the percentage of MDSCs (Figure 5C); however, lack of dietary Trp increased the number of $TNF\alpha^+IFN\gamma^+$ and proliferating $CD8^+$ T cells, an effect that was reversed by dietary IAA or ILA (Figure 5D). In the dietary Trp^{neg} group, TAMs decreased as a percentage of the immune infiltrate and showed decreased expression of MHCII compared with controls, suggesting a less activated phenotype (Figure 5E). Supplementation of the diet with IAA or ILA rescued this effect increasing the percentage of TAMs and MHCII expression to levels comparable with that of the Trp^+ diet controls (Figure 5E). Moreover, in the absence of dietary Trp, TAMs had decreased expression of *Il10* and *Arg1* and *Cyp1b1* (Figure 5F). Importantly, IAA supplementation in dietary Trp^{neg} mice increased *Il10*, *Arg1*, *Cyp1a1*, and *Cyp1a2* expression, suggesting that IAA activates AhR and drives an immunosuppressive TAM phenotype (Figure 5F). Ultimately, the data suggest that dietary Trp is a key driver of immune phenotype in the PDAC TME by serving as a source of indoles via microbiome metabolization.

AHR expression and activity correlates with patient outcomes in human pancreatic ductal adenocarcinoma

Pan-cancer analysis showed that PDAC exhibits higher *AHR* compared with most other cancer types (Figure 6A). We then examined correlation of *AHR* expression with survival. In PDAC patients, *AHR* expression below the median value was associated with improved overall survival (OS) compared with patients above the median (Figures 6B, panel 1 and S5A), and when we grouped patients into quartiles based on relative *AHR*, we observed the best OS in the lowest *AHR* quartile (Q1), whereas the other expression quartiles did not show differential OS. This suggested a benefit for patients with low *AHR* expression. Although the difference in OS among the quartiles was not significant (Figure 6B, panel 2), hazard ratios suggested that *AHR* expression was a risk factor for death (Figure S5B). Thus, we surmised that a threshold of *AHR* expression may compromise survival in PDAC. In agreement with this, Q1 showed an improvement in OS when compared with all other PDAC patients (Figure 6B, panel 3). Thus, overall, the relationship of *AHR* to OS suggests that low *AHR* expression may be beneficial for survival, but even moderate expression may negatively impact outcomes.

A follow-on prediction from these results is that AhR activity may impact survival by altering immunity in the TME. To test this, we applied a human AhR transcriptional signature (AhTS) (Goudot et al., 2017), examining correlation with T cell and macrophage gene expression in the PDAC TCGA cohort. We observed moderate negative correlation of the AhTS with expression of the macrophage markers *CD68, CD206* (*MRC1*), and *CD40*, suggesting macrophage density was negatively impacted by AhR activity (Figure 6C). Genes associated with $CD8^+$ T cells and effector function also showed a negative correlation with the AhTS (Figure 6C). Thus, the data show that AhR gene signatures correlate with a paucity of T cells transcriptional signatures in the TME and a cold tumor overall, whereas reduced AhTSs predicts increased cytolytic $CD8^+$ T cell presence and inflammation.

We then examined *AHR* expression in a single-cell dataset from treatment naive PDAC patients and non-malignant tumor adjacent pancreas tissue (Steele et al., 2020). *AHR* had the highest and broadest expression in epithelial and macrophage clusters (Figures 6D–6F). In macrophage clusters, *AHR* expression showed a high degree of similarity with *CD163* (a gene associated with alternative polarization) (Ambarus et al., 2012) and *SIRPA* (a key inhibitor of phagocytosis of self-cells) (Figure 6F), suggesting that *AHR* expression is associated with regulatory TAM populations in the PDAC TME. We then compared the similarity of *AHR* expression across all cell clusters, identifying the top 25 genes most similar to *AHR* in relative level and distribution of cellular expression (Figure S5C). Using this dataset, we performed gene set enrichment analysis to test for general cellular expression patterns. When we probed the HuBMAP ASCT plus B dataset, the highest cellular enrichment indicated was interstitial macrophages (Figure 6G). Similarly, for the Human Gene Atlas, the gene set

(C–E) Day-14 tumors were collected from B6 mice on Trp+/− diet with or without daily IAA or ILA gavage, and flow cytometry analysis of the intra-tumoral infiltrates was performed for the markers indicated. MDCSs were defined as $CD11b^+GR1^+MHCII^{lo}$, and TAMs were defined as $CD11b^+F4/80^+$; the T cells were $CD3^+CD8^+$ cells. MFI, mean fluorescence intensity.

(F) $CD45^+CD11b^+F4/80^+$ TAMs were sorted from day-14 tumors from mice treated with IAA as in (C). The mRNA indicated were then measured by qrt-PCR and normalized against *βactin* as described in STAR Methods. (see also Figure S4). * p <.05, ** p <.01, *** p <.001, NS- not significant.

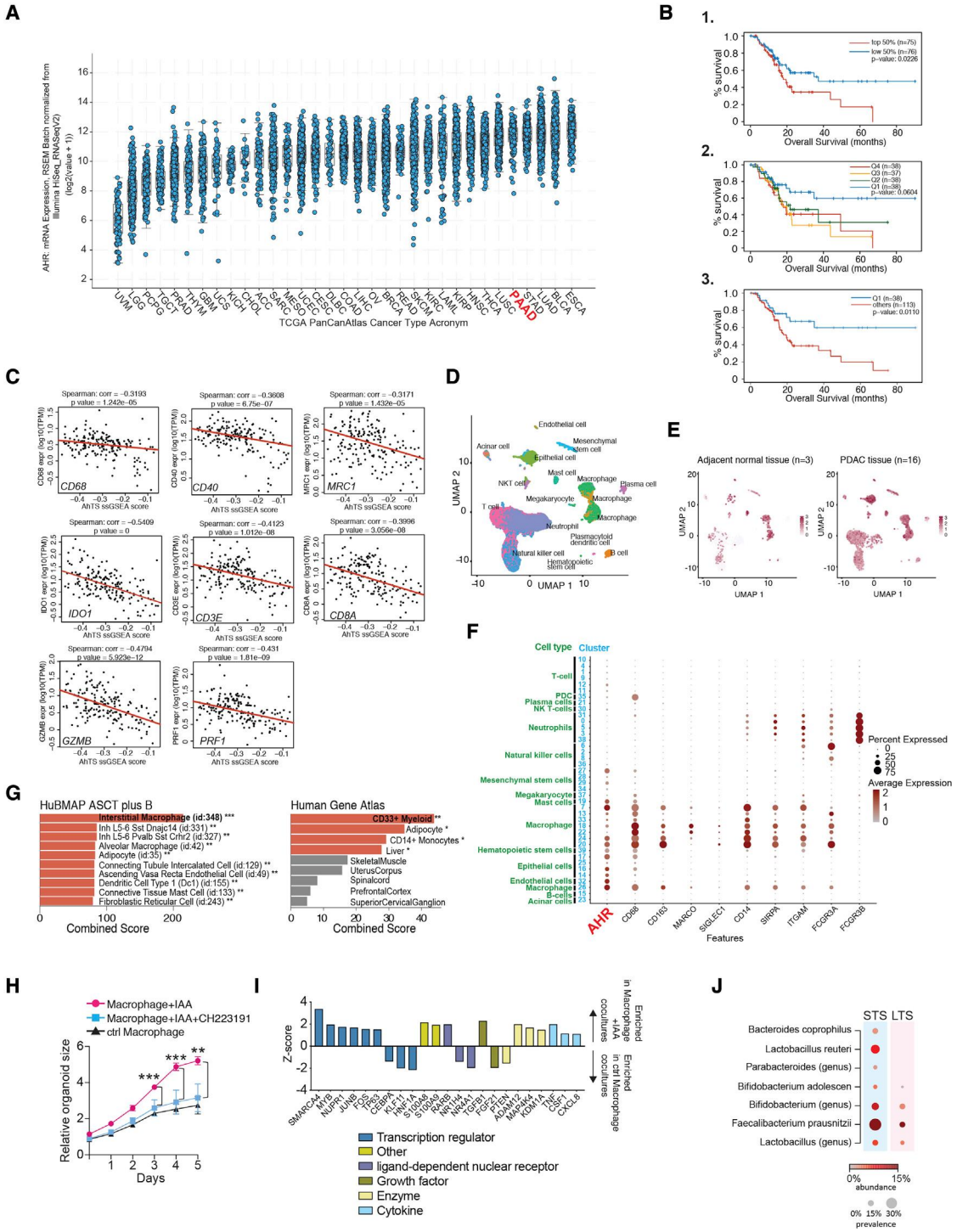

Figure 6. *AHR* expression and activity correlates with patient outcomes in human PDAC

(A) Pan-cancer TCGA analysis showing relative *AHR expression* across 32 cancer types.

(B) Overall survival of the PAAD (PDAC) TCGA patient dataset grouped based on relative *AHR* expression. Patients were grouped based on 1-median *AHR* expression. 2-quartiles of *AHR* expression. Q1 < Q2 < Q3 < Q4. 3- Q1 survival compared with all other quartiles combined.

(C) ssGSEA analysis was performed by examining correlation between the AhR transcriptional signature and the indicated genes in the PAAD-TCGA dataset. Red line is the quartile regression as described in STAR Methods.

(D) UMAP showing scRNA-seq data of 46,244 cells from human PDAC tumor samples and 8,542 cells from adjacent unaffected tissue.

(E) UMAPs of scRNA-seq from indicated samples showing relative *AHR* expression.

(F) Normalized expression and per cluster percentage expression of the genes indicated for each cell cluster for the scRNA-sequencing analysis described in (D).

(legend continued on next page)

enriched for CD33$^+$ myeloid cells and CD14$^+$ monocytes (Figure 6G). Thus, *AHR* is highly expressed in subsets of alternatively activated TAMs in the PDAC TME and is associated with gene set enrichment in myeloid cells across tissue types.

In addition to immune-suppressive function, macrophages can provide direct stromal support to PDAC tumors. Since AhR can induce expression of growth factors, including VEGF and TGFα, we postulated that AhR activation in macrophage may drive a phenotype that could directly support tumor growth. To test this, we co-cultured PBMC-derived macrophage (Halaby et al., 2019) exposed to IAA with PDAC patient-derived organoids (PDO). In the presence of control PBMC-derived macrophages, organoids doubled in size over 5 days (Figure 6D). Co-culture of the PDO with IAA-exposed macrophages increased PDO growth compared with control cultures (Figure 6D). Importantly, addition of the AhR antagonist CH223191 to the macrophages prior to co-culture abrogated the increased growth effect, showing that IAA stimulation improved PDO growth due to the activation of macrophage AhR (Figure 6D). RNA-seq analysis showed that co-culture with IAA-exposed macrophages altered the expression of 235 genes in the PDO (Table S1). iGSEA enrichment analysis of the differentially expressed genes in the PDO co-cultured with control macrophages versus IAA-treated macrophages showed that indole-treated macrophage cultures increased enrichment of pathways associated with PDAC growth and metastasis and reduced enrichment of genes associated with negative regulation of PDAC proliferative potential (e.g., the CEBPA pathway) (Lourenço and Coffer, 2017) (Figure 6D). Altogether, the data show that indoles induce macrophages to acquire a PDAC-supporting phenotype by an AhR-driven mechanism.

Riquelme et al. described a set of PDAC that survived more than 5 years post-resection (long-term survivors [LTS]), identifying local TME and fecal microbial diversity and enrichment for taxa in the LTS patients correlating with this effect (Riquelme et al., 2019). Importantly, FMT experiments suggested that, although microbiota from LTS patients reduced tumor PDAC burden in mice, FMTs from patients who survived less than 5 years post-surgery (matched STS) had a detrimental effect on tumor burden (Riquelme et al., 2019). This result implied that the microbiota from STS contain taxa that could actively contribute to PDAC progression worsening disease. A number of bacterial taxa from the *Bacteroides*, *Bifidobacterium*, *Clostridium*, and *Lactobacillus* genera are prominent producers of indoles (Cervantes-Barragan et al., 2017; Dodd et al., 2017; Elsden et al., 1976; Smith and Macfarlane, 1996), and we hypothesized that the worse outcomes in STS may correlate with increased abundance and/or prevalence of indole-producing bacterial taxa in the local tumor microbiome. Thus, we examined the Riquelme et al. intra-tumoral microbiome dataset to test the prevalence and relative abundance of a set of 20 indole-producing (i.e., IAA, ILA, and IAld) bacterial taxa (Table S2), examining their prevalence within the samples of the cohorts and the average relative abundance between STS and LTS patient groups (Figure 6F). We found an increased prevalence of *L. reuteri* in STS over LTS, with 5/21 STS patients displaying a relative abundance of *L. reuteri* above 2%, whereas none of the LTS patients displayed any detectable relative abundance of *L. reuteri* upon filtering. Similar increases were seen for other indole-producing bacteria or genera of known indole-producing bacteria, such as *Bacteroides coprophilus*, *Faecalibacterium prausnitzi*, and the *Lactobacillus* and *Bifidobacterum* genera (Figure 6F). Thus, the data suggest that enrichment of indole-producing bacteria in the local TME correlates with poor response to resection and OS in PDAC.

DISCUSSION

In some cancers, the gut microbiota influence therapeutic responses to checkpoint inhibitor therapy (Gopalakrishnan et al., 2018; Matson et al., 2018; Routy et al., 2018). The local tumor microbiota in PDAC influences survival independent of immune therapy (Riquelme et al., 2019). However, mechanisms directly linking either the local tumor or the gut microbiome to cancer progression are not well understood. We examined the connection between AhR and microbial indole production extensively, characterizing the immune TME and directly testing the ability of indole-producing bacteria and indoles to activate AhR and promote immune suppression and tumor growth. We found that macrophage AhR function promotes the expression of *Arg1* and *Il10* in TAMs and inhibits IFNγ expression in CD8$^+$ T cells. The observation that *AHR* expression correlates with poor outcomes and reduced immune signatures in human PDAC and indole-exposed human Mφ support PDAC organoid growth in an AhR-dependent mechanism suggests analogous function in human disease.

AhR is an important sensor for bacterial indoles produced via utilization of Trp as an energy source (Shinde and McGaha, 2018). In this report, we demonstrated that loss of the gut microbiome, or removal of dietary Trp phenocopied macrophage *Ahr* deletion; importantly, the effect could be rescued by provision of indoles. A recent report suggested that the microbiome can promote tumor growth by TLR-dependent stimulation of innate inflammation locally with enrichment of *Bifidobacterium* (Pushalkar et al., 2018). *Bifidobacterium* species were not a significant constituent of the microbiome in our mice; however, the *Bifidobacterium* genus was enriched in the microbiome of the STS in our human PDAC microbiome analysis, albeit to a much lesser extent when compared with other taxa. Nevertheless, *Bifidobacterium* spp. are known producers of ILA (Aragozzini et al., 1979; Russell et al., 2013), indicating that the association with oncogenesis in animal models and poor outcomes in human PDAC may be linked to the capacity to produce indoles. This prediction is strengthened by our results, directly comparing the tumorigenic potential of *Lactobacillus* species that were differentiated by the ability to produce indoles. The fact that indole-producing

(G) GSEA of *AHR+25* most similar genes for the indicated gene sets. Bars show relative p value, orange bars = p value <0.05, gray bars were not significant.
(H) 5-day growth curve of human PDAC PDO cultured with PBMC-derived macrophages treated as indicated prior to initiation of the co-culture. Each data point represents the mean value for triplicate samples +/− the standard deviation.
(I) *Z* score for iGSEA analysis of differential gene set enrichment of PDAC PDO/macrophage co-culture at day 5. Colored bars correspond to selected classifiers.
(J) The relative prevalence and abundance of indole-producing bacterial taxa in the tumor microbiome for short-term surviving (STS) versus long-term surviving (LTS) PDAC patients. Results are sorted by odds ratio of bacterial presence in STS versus LTS in descending order. (see also Figure S5). ** p <.01, *** p <.001.

Lactobacilli drastically increase tumor size, with an increase in MDSC numbers and a reduction in activated $CD8^+$ T cells and TNFα production, suggests that indole production by microbiota is an important force influencing immunity in the TME. Recently, a role for TAM AhR function was also identified in glioblastoma multiforme (GBM), driving CD39 expression and impairing T cell responses (Takenaka et al., 2019). This study, along with the data from our paper, strongly supports the prediction that macrophage AhR is a central driver of TAM function responding to multiple inputs to drive an immune-suppressive phenotype in the TME.

Therapeutic targeting of the microbiome has been a sought-after goal for cancer treatment. As such, the approaches had generally fallen into two categories: (1) FMT or (2) specific gut enrichment of bacterial consortia associated with therapeutic response. Indeed, a recent report has shown that a single FMT from melanoma patients responsive to αPD-1 therapy to αPD-1 refractive recipients promoted the accumulation of $CD8^+$ T cells and acquired responsiveness to αPD1 therapy (Davar et al., 2021). However, this approach may be limited in utility because of the lack of knowledge regarding specific taxa driving positive therapeutic responses and variability of key taxa engraftment. Our results suggest that targeting immunologic responses to the microbiome could have meaningful impact on therapy, augmenting microbiome manipulation approaches or potentially bypassing the need to manipulate the microbiome by precise inhibition of the response to microbial metabolites.

In conclusion, we found that macrophage AhR has a strong impact on tumor growth and the TME in pancreatic cancer. The link we identified between AhR, immune function, indoles, and microbiome constituents may provide useful prognostics for predicting patient outcomes.

Limitations of the study

Our study leaves open several questions. The chief among them is why the microbiome appears to serve a dominant role in AhR activation in our study, whereas well-known, Trp metabolizing mammalian enzymatic pathways appear to play a negligible role in the modulation of AhR function. In contrast to our findings, others have reported PDAC tumor cells can produce L-Kyn via an IDO- or TDO-dependent mechanism driving AhR activity (Wang et al., 2020). This dichotomy with our current study is likely reflective of the diverse and variable role of the microbiome versus IDO in shaping the TME in a heterogeneous disease, such as PDAC. Thus, it will be important in future experiments to examine conditions that predicate IDO versus microbiome contribution to AhR function in the TME. Second, in contrast to other reports, we could not detect intra-tumoral bacteria by PCR or 16S sequencing. The reasons for the dichotomy are not clear; however, our use of defined, cultured mouse feces-isolated bacteria may impact dissemination from the gut to the tumor. Third, although we show that pharmacologic inhibition of AhR improves responses to therapy, there are limitations to the application of AhR blockade in cancer due to the variable extent and composition of the tumor immune infiltrate and microbiome taxa. Finally, there is a difference in AhR-ligand-binding affinities between mouse and human (Flaveny and Perdew, 2009; Hubbard et al., 2015) that must be considered when applying data derived from mouse models to clinical disease. Nevertheless, a first-in-human clinical trial targeting AhR has been initiated in patients with advanced solid lung, colorectal, and urothelial tumors (clinicalTrials.gov identifier: NTC04069026), indicating potential applicability of AhR inhibition in multiple cancer types. Ultimately, these trials will provide a definitive test as to whether AhR is a legitimate target for cancer therapy.

STAR★METHODS

Detailed methods are provided in the online version of this paper and include the following:

- KEY RESOURCES TABLE
- RESOURCE AVAILABILITY
  - Lead contact
  - Materials availability
  - Data code and availability
- EXPERIMENTAL MODEL AND SUBJECT DETAILS
- METHODS DETAIL
  - Tumor implantation and tumor induction
  - Isolation of bacteria from mouse intestine
  - Bacterial culture for metabolomics analysis
  - Antibiotic treatment to remove microbiota
  - Microbiota transplantation in SPF mice
  - Germ free microbiota transplantation
  - Bulk RNA-sequencing and analysis
  - scRNA-sequencing and analysis
  - Pan cancer TCGA analysis
  - Analysis of human PDAC scRNA sequencing
  - PDAC organoid culture
  - Metabolomic Sample Preparation
  - Time-of-Flight mass cytometry (CyTOF)
  - Flow Cytometry
  - INFγ blocking or αCD8 T cell delpetion
  - Tryptophan-deficient diet and indole gavage
  - Metabolomics
  - 16S rRNA gene sequencing
  - Analysis of the bacterial microbiome
- QUANTIFICATION AND STATISTICAL ANALYSIS

SUPPLEMENTAL INFORMATION

Supplemental information can be found online at https://doi.org/10.1016/j.immuni.2022.01.006.

ACKNOWLEDGMENTS

We thank Kate Banks, Karen Parisien, and Amy Cao from the University of Toronto Germ Free Mouse Core for assistance in establishing the germ free orthotopic PDAC mouse model. In addition, we thank Dr. Kieran Manion for assistance with graphical abstract images. We also thank Dr. Hal Berman for pathologic assessment of mouse PDAC tumors. This work was supported by NIH grants R01AR067763, R01CA190449, R01CA255670, the Terry Fox Research Institute New Frontiers Program, Medicine by Design-Canada First Research Excellence Fund, the John R. Evans Leaders Fund, and project grants from the Canadian Institutes of Health Research (T.L.M.).

AUTHOR CONTRIBUTIONS

T.L.M. designed and supervised the research. K.H., R.S., S.L., M.T.C., E.G.F., D.C., L.N., K.L., P.M., X.Z., and I.C. executed the biochemical, cell biological,

and *in vitro* experiments. M.J.H., K.H., and S.L. performed the animal experiments. A.K. and R.Q. analyzed the RNA-seq results. G.H.J. analyzed the TCGA data and T.J.P. performed the pan-cancer TCGA analysis. D.P. conducted and analyzed the mass spectrometry data and interpreted the results. H.M. analyzed the 16S rRNA-sequencing data. A.M., B.G., R.K., P.S.O., G.O., S.G., W.W.N., D.P., and D.G.B. contributed reagents, human samples, and discussions. K.H., R.S., A.K., M.J.H., R.Q., M.T.C., T.J.P., D.P., G.J., H.M., and T.L.M. prepared figures and conducted statistical analysis and T.L.M. wrote the paper.

DECLARATION OF INTERESTS

The authors have no conflicting interests to declare.

Received: April 5, 2021
Revised: October 19, 2021
Accepted: January 7, 2022
Published: February 8, 2022

REFERENCES

Afik, R., Zigmond, E., Vugman, M., Klepfish, M., Shimshoni, E., Pasmanik-Chor, M., Shenoy, A., Bassat, E., Halpern, Z., Geiger, T., et al. (2016). Tumor macrophages are pivotal constructors of tumor collagenous matrix. J. Exp. Med. *213*, 2315–2331. https://doi.org/10.1084/jem.20151193.

Ambarus, C.A., Krausz, S., van Eijk, M., Hamann, J., Radstake, T.R., Reedquist, K.A., Tak, P.P., and Baeten, D.L. (2012). Systematic validation of specific phenotypic markers for in vitro polarized human macrophages. J. Immunol. Methods *375*, 196–206. https://doi.org/10.1016/j.jim.2011.10.013.

Aragozzini, F., Ferrari, A., Pacini, N., and Gualandris, R. (1979). Indole-3-lactic acid as a tryptophan metabolite produced by Bifidobacterium spp. Appl. Environ. Microbiol. *38*, 544–546. https://doi.org/10.1128/AEM.38.3.544-546.1979.

Boj, S.F., Hwang, C.-I., Baker, L.A., Chio, I.I.C., Engle, D.D., Corbo, V., Jager, M., Ponz-Sarvise, M., Tiriac, H., Spector, M.S., et al. (2015). Organoid models of human and mouse ductal pancreatic cancer. Cell *160*, 324–338. https://doi.org/10.1016/j.cell.2014.12.021.

Braumüller, H., Wieder, T., Brenner, E., Aßmann, S., Hahn, M., Alkhaled, M., Schilbach, K., Essmann, F., Kneilling, M., Griessinger, C., et al. (2013). T-helper-1-cell cytokines drive cancer into senescence. Nature *494*, 361–365. https://doi.org/10.1038/nature11824.

Butler, A., Hoffman, P., Smibert, P., Papalexi, E., and Satija, R. (2018). Integrating single-cell transcriptomic data across different conditions, technologies, and species. Nat. Biotechnol. *36*, 411–420. https://doi.org/10.1038/nbt.4096.

Cao, Y., Wang, X., and Peng, G. (2020). SCSA: a cell type annotation tool for single-cell RNA-seq data. Front. Genet. *11*, 490. https://doi.org/10.3389/fgene.2020.00490.

Caporaso, J.G., Kuczynski, J., Stombaugh, J., Bittinger, K., Bushman, F.D., Costello, E.K., Fierer, N., Peña, A.G., Goodrich, J.K., Gordon, J.I., et al. (2010). QIIME allows analysis of high-throughput community sequencing data. Nat. Methods *7*, 335–336. https://doi.org/10.1038/nmeth.f.303.

Cervantes-Barragan, L., Chai, J.N., Tianero, M.D., Di Luccia, B., Ahern, P.P., Merriman, J., Cortez, V.S., Caparon, M.G., Donia, M.S., Gilfillan, S., et al. (2017). Lactobacillus reuteri induces gut intraepithelial CD4+CD8alphaalpha+ T cells. Science *357*, 806–810. https://doi.org/10.1126/science.aah5825.

Chen, X., Willette-Brown, J., Wu, X., Hu, Y., Howard, O.M., Hu, Y., and Oppenheim, J.J. (2015). IKKalpha is required for the homeostasis of regulatory T cells and for the expansion of both regulatory and effector CD4 T cells. FASEB J. *29*, 443–454. https://doi.org/10.1096/fj.14-259564.

Chong, J., Liu, P., Zhou, G., and Xia, J. (2020). Using MicrobiomeAnalyst for comprehensive statistical, functional, and meta-analysis of microbiome data. Nat. Protoc. *15*, 799–821. https://doi.org/10.1038/s41596-019-0264-1.

Cuadrado, E., van den Biggelaar, M., de Kivit, S., Chen, Y.-Y., Slot, M., Doubal, I., Meijer, A., van Lier, R.A.W., Borst, J., and Amsen, D. (2018). Proteomic analyses of human regulatory T cells reveal adaptations in signaling pathways that protect cellular identity. Immunity *48*, 1046–1059.e6. https://doi.org/10.1016/j.immuni.2018.04.008.

D'Arcangelo, E., Wu, N.C., Chen, T., Shahaj, A., Cadavid, J.L., Huang, L., Ailles, L., and McGuigan, A.P. (2020). Gels for live analysis of compartmentalized environments (GLAnCE): a tissue model to probe tumour phenotypes at tumour-stroma interfaces. Biomaterials *228*, 119572. https://doi.org/10.1016/j.biomaterials.2019.119572.

Davar, D., Dzutsev, A.K., McCulloch, J.A., Rodrigues, R.R., Chauvin, J.-M., Morrison, R.M., Deblasio, R.N., Menna, C., Ding, Q., Pagliano, O., et al. (2021). Fecal microbiota transplant overcomes resistance to anti-PD-1 therapy in melanoma patients. Science *371*, 595–602. https://doi.org/10.1126/science.abf3363.

de Vries, J., de Vries, S., Curtis, B.A., Zhou, H., Penny, S., Feussner, K., Pinto, D.M., Steinert, M., Cohen, A.M., von Schwartzenberg, K., and Archibald, J.M. (2020). Heat stress response in the closest algal relatives of land plants reveals conserved stress signaling circuits. Plant J. *103*, 1025–1048. https://doi.org/10.1111/tpj.14782.

Dejean, A.S., Beisner, D.R., Ch'en, I.L., Kerdiles, Y.M., Babour, A., Arden, K.C., Castrillon, D.H., DePinho, R.A., and Hedrick, S.M. (2009). Transcription factor Foxo3 controls the magnitude of T cell immune responses by modulating the function of dendritic cells. Nat. Immunol. *10*, 504–513. https://doi.org/10.1038/ni.1729.

DeNardo, D.G., and Ruffell, B. (2019). Macrophages as regulators of tumour immunity and immunotherapy. Nat. Rev. Immunol. *19*, 369–382. https://doi.org/10.1038/s41577-019-0127-6.

Dhariwal, A., Chong, J., Habib, S., King, I.L., Agellon, L.B., and Xia, J. (2017). MicrobiomeAnalyst: a web-based tool for comprehensive statistical, visual and meta-analysis of microbiome data. Nucleic Acids Res. *45*, W180–W188. https://doi.org/10.1093/nar/gkx295.

Dias, S., D'Amico, A., Cretney, E., Liao, Y., Tellier, J., Bruggeman, C., Almeida, F.F., Leahy, J., Belz, G.T., Smyth, G.K., et al. (2017). Effector regulatory T cell differentiation and immune homeostasis depend on the transcription factor Myb. Immunity *46*, 78–91. https://doi.org/10.1016/j.immuni.2016.12.017.

Dobin, A., Davis, C.A., Schlesinger, F., Drenkow, J., Zaleski, C., Jha, S., Batut, P., Chaisson, M., and Gingeras, T.R. (2013). STAR: ultrafast universal RNA-seq aligner. Bioinformatics *29*, 15–21. https://doi.org/10.1093/bioinformatics/bts635.

Dodd, D., Spitzer, M.H., Van Treuren, W., Merrill, B.D., Hryckowian, A.J., Higginbottom, S.K., Le, A., Cowan, T.M., Nolan, G.P., Fischbach, M.A., and Sonnenburg, J.L. (2017). A gut bacterial pathway metabolizes aromatic amino acids into nine circulating metabolites. Nature *551*, 648–652. https://doi.org/10.1038/nature24661.

Elsden, S.R., Hilton, M.G., and Waller, J.M. (1976). The end products of the metabolism of aromatic amino acids by Clostridia. Arch. Microbiol. *107*, 283–288. https://doi.org/10.1007/BF00425340.

Flaveny, C.A., and Perdew, G.H. (2009). Transgenic humanized AHR mouse reveals differences between human and mouse AHR ligand selectivity. Mol. Cell. Pharmacol. *1*, 119–123. https://doi.org/10.4255/mcpharmacol.09.15.

Fragale, A., Gabriele, L., Stellacci, E., Borghi, P., Perrotti, E., Ilari, R., Lanciotti, A., Remoli, A.L., Venditti, M., Belardelli, F., and Battistini, A. (2008). IFN regulatory factor-1 negatively regulates CD4+ CD25+ regulatory T cell differentiation by repressing Foxp3 expression. J. Immunol. *181*, 1673–1682. https://doi.org/10.4049/jimmunol.181.3.1673.

Franchini, A.M., Myers, J.R., Jin, G.-B., Shepherd, D.M., and Lawrence, B.P. (2019). Genome-wide transcriptional analysis reveals novel AhR targets that regulate dendritic cell function during influenza A virus infection. Immunohorizons *3*, 219–235. https://doi.org/10.4049/immunohorizons.1900004.

Gopalakrishnan, V., Spencer, C.N., Nezi, L., Reuben, A., Andrews, M.C., Karpinets, T.V., Prieto, P.A., Vicente, D., Hoffman, K., Wei, S.C., et al. (2018). Gut microbiome modulates response to anti-PD-1 immunotherapy in melanoma patients. Science *359*, 97–103. https://doi.org/10.1126/science.aan4236.

Goudot, C., Coillard, A., Villani, A.-C., Gueguen, P., Cros, A., Sarkizova, S., Tang-Huau, T.-L., Bohec, M., Baulande, S., Hacohen, N., et al. (2017). Aryl hydrocarbon receptor Controls Monocyte Differentiation into dendritic Cells versus Macrophages. Immunity *47*, 582–596.e6. https://doi.org/10.1016/j.immuni.2017.08.016.

Halaby, M.J., Hezaveh, K., Lamorte, S., Ciudad, M.T., Kloetgen, A., MacLeod, B.L., Guo, M., Chakravarthy, A., Medina, T.D.S., Ugel, S., et al. (2019). GCN2 drives macrophage and MDSC function and immunosuppression in the tumor microenvironment. Sci. Immunol. *4*. https://doi.org/10.1126/sciimmunol.aax8189.

Halbrook, C.J., Pontious, C., Kovalenko, I., Lapienyte, L., Dreyer, S., Lee, H.-J., Thurston, G., Zhang, Y., Lazarus, J., Sajjakulnukit, P., et al. (2019). Macrophage-released pyrimidines inhibit gemcitabine therapy in pancreatic cancer. Cell Metab *29*, 1390–1399.e6. https://doi.org/10.1016/j.cmet.2019.02.001.

Hubbard, T.D., Murray, I.A., Bisson, W.H., Lahoti, T.S., Gowda, K., Amin, S.G., Patterson, A.D., and Perdew, G.H. (2015). Adaptation of the human aryl hydrocarbon receptor to sense microbiota-derived indoles. Sci. Rep. *5*, 12689. https://doi.org/10.1038/srep12689.

Korsunsky, I., Millard, N., Fan, J., Slowikowski, K., Zhang, F., Wei, K., Baglaenko, Y., Brenner, M., Loh, P.-R., and Raychaudhuri, S. (2019). Fast, sensitive and accurate integration of single-cell data with Harmony. Nat. Methods *16*, 1289–1296. https://doi.org/10.1038/s41592-019-0619-0.

Levine, J.H., Simonds, E.F., Bendall, S.C., Davis, K.L., Amir, E-a.D., Tadmor, M.D., Litvin, O., Fienberg, H.G., Jager, A., Zunder, E.R., et al. (2015). Data-driven phenotypic dissection of AML reveals progenitor-like cells that correlate with prognosis. Cell *162*, 184–197. https://doi.org/10.1016/j.cell.2015.05.047.

Liao, X., Sharma, N., Kapadia, F., Zhou, G., Lu, Y., Hong, H., Paruchuri, K., Mahabeleshwar, G.H., Dalmas, E., Venteclef, N., et al. (2011). Kruppel-like factor 4 regulates macrophage polarization. J. Clin. Invest. *121*, 2736–2749. https://doi.org/10.1172/JCI45444.

Lourenço, A.R., and Coffer, P.J. (2017). A tumor suppressor role for C/EBPalpha in solid tumors: more than fat and blood. Oncogene *36*, 5221–5230. https://doi.org/10.1038/onc.2017.151.

Maddipati, R., and Stanger, B.Z. (2015). Pancreatic cancer metastases harbor evidence of polyclonality. Cancer Discov. *5*, 1086–1097. https://doi.org/10.1158/2159-8290.CD-15-0120.

Madisen, L., Zwingman, T.A., Sunkin, S.M., Oh, S.W., Zariwala, H.A., Gu, H., Ng, L.L., Palmiter, R.D., Hawrylycz, M.J., Jones, A.R., et al. (2010). A robust and high-throughput Cre reporting and characterization system for the whole mouse brain. Nat. Neurosci. *13*, 133–140. https://doi.org/10.1038/nn.2467.

Matson, V., Fessler, J., Bao, R., Chongsuwat, T., Zha, Y., Alegre, M.L., Luke, J.J., and Gajewski, T.F. (2018). The commensal microbiome is associated with anti-PD-1 efficacy in metastatic melanoma patients. Science *359*, 104–108. https://doi.org/10.1126/science.aao3290.

Monteleone, I., Rizzo, A., Sarra, M., Sica, G., Sileri, P., Biancone, L., MacDonald, T.T., Pallone, F., and Monteleone, G. (2011). Aryl hydrocarbon receptor-induced signals up-regulate IL-22 production and inhibit inflammation in the gastrointestinal tract. Gastroenterology *141*, 237–248. 248.e1. https://doi.org/10.1053/j.gastro.2011.04.007.

Murray, I.A., Patterson, A.D., and Perdew, G.H. (2014). Aryl hydrocarbon receptor ligands in cancer: friend and foe. Nat. Rev. Cancer *14*, 801–814. https://doi.org/10.1038/nrc3846.

Pino, L.K., Searle, B.C., Bollinger, J.G., Nunn, B., MacLean, B., and MacCoss, M.J. (2020). The Skyline ecosystem: informatics for quantitative mass spectrometry proteomics. Mass Spectrom. Rev. *39*, 229–244. https://doi.org/10.1002/mas.21540.

Price, M.N., Dehal, P.S., and Arkin, A.P. (2009). FastTree: computing large minimum evolution trees with profiles instead of a distance matrix. Mol. Biol. Evol. *26*, 1641–1650. https://doi.org/10.1093/molbev/msp077.

Pushalkar, S., Hundeyin, M., Daley, D., Zambirinis, C.P., Kurz, E., Mishra, A., Mohan, N., Aykut, B., Usyk, M., Torres, L.E., et al. (2018). The pancreatic cancer microbiome promotes oncogenesis by induction of innate and adaptive immune suppression. Cancer Discov. *8*, 403–416. https://doi.org/10.1158/2159-8290.CD-17-1134.

Ravishankar, B., Liu, H., Shinde, R., Chaudhary, K., Xiao, W., Bradley, J., Koritzinsky, M., Madaio, M.P., and McGaha, T.L. (2015). The amino acid sensor GCN2 inhibits inflammatory responses to apoptotic cells promoting tolerance and suppressing systemic autoimmunity. Proc. Natl. Acad. Sci. USA *112*, 10774–10779. https://doi.org/10.1073/pnas.1504276112.

Riquelme, E., Zhang, Y., Zhang, L., Montiel, M., Zoltan, M., Dong, W., Quesada, P., Sahin, I., Chandra, V., San Lucas, A., et al. (2019). Tumor microbiome diversity and composition influence pancreatic cancer outcomes. Cell *178*, 795–806.e12. https://doi.org/10.1016/j.cell.2019.07.008.

Roager, H.M., and Licht, T.R. (2018). Microbial tryptophan catabolites in health and disease. Nat. Commun. *9*, 3294. https://doi.org/10.1038/s41467-018-05470-4.

Robinson, M.D., McCarthy, D.J., and Smyth, G.K. (2010). edgeR: a bioconductor package for differential expression analysis of digital gene expression data. Bioinformatics *26*, 139–140. https://doi.org/10.1093/bioinformatics/btp616.

Rothhammer, V., Borucki, D.M., Tjon, E.C., Takenaka, M.C., Chao, C.-C., Ardura-Fabregat, A., de Lima, K.A., Gutiérrez-Vázquez, C., Hewson, P., Staszewski, O., et al. (2018). Microglial control of astrocytes in response to microbial metabolites. Nature *557*, 724–728. https://doi.org/10.1038/s41586-018-0119-x.

Rothhammer, V., Mascanfroni, I.D., Bunse, L., Takenaka, M.C., Kenison, J.E., Mayo, L., Chao, C.C., Patel, B., Yan, R., Blain, M., et al. (2016). Type I interferons and microbial metabolites of tryptophan modulate astrocyte activity and central nervous system inflammation via the aryl hydrocarbon receptor. Nat. Med. *22*, 586–597. https://doi.org/10.1038/nm.4106.

Routy, B., Le Chatelier, E., Derosa, L., Duong, C.P.M., Alou, M.T., Daillère, R., Fluckiger, A., Messaoudene, M., Rauber, C., Roberti, M.P., et al. (2018). Gut microbiome influences efficacy of PD-1-based immunotherapy against epithelial tumors. Science *359*, 91–97. https://doi.org/10.1126/science.aan3706.

Russell, W.R., Duncan, S.H., Scobbie, L., Duncan, G., Cantlay, L., Calder, A.G., Anderson, S.E., and Flint, H.J. (2013). Major phenylpropanoid-derived metabolites in the human gut can arise from microbial fermentation of protein. Mol. Nutr. Food Res. *57*, 523–535. https://doi.org/10.1002/mnfr.201200594.

Shankaran, V., Ikeda, H., Bruce, A.T., White, J.M., Swanson, P.E., Old, L.J., and Schreiber, R.D. (2001). IFNgamma and lymphocytes prevent primary tumour development and shape tumour immunogenicity. Nature *410*, 1107–1111. https://doi.org/10.1038/35074122.

Shinde, R., Hezaveh, K., Halaby, M.J., Kloetgen, A., Chakravarthy, A., da Silva Medina, T., Deol, R., Manion, K.P., Baglaenko, Y., Eldh, M., et al. (2018). Apoptotic cell-induced AhR activity is required for immunological tolerance and suppression of systemic lupus erythematosus in mice and humans. Nat. Immunol. *19*, 571–582. https://doi.org/10.1038/s41590-018-0107-1.

Shinde, R., and McGaha, T.L. (2018). The aryl hydrocarbon receptor: connecting immunity to the microenvironment. Trends Immunol. *39*, 1005–1020. https://doi.org/10.1016/j.it.2018.10.010.

Smith, E.A., and Macfarlane, G.T. (1996). Enumeration of human colonic bacteria producing phenolic and indolic compounds: effects of pH, carbohydrate availability and retention time on dissimilatory aromatic amino acid metabolism. J. Appl. Bacteriol. *81*, 288–302. https://doi.org/10.1111/j.1365-2672.1996.tb04331.x.

St Paul, M., and Ohashi, P.S. (2020). The roles of CD8+ T cell subsets in antitumor immunity. Trends Cell Biol. *30*, 695–704. https://doi.org/10.1016/j.tcb.2020.06.003.

Steele, N.G., Carpenter, E.S., Kemp, S.B., Sirihorachai, V., The, S., Delrosario, L., Lazarus, J., Amir, E.-A.D., Gunchick, V., Espinoza, C., et al. (2020). Multimodal mapping of the tumor and peripheral blood immune landscape in human pancreatic cancer. Nat. Cancer *1*, 1097–1112. https://doi.org/10.1038/s43018-020-00121-4.

Szabo, S.J., Kim, S.T., Costa, G.L., Zhang, X., Fathman, C.G., and Glimcher, L.H. (2000). A novel transcription factor, T-bet, directs Th1 lineage commitment. Cell *100*, 655–669. https://doi.org/10.1016/S0092-8674(00)80702-3.

Takenaka, M.C., Gabriely, G., Rothhammer, V., Mascanfroni, I.D., Wheeler, M.A., Chao, C.-C., Gutiérrez-Vázquez, C., Kenison, J., Tjon, E.C., Barroso,

A., et al. (2019). Control of tumor-associated macrophages and T cells in glioblastoma via AHR and CD39. Nat. Neurosci. *22*, 729–740. https://doi.org/10.1038/s41593-019-0370-y.

Wang, L., Tang, W., Yang, S., He, P., Wang, J., Gaedcke, J., Ströbel, P., Azizian, A., Ried, T., Gaida, M.M., et al. (2020). NO●/RUNX3/kynurenine metabolic signaling enhances disease aggressiveness in pancreatic cancer. Int. J. Cancer *146*, 3160–3169. https://doi.org/10.1002/ijc.32733.

Wang, Q., Garrity, G.M., Tiedje, J.M., and Cole, J.R. (2007). Naive Bayesian classifier for rapid assignment of rRNA sequences into the new bacterial taxonomy. Appl. Environ. Microbiol. *73*, 5261–5267. https://doi.org/10.1128/AEM.00062-07.

Weisburg, W.G., Barns, S.M., Pelletier, D.A., and Lane, D.J. (1991). 16S ribosomal DNA amplification for phylogenetic study. J. Bacteriol. *173*, 697–703. https://doi.org/10.1128/jb.173.2.697-703.1991.

Wilck, N., Matus, M.G., Kearney, S.M., Olesen, S.W., Forslund, K., Bartolomaeus, H., Haase, S., Mähler, A., Balogh, A., Markó, L., et al. (2017). Salt-responsive gut commensal modulates TH17 axis and disease. Nature *551*, 585–589. https://doi.org/10.1038/nature24628.

Xia, J., and Wishart, D.S. (2016). Using MetaboAnalyst 3.0 for comprehensive metabolomics data analysis. Curr. Protoc. Bioinformatics *55*, 14.10.1–14.10.91. https://doi.org/10.1002/cpbi.11.

Yamauchi, T., Hoki, T., Oba, T., Saito, H., Attwood, K., Sabel, M.S., Chang, A.E., Odunsi, K., and Ito, F. (2020). CX3CR1-CD8+ T cells are critical in antitumor efficacy but functionally suppressed in the tumor microenvironment. JCI Insight *5*. https://doi.org/10.1172/jci.insight.133920.

Zelante, T., Iannitti, R.G., Cunha, C., De Luca, A., Giovannini, G., Pieraccini, G., Zecchi, R., D'Angelo, C., Massi-Benedetti, C., Fallarino, F., et al. (2013). Tryptophan catabolites from microbiota engage aryl hydrocarbon receptor and balance mucosal reactivity via interleukin-22. Immunity *39*, 372–385. https://doi.org/10.1016/j.immuni.2013.08.003.

Zhu, M., Goetsch, S.C., Wang, Z., Luo, R., Hill, J.A., Schneider, J., Morris, S.M., Jr., and Liu, Z.-P. (2015). FoxO4 promotes early inflammatory response upon myocardial infarction via endothelial Arg1. Circ. Res. *117*, 967–977. https://doi.org/10.1161/CIRCRESAHA.115.306919.

Zhu, W., Lönnblom, E., Förster, M., Johannesson, M., Tao, P., Meng, L., Lu, S., and Holmdahl, R. (2020). Natural polymorphism of Ym1 regulates pneumonitis through alternative activation of macrophages. Sci. Adv. *6*. https://doi.org/10.1126/sciadv.aba9337.

Zhu, Y., Herndon, J.M., Sojka, D.K., Kim, K.-W., Knolhoff, B.L., Zuo, C., Cullinan, D.R., Luo, J., Bearden, A.R., Lavine, K.J., et al. (2017). Tissue-resident macrophages in pancreatic ductal adenocarcinoma originate from embryonic hematopoiesis and promote tumor progression. Immunity *47*, 597. https://doi.org/10.1016/j.immuni.2017.08.018.

STAR★METHODS

KEY RESOURCES TABLE

REAGENT or RESOURCE	SOURCE	IDENTIFIER
Antibodies		
Anti-mouse CD8a	BioXCell	Cat# BE0117; RRID: AB_10950145
Anti-mouse INFg Ab	BioXCell	Cat# BE0055; RRID: AB_1107694
IgG1 isotype control	BioXCell	Cat# BE0083; RRID: AB_ 1107784
IgG2a isotype control	BioXCell	Cat# BE0090; RRID: AB_1107780
CD45 (mouse), clone 30-F11	Fluidigm	Cat# 3089005B; RRID:AB_2651152
Ly6C (mouse), clone HK1.4	Biolegend	Cat# 128001; RRID:AB_1134213
GzmB (mouse), clone QA 16a02	Biolegend	Cat# 372202; RRID:AB_2686929
CD44 (mouse), clone IM7	Biolegend	Cat# 103051; RRID:AB_2562799
CD69 (mouse), clone H1.2F3	Fluidigm	Cat# 3143004B; RRID:AB_2827881
CTLA4 (mouse), clone UC104B9	Biolegend	Cat# 106302; RRID:AB_313251
F4/80 (mouse), clone BM8	Fluidigm	Cat# 3146008B; RRID:AB_2895117
CD11b (mouse), clone M1/70	Fluidigm	Cat# 3148003B; RRID:AB_2814738
Nos2 (mouse), clone W16030C	Biolegend	Cat# 696802; RRID:AB_2687097
Ly6G (mouse), clone 1A8	Biolegend	Cat# 127637; RRID:AB_2563784
CD25 (mouse), clone 3C7	Biolegend	Cat# 101913; RRID:AB_2562798
CD3e (mouse), clone 145-2C11	Fluidigm	Cat# 3152004B; RRID:AB_2687836
CD8a (mouse), clone 536.7	Fluidigm	Cat# 3153012B; RRID:AB_2885019
CD103 (mouse), clone Ber-ACT8	Novus Bio	Cat# NBP1-97564; RRID:AB_11189940
PDL1 (mouse), clone 29E.2A3	Biolegend	Cat# 329719; RRID:AB_2565429
Tim3 (mouse), clone F38-2E2	Biolegend	Cat# 345019; RRID:AB_2563790
CD62L (mouse), clone MEL-14	Fluidigm	Cat# 3160008B; RRID:AB_2687840
TBET (mouse), clone 4B10	Biolegend	Cat# 644825; RRID:AB_2563788
FOXP3 (mouse), clone MF-14	Biolegend	Cat# 126401; RRID:AB_1089120
CD86 (mouse), clone IT2.2	Biolegend	Cat# 305435; RRID:AB_2563764
CX3CR1 (mouse), clone SSA011F11	Fluidigm	Cat# 3164023B; RRID:AB_2832247
IFNg (mouse), clone XMG1.2	Biolegend	Cat# 505802; RRID:AB_315396
B220 (mouse), clone RA36B2	Biolegend	Cat# 103249; RRID:AB_2562801
CCL4 (mouse), clone W15194A	Biolegend	Cat# 625504; RRID:AB_2814489
TNFa (mouse), clone mp6xt22	Fluidigm	Cat# 3162002B; RRID:AB_2801437
CD206 (mouse), clone C068C2	Fluidigm	Cat# 3169021B; RRID:AB_2832249
CD4 (mouse), clone RM45	Fluidigm	Cat #3172003B; RRID:AB_2811242
CD11c (mouse), clone N418	Biolegend	Cat# 117301; RRID:AB_313770
PD1 (mouse), clone RMP1-30	Biolegend	Cat# 109113; RRID:AB_2563735
TIGIT (mouse), clone 4D4/m1	Biolegend	Cat# 156102; RRID:AB_2750250
MHCII (mouse), clone m5/114.15.2	Fluidigm	Cat# 3209006B; RRID:AB_2885025
Bacterial and Virus Strains		
Lactobacillus murinus strain NM26_J9	This Paper	NCBI Genome Assembly GCA_004793535.1
Lactobacillus reuteri strain NM11_1-41	This Paper	NCBI Genome Assembly GCA_004793875.1
Lactobacillus johnsonii strain NM60_B2-8	This Paper	NCBI Genome Assembly GCA_004793575.1
Lactobacillus intestinalis strain NM61_E11	This paper	NCBI Genome Assembly GCA_004793775.1
Biological Samples		
Healthy human peripheral blood mononuclear cells (PBMC)	The Princess Margaret Cancer Centre	N/A

(*Continued on next page*)

Continued

REAGENT or RESOURCE	SOURCE	IDENTIFIER
Chemicals, Peptides, and Recombinant Proteins		
3-Indoleacetic acid (IAA)	Sigma Aldrich	Cat# I3750, CAS: 87-51-4
Indole-3-Lactic Acid (ILA)	Sigma Aldrich	Cat# I5508, CAS: 832-97-3
ITE	Tocris	Cat# 1803, CAS: 448906-42-1
FICZ	Millipore Sigma	Cat# SML1489, CAS: 172922-91-7
CH223191	Cayman Chemicals	Cat# 16154, CAS: 301326-22-7
Streptomycin sulfate	Millipore Sigma	Cat# S9137, CAS: 3810-74-0
Clindamycin hydrochloride	Millipore Sigma	Cat# C5269, CAS: 21462-39-5
Vancomycin hydrochloride	Millipore Sigma	Cat# V2002, CAS: 1404-93-9
Indole-3-Carboxyaldehyde (IAld)	Millipore Sigma	Cat# 129445, CAS: 487-89-8
Ampicillin	Millipore Sigma	Millipore Sigma
Metabolomics Amino Acid Mix Standard	Cambridge Isotopes Laboratories Inc	Cat# MSK-A2-1.2
peptone-tryptone media	Sigma-Aldrich	cat# BP1421
Man-Rogosa-Sharpe (MRS) agar	Sigma-Aldrich	cat# 69964
tamoxifen	Sigma-Aldrich	cat# T5648
corn oil	Sigma Aldrich	cat# C8267
Maxpar Staining Buffer	Fluidigm	cat # 201068
TruStain Fc blocking buffer	Biolegend	cat# 101320
Cell_Id cisplatin	Fluidigm	cat# 201064
Cell-ID multiplex Barcoding kit	Fluidigm	cat # 201060
Foxp3 transcription factor staining kit	eBioscience	cat# 00-5523-00
EQ beads	Fluidigm	cat# 201078
Critical Commercial Assays		
SMART-Seq v4 Ultra Low Input 20 536 RNA Kit for Sequencing	Takara	cat# R400752
NexteraXT DNA Library Preparation	Illumina	cat# FC-131-1096
NexteraXT Index Kit V1 or V2 Set A	10X Genomics	cat# PN-1000121 & PN-1000127
Platinum Green Hot Start PCR 2x Master Mix	Invitrogen	cat# 13001013
Monarch PCR & DNA Cleanup Kit	New England Biolabs	cat # T1030S
Deposited Data		
Raw RNA sequencing data	This paper	NCBI GEO accession ID GSE171603
Experimental Models: Cell Lines		
mT4 PDAC cell	Dr. David Tuveson (CSHL)	*Cell*, 160(1-2), 324–338. https://doi.org/10.1016/j.cell.2014.12.021
mT3 PDAC cell line	Dr. David Tuveson (CSHL)	*Cell*, 160(1-2), 324–338. https://doi.org/10.1016/j.cell.2014.12.021
mT5 PDAC cell line	Dr. David Tuveson (CSHL)	*Cell*, 160(1-2), 324–338. https://doi.org/10.1016/j.cell.2014.12.021
Patient derived organoid model	The University Health Network Living Biobank, ON Canada	PPTO.46
Experimental Models: Organisms/Strains		
Mouse: C57BL/6J	Jackson Laboratory	JAX:000664
Mouse: B6.*Ahr*$^{fl/fl}$	Jackson Laboratory	JAX:006203
Mouse: B6.Cg-*Gt(ROSA)26Sor*$^{tm9(CAG-tdTomato)Hze}$/J	Jackson Laboratory	JAX:007909
Mouse: *Kras*^{tm4Tyj}*Trp53*^{tm1Brn} Tg (Pdx1-cre/Esr1*)#Dam/J	Jackson Laboratory	Jax: 032429
Mouse: B6.*Lyz2-CRE*	Jackson Laboratory	Jax: 004781

(*Continued on next page*)

Continued

REAGENT or RESOURCE	SOURCE	IDENTIFIER
Oligonucleotides		
AhR CRISPR guide RNA (CTCCACTATCCAAGAT TACC)	GenScript	CrRNA 3
Mouse: Cyp1a1F: 5'-CAAT5'-CCCTTCTCAAATGTCC TGTAGTG-3'R: 5'- CCCTTCTCAAATGTCCTGT AGTG-3',	ThermoFisher Scientific	N/A
Mouse: Cyp1b1 F: 5'-CCACCAGCCTTAGTGC AGAC-3' R: 5'-GGCCAGGACGGAGA AGAGT-3'	ThermoFisher Scientific	N/A
Mouse: Actb F: 5'-AAGAGCTATGAGCTGC CTGA-3' R: 5'-TACGGATGTCAACGTC ACAC-3'	ThermoFisher Scientific	N/A
NM26 (L. Murinus)F: 5'- CCACATGCTAGTGA GCGTATC-3'R: 5'- GTCCAGTTTCTTCTCG CTTCT-3'	ThermoFisher Scientific	N/A
NM11 (L. Reuteri)F: 5'- GGACGCTTAGACCGC AATGTA-3'R: 5'- TCTCAACACCCGCCTT AATC-3'	ThermoFisher Scientific	N/A
Mouse: Arg-1 F: 5'-CTCCAAGCCAAAGTC CTTAGAG-3' R: 5'-GGAGCTGTTCATTAGGG ACATCA-3'	ThermoFisher Scientific	N/A
Mouse: IL-10 F: 5'- ATTTTAATAAGCTCCAA GACCAAGGT-3' R: 5'-CTGCAGGTGTTTTAGCTT TTCATTT-3'	ThermoFisher Scientific	N/A
mOUSE: IDO-1 F: 5'- GAGGATGCGTGACTTT GTGGA-3' R: 5'-TCCCAGACCCCCTCAT ACAG-3'	ThermoFisher Scientific	N/A
Recombinant DNA		
pSpCas9(BB)-2A-GFP	GenScript	Cat# PX458
Software and Algorithms		
FlowJo v10	BD Biosciences	https://www.flowjo.com/
Cytobank	Beckmann Coulter	https://www.mybeckman.ca/flow-cytometry/software/cytobank-premium
infercnv v1.6.0	infercnv v1.6.0inferCNV of the Trinity CTAT Project. https://github.com/broadinstitute/inferCNV	https://github.com/broadinstitute/infercnv
Seurat v4.0.3		https://satijalab.org/seurat/
Harmony v0.1.0	Korsunsky et al., 2019	https://github.com/immunogenomics/harmony
R v4.0.3		https://www.r-project.org/
Prism 7	GraphPad	graphpad.com/scientific-software/prism/
Other		
Trp negative chow diet	Envigo	cat# TD.01084
Amino acid chow diet	Envigo	cat# TD.08126
X-tremeGENE 9 DNA Transfection Reagent	Millipore-Sigma	cat# XTG9-RO

RESOURCE AVAILABILITY

Lead contact

Further information and requests for resources and reagents should be directed to and will be fulfilled by the lead contact, Tracy L. McGaha (tmcgaha@uhnresearch.ca).

Materials availability

This study did not generate new unique reagents.

Data code and availability

Single-cell RNA-seq data have been deposited at GEO and are publicly available as of the date of publicationkey resources table under NCBI GEO accession ID GSE171603.

This paper does not report original code.

Any additional information required to reanalyze the data reported in this paper is available from the lead contact upon request.

EXPERIMENTAL MODEL AND SUBJECT DETAILS

C57BL6/J (*B6*), B6.*Ido1*$^{-/-}$, B6.*Ahr*$^{fl/fl}$, B6.Cg-*Gt(ROSA)26Sor*$^{tm9(CAG-tdTomato)Hze}$/J, tamoxifen-inducible (i)KPC mice (*Kras*^{tm4Tyj} *Trp53*^{tm1Brn} Tg(Pdx1-cre/Esr1*)#Dam/J), and B6.*Lyz2CRE*$^{+/-}$ mice were obtained from Jackson Laboratories and maintained under specific pathogen-free conditions in the Princess Margaret Cancer Centre animal facility. Germ free B6 mice were obtained from and maintained at the University of Toronto germ free core facility. All mice were cared for in accordance with the Canadian Institutional Animal Care and Use Committee guidelines. Female mice 10-12 weeks of age were used for all experiments. Protocols were approved by the Princess Margaret Cancer Centre Animal Care Committee.

METHODS DETAIL

Tumor implantation and tumor induction

Mice were anesthetized with 2% isoflurane in oxygen. A lateral incision was made on the abdominal wall of each mouse and tumors were implanted orthotopically in the pancreas with $10x10^3$ cells of the KPC primary pancreatic adenocarcinoma organoid cell line mT3, mT4, or mT5 (a gift from Dr. David Tuveson) (Boj et al., 2015) resuspended in 80μl of Matrigel (VWR scientific, Cat. # 354234) diluted in PBS at a 1:4 ratio Matrigel/PBS and injected into the tail of the pancreas. Tumor growth was monitored by palpation, and mice were sacrificed 2 weeks after the tumor implantation. At the endpoint, tumors, large intestine fecal and blood specimens were harvested and processed for further analysis.

For induction of tumors in iKPC mice, 8-week-old mice were injected intraperitoneally with tamoxifen dissolved in corn oil for 5 consecutive days at 75mg/kg body weight in a volume of 200μl. 12 weeks after cessation of tamoxifen treatment mice received AhR inhibitor CH22319 intraperitoneally three times a week at a dose of 100 μg/mouse in a 200μl total injection volume.

Isolation of bacteria from mouse intestine

L. reuteri, *L. intestinalis*, *L. johnsonii*, and *L. murinus* strains were isolated from the small intestine of B6 mice through anaerobic culturing on MRS media. Isolated colonies were selected for 16S PCR amplification (Platinum™ Green Hot Start PCR 2x Master Mix) using the universal 16S primers, 8F (8F: AGA GTT TGA TCC TGG CTC AG) and 1492R (1492R: GGT TAC CTT GTT ACG ACT T) (Weisburg et al., 1991) followed by a clean-up step (Monarch® PCR & DNA Cleanup Kit (5 μg), Sanger sequencing of the 16S PCR product using the 1492R primer was performed at The Centre for Applied Genomics, Toronto, ON. Bacterial species were identified by alignment of the 16S sequence using BLASTn against the NCBI database with an alignment of at least 99.5%.

Bacterial culture for metabolomics analysis

Bacteria from glycerol stock were plated on MRS agar plates and incubated anaerobically at 37°C for at least 3 days, after which visible colonies were selected and cultured anaerobically in MRS broth at 37°C. Cultures were incubated at 37 °C for 72hrs. two culture sets per condition were prepared (second set is for checking CFU/OD). Bacteria cultures were then collected and resuspended in 1 mL of test medium (MRS or peptone-tryptone (PT) media +/- tryptophan) and incubated overnight at 37°C anaerobically. Bacteria cultures were centrifuged at 4000xg for 10 minutes and supernatants were collected for metabolomics analysis.

Antibiotic treatment to remove microbiota

Mice were treated 1 g/l ampicillin, 1 g/l metronidazole, 1 g/l neomycin, and 0.5 g/l vancomycin in their drinking water, which was replaced daily for the course of the experiment. Tumor implantations occurred 3d after mice were placed on antibiotic containing water. When indicated mice were placed on drinking water containing only ampicillin or vancomycin at the concentrations indicated above.

Microbiota transplantation in SPF mice

Female B6 were treated for two weeks with an antibiotic solution (ATBx) containing streptomycin (5 mg/ml), and clindamycin (0.1 mg/ml) added to sterile drinking water. Solutions and bottles were changed 3 times a week. After two weeks ATBx treatment was stopped, and the mice were gavaged with pooled *L. murinus* and *L. reuteri* or *L. johnsonii* and *L. intestinalis* cultures. Each gavage contained approximately 10^8 CFU per 200uL (corresponding to an OD 5). Mice received bacterial culture 3 times a week by oral gavage using animal feeding needles before undergoing orthotopic tumor implantation and once/week after the tumor implantation until experimental end points.

Germ free microbiota transplantation

Germ free mice were received single oral gavage of 200ul of bacterial culture (L. murinus) 4 weeks before undergoing orthotopic tumor implantation. Control mice received 200ul of sterile phosphate buffered saline.

Bulk RNA-sequencing and analysis

RNA samples were quantified by qubit (Life Technologies) and an Agilent Bioananlyzer assessed the RNA quality. All samples had RIN above 8. SMART-Seq v4 Ultra Low Input RNA Kit for Sequencing (Clontech #634894) was used per manufacturer's instructions for amplification of RNA and subsequent cDNA synthesis. AMPure XP Bead (Agencourt AMPure beads XP PCR, Beckman Coulter A63881) purification was done manually for the first amplification set. A bead ratio of 1x was used (50μl of AMPure XP beads to 50μl cDNA PCR product with 1μl of 10x lysis buffer added, as per Clontech instructions), and purified cDNA was eluted in 17μl elution buffer provided by Clontech. All samples were quantitated using a Bioanalyzer 2100 Instrument (Agilent Genomics). All samples proceeded through NexteraXT DNA Library Preparation (Illumina FC-131-1096) using NexteraXT Index Kit V1 or V2 Set A (FC-131-1002 or FC-131-2001) following the manufacturer's instructions. An aliquot of all samples was first normalized to 150pg/μl with Nuclease-Free Water (Ambion), then the normalized sample aliquot was used as input material into the NexteraXT DNA Library Prep. AMPure XP bead purification was done using 0.9x bead ratio to sample volume, and all samples were eluted in 22μl of Resuspension Buffer (Illumina). As with the Amplification sets, manual bead purification was done for the first Library set. All samples were run on Agilent Bioanalyzer 2100 using High Sensitivity DNA chips. A portion of this library pool was sent to an outside vendor for sequencing on an Illumina NextSeq HighOutput single read. An average of 400M reads were obtained per pool, with an average of 40M reads/sample across the entire data set.

Raw fastq sequencing reads were aligned against the respective reference genome sequence (GRCm38/mm10 or GRCh37/hg19) using the STAR aligned v2.5.0c (Dobin et al., 2013), discarding all non-uniquely aligned reads. For read counting per annotated gene, we have utilized the STAR function ''–quantMode GeneCounts'', counting reads matching exons of the Ensembl V75 Genes annotation. Further processing was performed with the R Bioconductor package edgeR v.3.14.0 (Robinson et al., 2010) using non-stranded reads. Reads were normalized for intra- and inter-sample variances using the functions ''calcNormFactors'' and ''estimateTagwiseDisp'', resulting in counts-per-million (CPM) for each gene. Differential gene expression analysis was performed with the functions ''glmQLFit'' and ''glmQLFTest'', reporting p-value, false-discovery rate (FDR) and $\log_2$ fold-changes between any possible pair-wise comparison and gene.

scRNA-sequencing and analysis

Tumors from three mice per group were digested, pooled, and stained with DAPI. Live cells were FACS-sorted into buffer (PBS + 2% FBS), washed 2 times with PBS + 0.04% BSA, and then $10x10^3$ cells were mixed with 10X Genomics Chromium single-cell RNA master mix, followed by loading onto a 10X Chromium chip according to the manufacturer's protocol to obtain single-cell cDNA. Libraries were subsequently prepared and sequenced using a NovaSeq sequencer (Illumina).

Single cell raw data was demultiplexed and converted to FASTQ format with Illumina bcl2fastq. We then processed the fastq data with the Cell Ranger Single-Cell Software Suite Version 1.2 (https://support.10xgenomics.com/single-cell-gene-expression/software/pipelines/latest/what-is-cell-ranger) with default parameters according to the 10x genomics guidelines, to align reads against the mouse reference genome (GRCm38/mm10) and to further assign all reads to genes and individual cells based on the barcode information. We filtered all duplicated reads and those not uniquely mapped. Next, Seurat v2.2.1 (Butler et al., 2018) we used to process counts data. We excluded cells with less than 200 detected genes or > 5% mitochondrial transcripts. Expression data was normalized with the NormalizeData function, using the ''LogNormalize'' approach, and further scaled by sequencing depth. Clustering of cells based on gene expression was performed on all cells from both conditions with default parameters (function FindClusters), as well as a cluster-specific marker analysis (FindAllMarkers function), using only genes that were expressed at least in 25% of cells of each particular cluster. Different cell types were assigned to clusters based on known surface markers uniquely expressed in the particular cluster and found as a significant marker (FDR < 0.05). For each defined cluster/cell type, we have performed individual differential gene expression analysis between WT and $Lyz2^{cre/+}Ahr^{fl/fl}$ cells using the FindMarkers function for genes expressed in at least 25% of cells of each particular cluster. For visualization, violin plots of gene expressions were generated based on normalized gene expression data.

Pan cancer TCGA analysis

Gene expression levels were accessed from 10,071 samples from 32 studies curated by cBioPortal.org (cite Gao et al. PMID 23550210) as ''TCGA PanCancer Atlas Studies''. Samples were grouped by TCGA PanCancer Atlas Cancer Type Acronym and

mRNA expression values displayed as RSEM Batch normalized from Illumina HiSeq RNASeqV2. Cancer types were sorted by expression median. Data points were coloured by the presence of specific mutation types as curated by cBioPortal. The full bookmarked query is available as: https://www.cbioportal.org/results/plots?cancer_study_list=laml_tcga_pan_can_atlas_2018%2Cacc_tcga_pan_can_atlas_2018%2Cblca_tcga_pan_can_atlas_2018%2Clgg_tcga_pan_can_atlas_2018%2Cbrca_tcga_pan_can_atlas_2018%2Ccesc_tcga_pan_can_atlas_2018%2Cchol_tcga_pan_can_atlas_2018%2Ccoadread_tcga_pan_can_atlas_2018%2Cdlbc_tcga_pan_can_atlas_2018%2Cesca_tcga_pan_can_atlas_2018%2Cgbm_tcga_pan_can_atlas_2018%2Chnsc_tcga_pan_can_atlas_2018%2Ckich_tcga_pan_can_atlas_2018%2Ckirc_tcga_pan_can_atlas_2018%2Ckirp_tcga_pan_can_atlas_2018%2Clihc_tcga_pan_can_atlas_2018%2Cluad_tcga_pan_can_atlas_2018%2Clusc_tcga_pan_can_atlas_2018%2Cmeso_tcga_pan_can_atlas_2018%2Cov_tcga_pan_can_atlas_2018%2Cpaad_tcga_pan_can_atlas_2018%2Cpcpg_tcga_pan_can_atlas_2018%2Cprad_tcga_pan_can_atlas_2018%2Csarc_tcga_pan_can_atlas_2018%2Cskcm_tcga_pan_can_atlas_2018%2Cstad_tcga_pan_can_atlas_2018%2Ctgct_tcga_pan_can_atlas_2018%2Cthym_tcga_pan_can_atlas_2018%2Cthca_tcga_pan_can_atlas_2018%2Cucs_tcga_pan_can_atlas_2018%2Cucec_tcga_pan_can_atlas_2018%2Cuvm_tcga_pan_can_atlas_2018&Z_SCORE_THRESHOLD=2.0&RPPA_SCORE_THRESHOLD=2.0&data_priority=0&profileFilter=0&case_set_id=all&gene_list=AHR&geneset_list=%20&tab_index=tab_visualize&Action=Submit&plots_horz_selection=%7B%22dataType%22%3A%22clinical_attribute%22%2C%22selectedDataSourceOption%22%3A%22CANCER_TYPE_ACRONYM%22%7D&plots_vert_selection=%7B%22selectedGeneOption%22%3A196%2C%22selectedDataSourceOption%22%3A%22rna_seq_v2_mrna%22%2C%22logScale%22%3A%22true%22%7D&plots_coloring_selection=%7B%22colorByCopyNumber%22%3A%22false%22%7D

Analysis of human PDAC scRNA sequencing

To examine transcriptomics in human PDAC we analyzed a previously published scRNA sequencing dataset using a similar methodology (Steele et al., 2020). Briefly, cells with high mitochondrial reads were filtered out (>10%), as well as cells that were outliers due to oversequencing (total_counts=4836; > 95th percentile) and cells with too few genes (n_genes=581; < 5th percentile). Using the filtered cells, we combined all cells from the PDAC tissue and controls using Harmony (Korsunsky et al., 2019) to create sample and group non-specific clusters that were annotated using the SCSA algorithm (Cao et al., 2020). We then manually resolved any ambiguous annotations using the original publication groupings and known cell-type markers as a reference. UMAP visualization of the was done using the Seurat RunUMAP command with parameters set to 30 dimensions, 10 nearest neighbors, 2 components, 400 epochs, and minimum distance of 0.1. We compared *AHR* expression to our own marker gene set of interest and all genes expressed across all cells. Expression similarity was done on a per-cluster basis, using the clusters inferred from Harmony. For both the mean gene expression and percent-expressed per cluster, we calculated the euclidean distances between AhR and all other genes (n=32,738). We then combined the distance metric using the mean value of both these distances and selected the top 25 for further analysis.

PDAC organoid culture

To visualize the effect of indole acetic acid (IAA)-treated macrophages on organoid growth, human monocyte-derived macrophages (MDMs) were grown in the presence of hM-CSF for 5 days. They were then treated with 250 μM IAA overnight or left untreated (control). Macrophages were lifted off the plates using PBS+ 2% FBS+ 2mM EDTA. They were then labeled with DiD for 5 minutes at 37°C and washed twice in complete medium. GFP-labeled PDAC organoid (Pancreatic Organoid, Tumor, PMLB PPTO.46 from the University Health Network Living Biobank, Toronto, Canada) domes were grown for 4 days in matrigel. The PDAC organoids were then freed from the matrigel domes by gently pipetting up and down. Ice cold advanced DMEM/F12 (AD/F12) was added to the organoids and they were centrifuged down. Cell rinse solution was then added to the pellet to depolymerize matrigel. PDAC organoids and macrophages were then co-cultured in the 24-GLAnCE system (D'Arcangelo et al., 2020) for visualization over a period of 5 days.

For sorting of organoid cells from macrophage/organoid co-cultures, IAA-treated or untreated unlabeled macrophages were co-cultured in matrigel domes with GFP-ve PDAC organoid for 4 days. Domes were then disrupted by pipetting up and down and addition of TRyple enzyme. Single cell suspension containing macrophages and tumor cells were then stained with anti-CD45 antibody and Zombie violet viability dye. Cells were then sorted directly into RNA lysis buffer using the MoFlo Astrios EQ cell sorter (Beckmann Coulter).

Metabolomic Sample Preparation

Briefly, 20 μl of bacterial cultures supernatants or mouse serum were mixed with 80 μl of ice-cold methanol spiked with 5 μl of a 1:1 dilution of an amino acid standard in methanol. The mixture was then incubated at -20°C for 1 hr and centrifuged for 10 minutes at maximum speed in a refrigerated countertop centrifuge. The supernatant was then collected and ran on a mass spectrometer at Dalhousie University Biological Mass Spectrometry Facility. Data analysis was performed using the Skyline software platform

Time-of-Flight mass cytometry (CyTOF)

$CD45^+$ cells were enriched from single cell suspensions from orthotopic PDAC tumors using the positive selection kit and biotin labeled anti-CD45.2 antibody StemCell. Enriched cells were resuspended in Maxpar Staining Buffer, blocked with TruStain Fc blocking buffer for 10 minutes and then resuspended in antibody staining cocktail for 30 Cells were washed twice and incubated in 1 μM Cell_Id cisplatin for 5 minutes. Cisplatin was then quenched by addition of PBS + 5% FBS. Cells were then washed, fixed and permeabilized then barcoded using the Cell-ID multiplex Barcoding kit. Pooled cells were then stained with intracellular antibodies using

the permeabilization buffer from Foxp3 transcription factor staining kit. They were then washed twice with perm. Buffer and resuspended in 1.6% paraformaldehyde in PBS containing 0.3% saponin and 125 nM Iridium (Fluidigm, Cat. # 201192A). They were stored in this solution at 4°C until the day of acquisition when they were centrifuged down, washed with Maxpar buffer and resuspended in Maxpar water + EQ beads solution, and analyzed on a Helios Mass Cytometer (Fluidigm) at the Sickkids CYTOF facility.

Flow Cytometry

PDAC tumors were digested using 100 U/ml collagenase IV and 50 u/ml DNase I in complete RPMI medium at 37C. Single cell PDAC preparations were stained with antibody cocktail at a concentration of 1:300 in FACS buffer (PBS + 2% FBS) for 45 minutes at 4°C in the presence of a fixable viability dye. Cells were then washed twice with FACS buffer, fixed in 4% paraformaldehyde for 10 minutes, washed again with FACS buffer and assessed for fluorescence on a BD Fortessa flow cytometer. For staining of intracellular cytokines cells were first treated for 4 hrs with PMA (5 ng/ml) and ionomycin (500ng/ml) in the presence of Brefeldin A. Surface staining was performed as described above, followed by fixation, permeabilization and staining with intracellular antibodies using the from Foxp3 transcription factor staining kit according to manufacturer's recommendations.

For sorting experiments, mouse tumor cells were stained with anti-CD45, anti-CD11b anti-F4/80 (TAMs) on a MoFlo (Beckman Coulter) cell sorter. For flow cytometric analysis at least 10^5 events were collected on the LSR Fortessa flow cytometer (BD Biosciences).

INFγ blocking or αCD8 T cell delpetion

Orthotopic PDAC surgery was performed on *AhR*$^{fl/fl}$ and *AhR*$^{fl/fl}$ *LMC* mice. At day 3 post-surgery the mice were injected intraperitoneally with 200 μg InVivoMab α-mouse INFγ IgG1 antibody or IgG1 isotype control every 3 days for up to 2 weeks.

In one set of experiments to deplete CD8$^+$ T cells, 3 days post-surgery mice received 200μg of αmouse CD8 IgG2a or IgG2A isotype control in an initial injection and 100μg every third day thereafter for up to 2 weeks.

Tryptophan-deficient diet and indole gavage

One day before PDAC orthotopic surgery, regular mouse chow was replaced by an amino acid control diet or a tryptophan-deficient diet. The diet was maintained for 14 days until the experimental endpoint.

In one set of experiments mice were gavaged with 40μg/kg of IAA, IAld (both from Cayman Chemicals) or ILA (Sigma Aldrich) dissolved in 200μl of water every day beginning 4 days after orthotopic tumor injection.

Metabolomics

Targeted metabolomic profiling of cell culture supernatant was performed using liquid chromatography tandem mass spectrometry as previously described (de Vries et al., 2020). Briefly, 20 μl of cell culture supernatant was mixed with 80 μl of cold methanol and 5ul of internal standard (Isotopically labeled amino acids, 1.25mM, PN MSK-A2-1.2, Cambridge Isotope Laboratories), incubated for 30 minutes at -20 C, centrifuged at 13, 000xg for 5 min at 4 C. Samples were further diluted 10-fold prior to analysis. Quality control (QC) samples were prepared by pooling 10 μl of each sample. All samples including QC's were separated using a Cortecs T3 2.1 x 50 mm, 2.7 μm column (Waters Inc.) using (A) water with 0.1% formic acid and (B) acetonitrile with 0.1% formic acid solvent system coupled to a Sciex Qtrap 5500 triple quadrupole linear ion trap tandem mass spectrometer. The data acquisition included 151 transitions. Data were captured using Analyst, version 1.6.2 software (Sciex); peak integration was performed using Skyline, version 4.1 (Pino et al., 2020). An in-house R script (R-4.0.2) was used for data processing. Metabolites with low peak heights (<5000) and peaks with variable retention times (>30% CV) were excluded from further analysis. Metabolite peak heights were normalized using the mean of nearest QC samples. Statistical analysis and heatmaps were generated with MetaboAnalyst (Xia and Wishart, 2016).

16S rRNA gene sequencing

The V4 hypervariable region of the 16S rRNA gene was amplified using uniquely barcoded forward and reverse sequencing primers to allow for multiplexing. Amplification reactions were performed using 12.5 μL of KAPA2G Robust HotStart ReadyMix, 1.5 μL of 10 μM forward and reverse primers, 7.5 uL of sterile water and 2 μL of DNA. The V4 region was amplified by cycling the reaction at 95°C for 3 minutes, 18x or 24x cycles of 95°C for 15 seconds, 50°C for 15 seconds and 72°C for 15 seconds, followed by a 5-minute 72°C extension. All amplification reactions were done in triplicate, pooled together, and checked on a 1% agarose TBE gel. Pooled triplicates were quantified using PicoGreen and combined by even concentrations. The library was then purified using Ampure XP beads and loaded on to the Illumina MiSeq for sequencing, according to manufacturer instructions (Illumina, San Diego, CA). Sequencing was performed using the V2 (150bp x 2) chemistry. A single-species (*Pseudomonas aeruginosa* DNA), a mock community (Zymo Microbial Standard: https://www.zymoresearch.de/zymobiomics-community-standard) and a template-free negative control were included in the sequencing run.

Analysis of the bacterial microbiome

The last base was removed from all sequences using cutadapt v.1.18. Sequences were assembled and quality trimmed using –fastq_mergepairs with a –fastq_trunctail set at 5, a –fastq_minqual set at 3, and minimum and maximum assemble lengths set at 243 and 263 (+/- 10 from the mean) base pairs. Assembled sequences were quality filtered using –fastq_filter with a –fastq_maxee set at 1.0. The trimmed data was then processed following the UNOISE pipeline. Sequences were first de-replicated and sorted to

remove singletons, then denoised and chimeras were removed using the unoise3 command. Assembled sequences were mapped back to the chimera-free denoised sequences at 97% identity OTUs. Taxonomy assignment was executed using SINTAX, available through USEARCH, and the UNOISE compatible Ribosomal Database Project (RDP) database version 16, with a minimum confidence cutoff of 0.8 (Wang et al., 2007). OTU sequences were aligned using align_seqs.py v.1.9.1 through QIIME1 (Caporaso et al., 2010). Sequences that did not align were removed from the dataset and a phylogenetic tree of the filtered aligned sequence data was made using FastTree (Price et al., 2009). The OTU table, including taxonomic assignments, was imported into MicrobiomeAnalyst (Chong et al., 2020; Dhariwal et al., 2017) for comparisons of alpha diversity and to generate bar plots of taxon relative abundances. Data were filtered to remove OTUs with low counts or variance using default parameters. Data were scaled using Total sum scaling (TSS) to remove variability between samples based on sequencing depth.

QUANTIFICATION AND STATISTICAL ANALYSIS

Number of mice and experiments, and statistical tests are reported in each figure legend. Analyses were performed using GraphPad Prism 8 software. Statistical significance was calculated using *t*-test (unpaired) or Wilcoxon rank-sum test or one-way ANOVA or with Kaplan-Meier analysis followed by the log-rank test. Error bars represent standard deviation and p values <.05 were considered statistically significant (* p <.05, ** p <.01, *** p <.001, **** p <.0001, NS- not significant).

Immunity, Volume *55*

Supplemental information

Tryptophan-derived microbial metabolites activate the aryl hydrocarbon receptor in tumor-associated macrophages to suppress anti-tumor immunity

Kebria Hezaveh, Rahul S. Shinde, Andreas Klötgen, Marie Jo Halaby, Sara Lamorte, M. Teresa Ciudad, Rene Quevedo, Luke Neufeld, Zhe Qi Liu, Robbie Jin, Barbara T. Grünwald, Elisabeth G. Foerster, Danica Chaharlangi, Mengdi Guo, Priya Makhijani, Xin Zhang, Trevor J. Pugh, Devanand M. Pinto, Ileana L. Co, Alison P. McGuigan, Gun Ho Jang, Rama Khokha, Pamela S. Ohashi, Grainne M. O'Kane, Steven Gallinger, William W. Navarre, Heather Maughan, Dana J. Philpott, David G. Brooks, and Tracy L. McGaha

Supplemental Figure Legend

Supplemental Figure 1.

Transcriptomic analysis of TAMs, related to figure 1. $CD45^+CD11b^+F4/80^+$ macrophages were enriched by flow cytometry sorting from normal pancreas (i.e. resident macrophages, n=4 mice) or PDAC tumors from control (n=3)) or *Lyz2*$^{cre/+}$*Ahr*$^{fl/fl}$ (n=3) mice 14 days after tumor implantation. The samples were then analyzed by RNA sequencing. **a)** Volcano plot shows differential expression comparing resident macrophages to control tumor-bearing mice. Red dotted line marks significance threshold (FDR <0.01, logFC>2). **b)** Bar graph of iGSEA analysis of upstream regulators for control TAM versus resident macrophages samples in (***a***). All columns shown have a pval>0.05. **c)** Flow cytometry analysis for dtTomato expression in d14 intratumoral cell populations indicated in tumor-bearing *Lyz2*$^{cre/+}$ x Cg-*Gt(ROSA)26Sor*$^{tm9(CAG-tdTomato)Hze}$/J mice. Pval determined by unpaired students T test. **d)** Volcano plot for differential expression based on transcriptome analysis of TAMs from control versus *Lyz2*$^{cre/+}$*Ahr*$^{fl/fl}$ tumor bearing mice. Red dotted line marks FDR < 0.05. **e)** Venn diagram showing significantly differentially expressed genes (FDR < 0.05, logFC > ± 1) for the comparisons indicated. **f** and **g**) Heatmaps showing significantly differential expression (FDR <0.01, logFC>2) of selected genes involved in cell cycling **(*f*)** or extracellular matrix synthesis **(*g*)**. For heat maps each column represents an individual mouse. **h**) Day 14 orthotopic tumor weight.

Supplemental Figure 2.

Assessment of the immune infiltrate in *Lyz2*$^{cre/+}$*Ahr*$^{fl/fl}$ mice by CyTOF and single cell RNA sequencing analysis, related to figure 3. a) Heatmap showing relative protein expression for each PhenoGraph generated cluster. Arcsinh transformed MSI for each marker was normalized by z-score and heatmap was generated using ggplots application in R. **b)** Graph showing relative abundance of each PhenoGraph cluster in *Lyz2*$^{cre/+}$*Ahr*$^{fl/fl}$ immune infiltrate relative to Control baseline. NS= Pval not significant as calculated using the DiffCYT package. **c)** UMAP plots showing PhenoGraph clustering of immune infiltrate subpopulations in control vs. *Lyz2*$^{cre/+}$*Ahr*$^{fl/fl}$ mice. UMAP and PhenoGraph were run in R for concatenated CYTOF data from live CD45+ cells (4 control

and 5 *Lyz2*$^{cre/+}$*Ahr*$^{fl/fl}$) that were down sampled to 5000 events before analysis. Twenty-four distinct immune clusters were obtained. The experiment was repeated twice with similar results. **d)** Normalized expression and per cluster percentage expression of top 10 marker genes for each cell cluster for the scRNA sequencing analysis described in **Fig 3d**. Both relative expression and percent expression were identified with the Seurat package as described in Methods. Cell labels were assigned to automatically detected clusters based on the top 10 marker genes. **e)** Normalized gene expression per cell of different macrophage marker genes projected onto UMAPs of the concatenated scRNA sequencing of day 14 tumors from *Lyz2*$^{cre/+}$*Ahr*$^{fl/fl}$ mice and littermate controls. **f)** iGSEA analysis showing enrichment for indicated pathways in macrophage 3 cluster as activated (positive Z-score; red) or inhibited (negative Z-score; blue).

Supplemental Figure 3.

Analysis of the role of IDO on tumor growth and AhR function and 16S sequencing analysis of the fecal microbiome, related to figure 4. a) Mice were treated with 1-methyl-tryptophan containing drinking water as previously described (Ravishankar *et al.*, 2015) for 3 days prior to tumor implantation. Tumors weights were determined at day 14 post-implantation as described in methods and compared to B6 and B6.*Ido1-/-* mice on control drinking water. **b)** CD45$^+$CD11b$^+$F4/80$^+$ TAMs were sorted from the tumors in **(*a*),** and expression of the indicated genes was measured by qPCR as described in methods normalized for the housekeeping gene *Bactin.* **c)** Mice (n=4/group) were placed on antibiotic containing drinking water or control water as indicated. 3 days later tumors were implanted. 14 days after tumor implantation CD45$^+$CD11b$^+$F4/80$^+$ TAMs were isolated by flow cytometric sorting and samples from each group were pooled and measured for expression of the genes indicated by qPCR. **d)** Boxplots showing alpha diversity measures calculated at the OTU level using the Simpson index (left panel), the Shannon index (middle panel), or the observed number of OTUs (right panel). Black diamonds overlaying the boxes indicate means; boxes show medians and interquartile ranges. Data points, each of which corresponds to the gut microbiome of one mouse, are colored according to treatment as shown below each panel. P-values shown above each

panel were obtained from Kruskal-Wallis tests. **e)** Relative abundances of the top 10 most abundant bacterial families (left panel) or genera (right panel). “Others” in both panels comprises all bacterial taxa that were present but were less abundant. “V6” (left panel) and “V2” (right panel) includes OTUs whose taxonomies could only be resolved at a higher level than that shown, e.g., at the order or family level, respectively.

Supplemental Figure 4.

Assessment of the effect antibiotics has on *Lactobacillus* presence in the fecal microbiome and the ability of *Lactobacillus* spp to produce indoles, **related to figure 5. a)** B6 mice were placed on antibiotic-containing drinking water as indicated for 4 days prior to collection of fecal material from the large intestine. 16S sequencing was performed, and the proportion of total *Lactobacillus* reads detected as well as reads for specific *Lactobacillus* species as indicated was determined. Relative frequency refers to the % of total sequencing reads identified belonging to the bacteria indicated. The experiment was repeated twice with similar results. **b)** *Lactobacilli* spp. indicated were cultured overnight in triplicate in the media indicated and culture supernatants were measured for the presence of Trp, lactic acid and the indoles indicated by mass spectroscopy analysis. **c)** Heat map showing hierarchical clustering depicting detected metabolites and amino acids indicated by mass spectroscopy analysis. Each column represents an individual culture. **d)** Principal component analysis of the data described in ***(c)***. Open circles identify *L. murinus* and *L. reuteri* culture data under the 3 culture conditions. ***e)*** Germ free B6 mice were gavaged with *L. murinus* or control saline as indicated and described in Methods. 30 days later fecal material was collected from the large intestine and the presence of *L. murinus* was determined by PCR as described in methods. The experiment was repeated twice with similar results. **f)** For the mice described in **(*e*)** fecal material was collected from the large intestine and measured for the indoles indicated by mass spectroscopy. **g)** Fecal measurement of indoles indicated was done by mass spectroscopy on mice with the microbiome enrichment indicated. P values were determined by unpaired students T test. Experiment was repeated twice with similar results.

Supplemental Figure 5.

Cox hazard analysis of *AHR* and OS in the TCGA PAAD cohort and analysis of genes with expression patterns most similar to *AHR,* related to figure 6. a and **b)** Forest plots of Cox proportional hazard analyses in TCGA-PAAD data set. **a)** The top 50% and bottom 50% stratified by median *AHR* expression. **b)** The TCGA-PAAD patient data set stratified by quartiles based on *AHR* expression: lowest 25% (Q1), up to second quartile (Q2), next quartile (Q3), and highest 25% (Q4). **c)** Normalized expression and per cluster percentage expression of *AHR* and the top 25 most similarly expressed genes across cell clusters for the scRNA sequencing analysis described in **Fig 6d.**

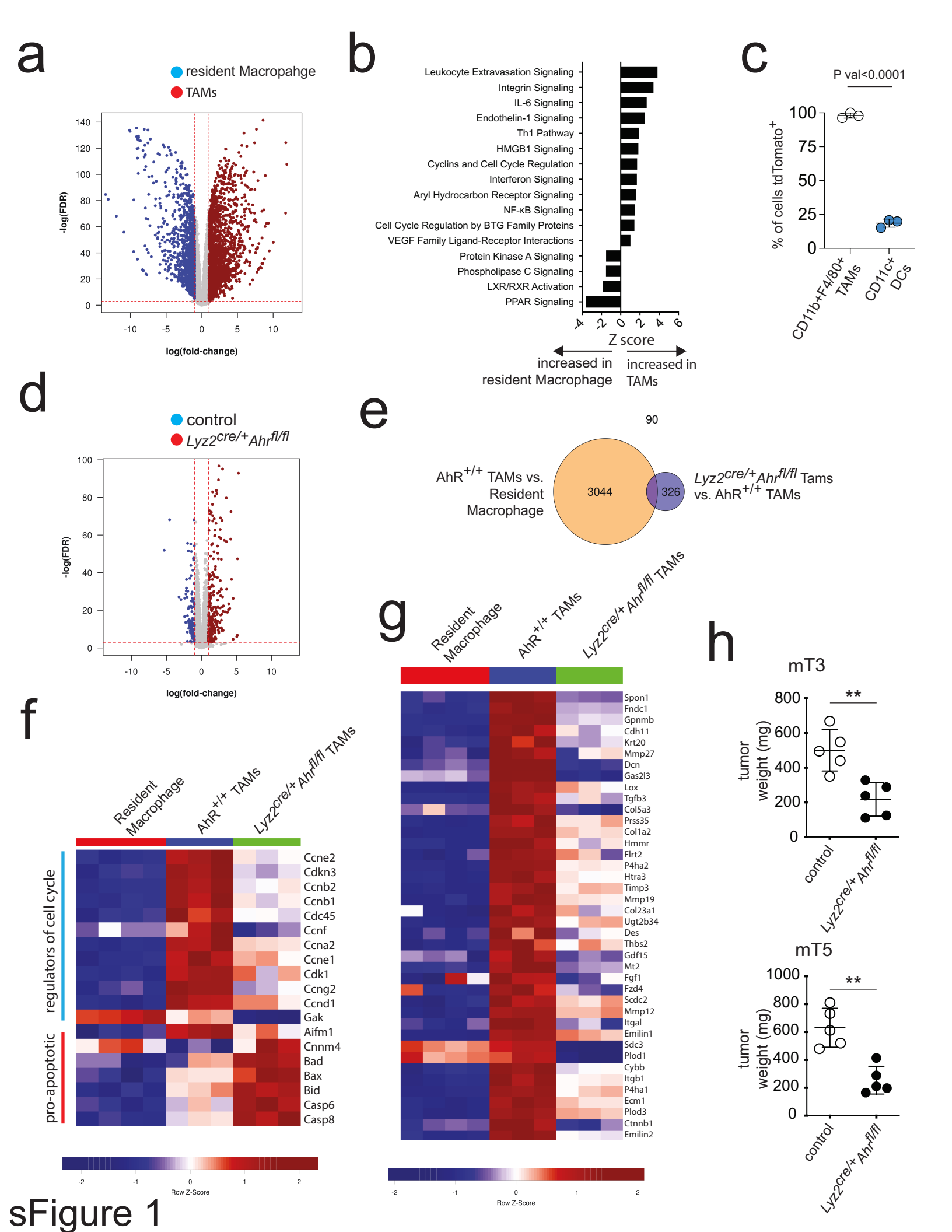
a
resident Macropahge
TAMs
-log(FDR)
log(fold-change)
b
Leukocyte Extravasation Signaling
Integrin Signaling
IL-6 Signaling
Endothelin-1 Signaling
Th1 Pathway
HMGB1 Signaling
Cyclins and Cell Cycle Regulation
Interferon Signaling
Aryl Hydrocarbon Receptor Signaling
NF-κB Signaling
Cell Cycle Regulation by BTG Family Proteins
VEGF Family Ligand-Receptor Interactions
Protein Kinase A Signaling
Phospholipase C Signaling
LXR/RXR Activation
PPAR Signaling
Z score
increased in resident Macrophage
increased in TAMs
c
P val<0.0001
% of cells tdTomato+
CD11b+F4/80+ TAMs
CD11c+ DCs
d
control
Lyz2cre/+Ahrfl/fl
-log(FDR)
log(fold-change)
e
AhR+/+ TAMs vs. Resident Macrophage
3044
326
90
Lyz2cre/+Ahrfl/fl Tams vs. AhR+/+ TAMs
f
Resident Macrophage
AhR+/+ TAMs
Lyz2cre/+ Ahrfl/fl TAMs
regulators of cell cycle
pro-apoptotic
Ccne2
Cdkn3
Ccnb2
Ccnb1
Cdc45
Ccnf
Ccna2
Ccne1
Cdk1
Ccng2
Ccnd1
Gak
Aifm1
Cnnm4
Bad
Bax
Bid
Casp6
Casp8
Row Z-Score
g
Resident Macrophage
AhR+/+ TAMs
Lyz2cre/+ Ahrfl/fl TAMs
Spon1
Fndc1
Gpnmb
Cdh11
Krt20
Mmp27
Dcn
Gas2l3
Lox
Tgfb3
Col5a3
Prss35
Col1a2
Hmmr
Flrt2
P4ha2
Htra3
Timp3
Mmp19
Col23a1
Ugt2b34
Des
Thbs2
Gdf15
Mt2
Fgf1
Fzd4
Scdc2
Mmp12
Itgal
Emilin1
Sdc3
Plod1
Cybb
Itgb1
P4ha1
Ecm1
Plod3
Ctnnb1
Emilin2
Row Z-Score
h
mT3
tumor weight (mg)
**
control
Lyz2cre/+ Ahrfl/fl
mT5
tumor weight (mg)
**
control
Lyz2cre/+ Ahrfl/fl

sFigure 1

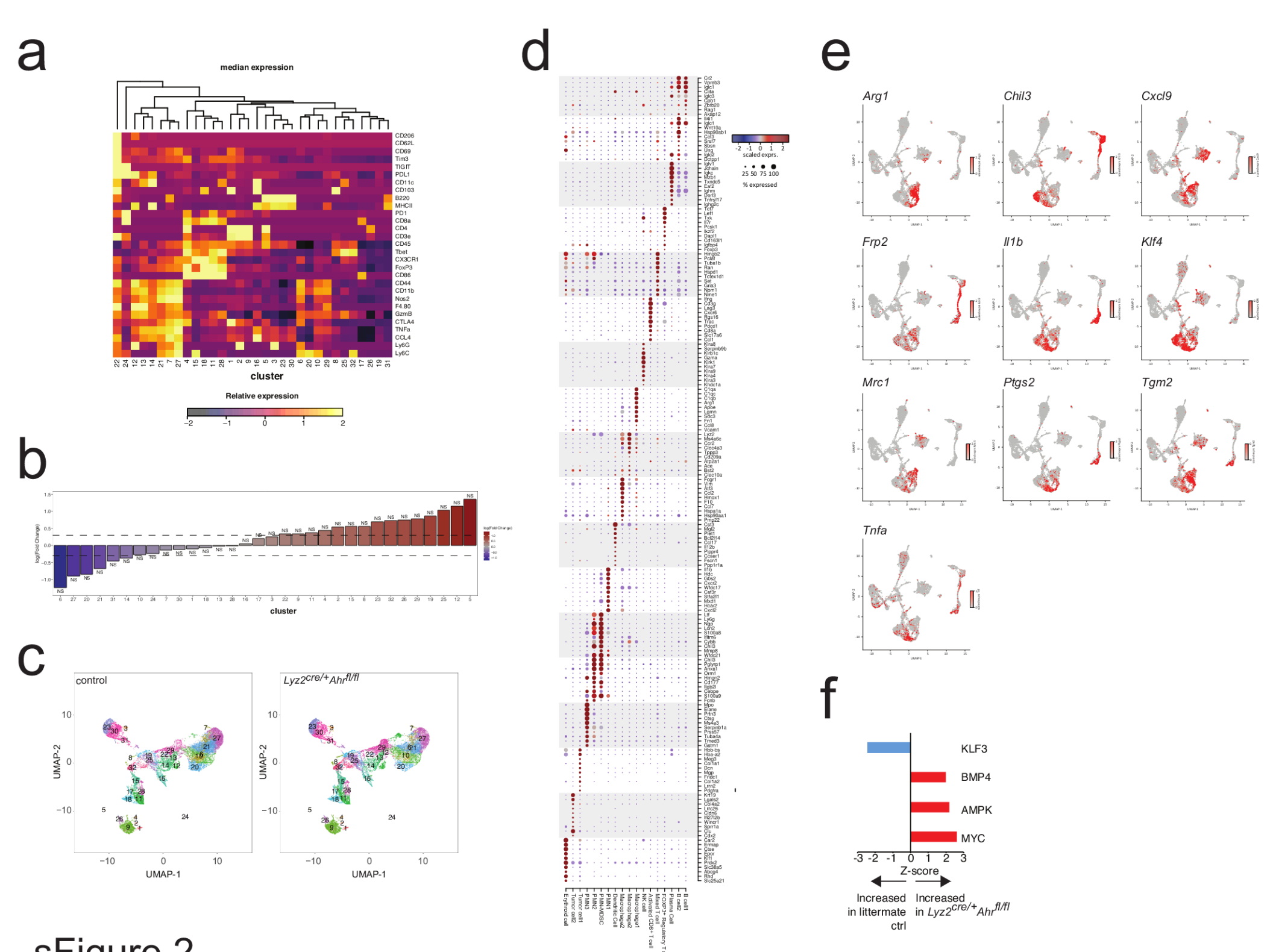
a
median expression
CD206
CD62L
CD69
Tim3
TIGIT
PDL1
CD11c
CD103
B220
MHCII
PD1
CD8a
CD4
CD3e
CD45
Tbet
CX3CR1
FoxP3
CD86
CD44
CD11b
Nos2
F4.80
GzmB
CTLA4
TNFa
CCL4
Ly6G
Ly6C
cluster
Relative expression
b
log(Fold Change)
cluster
c
control
Lyz2cre/+Ahrfl/fl
UMAP-2
UMAP-1
d
scaled exprs.
% expressed
B cell1
B cell2
Plasma Cell
FOXP3+ Regulatory T cell
Activated CD8+ T cell
NK cell
Macrophage1
Macrophage2
Macrophage3
Monocytic Cell
PMN-MDSC
PMN1
PMN2
PMN3
Tumor cell1
Tumor cell2
Erythroid cell
e
Arg1
Chil3
Cxcl9
Frp2
Il1b
Klf4
Mrc1
Ptgs2
Tgm2
Tnfa
f
KLF3
BMP4
AMPK
MYC
Z-score
Increased in littermate ctrl
Increased in Lyz2cre/+Ahrfl/fl

sFigure 2

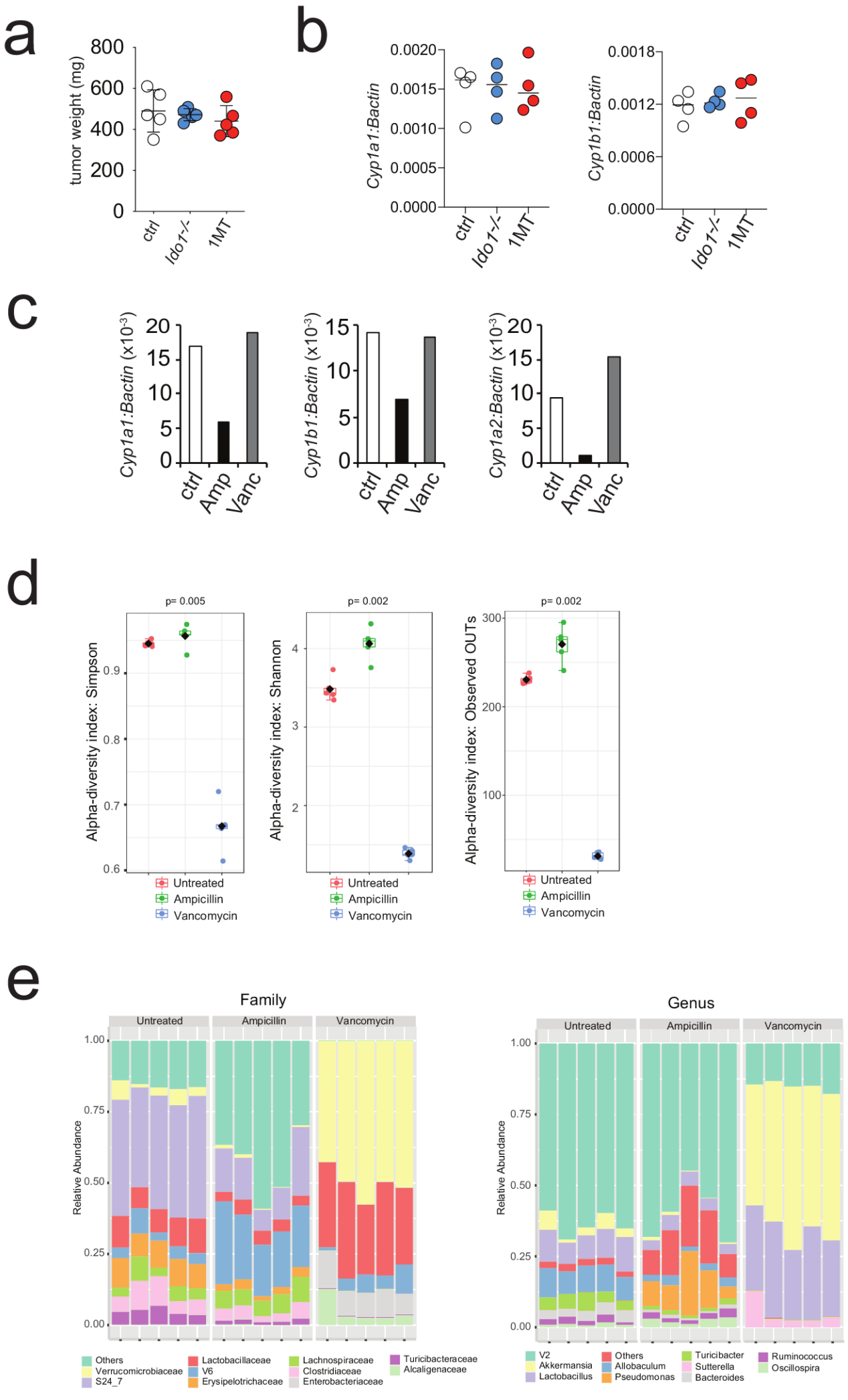
a
tumor weight (mg)
800
600
400
200
0
ctrl
Ido1-/-
1MT
b
Cyp1a1:Bactin
0.0020
0.0015
0.0010
0.0005
0.0000
Cyp1b1:Bactin
0.0018
0.0012
0.0006
0.0000
c
Cyp1a1:Bactin (x10-3)
Cyp1b1:Bactin (x10-3)
Cyp1a2:Bactin (x10-3)
ctrl
Amp
Vanc
d
p= 0.005
p= 0.002
p= 0.002
Alpha-diversity index: Simpson
Alpha-diversity index: Shannon
Alpha-diversity index: Observed OUTs
Untreated
Ampicillin
Vancomycin
e
Family
Genus
Untreated
Ampicillin
Vancomycin
Relative Abundance
Others
Verrucomicrobiaceae
S24_7
Lactobacillaceae
V6
Erysipelotrichaceae
Lachnospiraceae
Clostridiaceae
Enterobacteriaceae
Turicibacteraceae
Alcaligenaceae
V2
Akkermansia
Lactobacillus
Others
Allobaculum
Pseudomonas
Turicibacter
Sutterella
Bacteroides
Ruminococcus
Oscillospira

sFigure 3

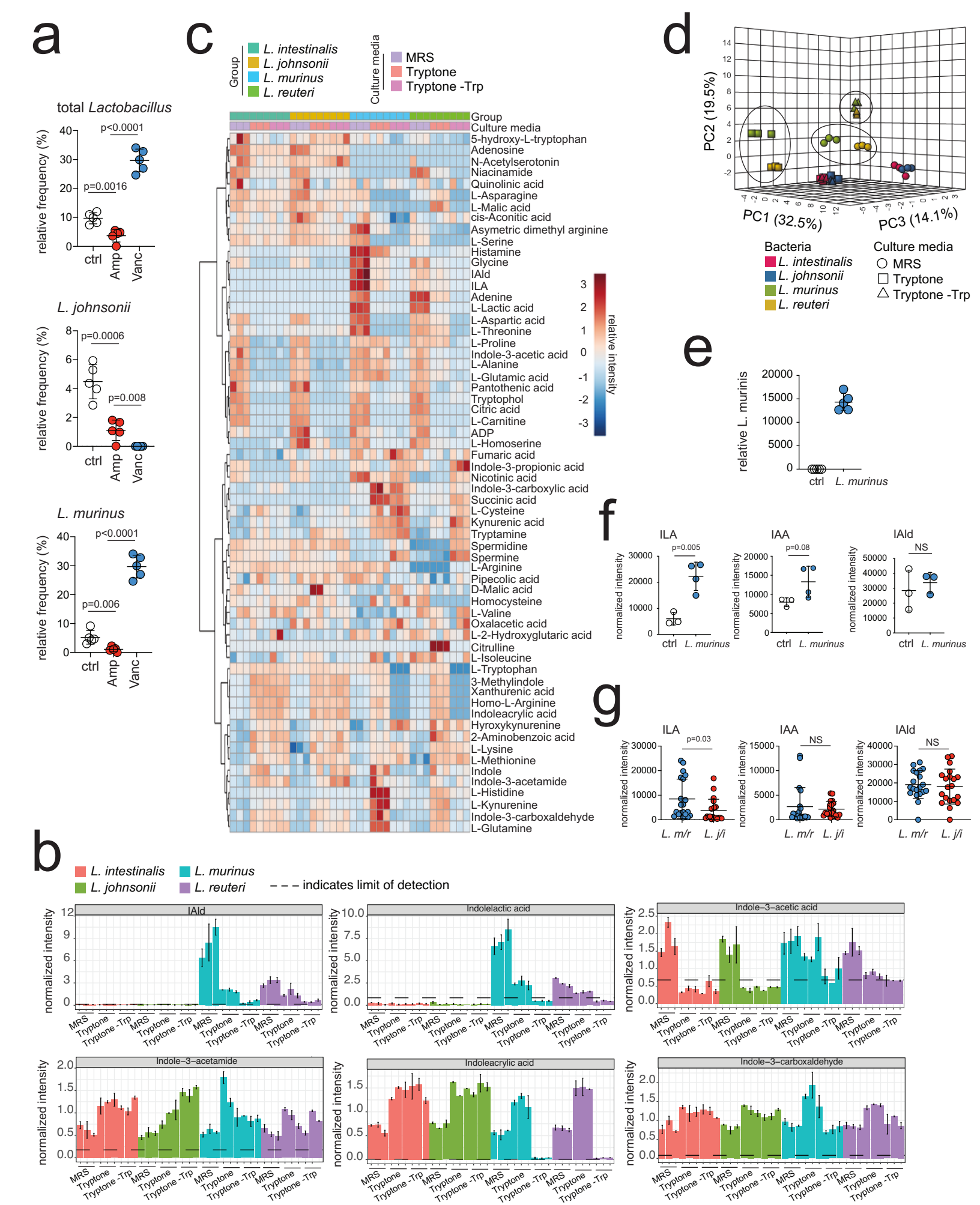
a
total Lactobacillus
p<0.0001
p=0.0016
relative frequency (%)
ctrl
Amp
Vanc
L. johnsonii
p=0.0006
p=0.008
L. murinus
p<0.0001
p=0.006
c
Group
L. intestinalis
L. johnsonii
L. murinus
L. reuteri
Culture media
MRS
Tryptone
Tryptone -Trp
relative intensity
d
PC2 (19.5%)
PC1 (32.5%)
PC3 (14.1%)
Bacteria
Culture media
e
relative L. murinis
f
ILA
IAA
IAld
normalized intensity
p=0.005
p=0.08
NS
g
p=0.03
L. m/r
L. j/i
b
L. intestinalis
L. johnsonii
L. murinus
L. reuteri
– – – indicates limit of detection
IAld
Indolelactic acid
Indole–3–acetic acid
Indole–3–acetamide
Indoleacrylic acid
Indole–3–carboxaldehyde

sFigure 4

a

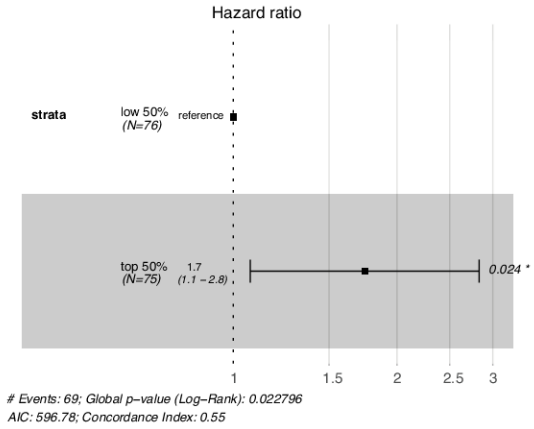

b

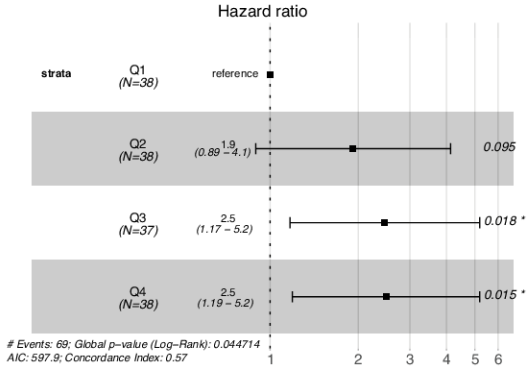

c

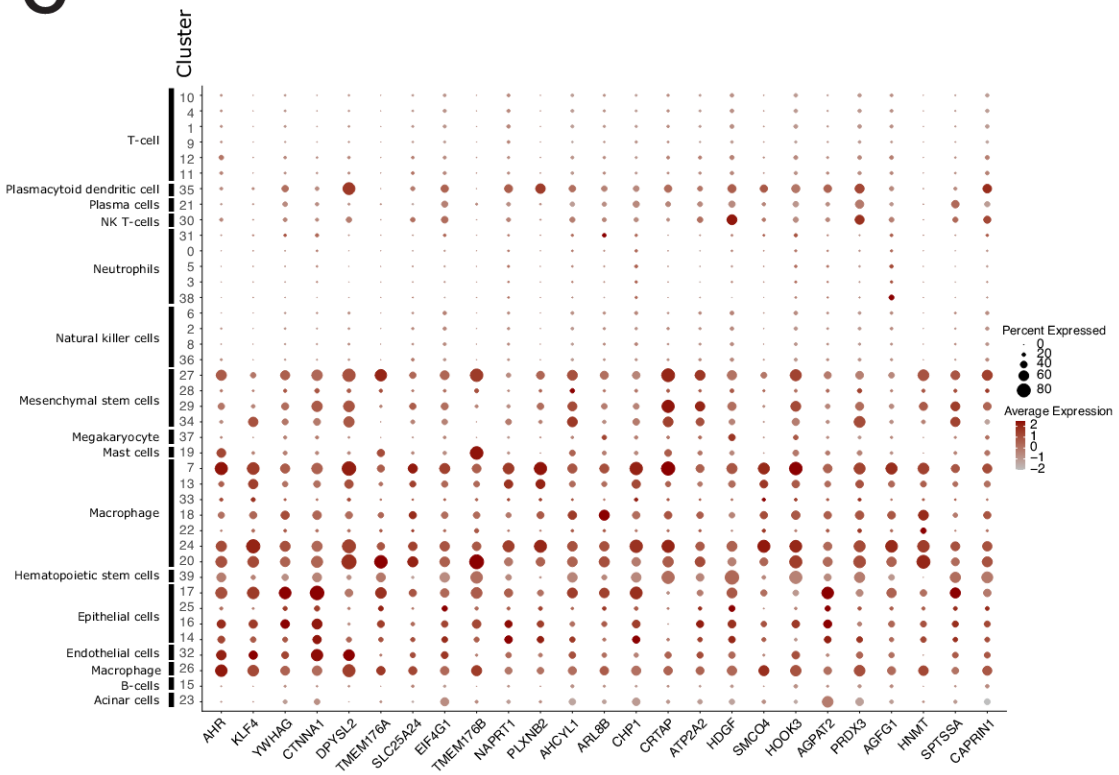

sFigure 5

Bacteria
Bacteroides fragilis
Bacteroides thetaiotaomicron
Bifidobacterium adolescentis
Bifidobacterium bifidum
Clostridium botulinum
Clostridium paraputrificum
Clostridium saccharolyticum
Clostridium sporogenes
Faecalibacterium prausnitzii
Lactobacillus acidophilus
Lactobacillus murinus
Lactobacillus reuteri
Parabacteroides distasonis
Stenotrophomonas maltophilia
Escherichia coli

S Table 2, related to figure 6j. Bacterial taxa target for analysis in figure 6j.